Cold Rydberg-Atom Interactions

by
Aaron W. Reinhard

A dissertation submitted in partial fulfillment
of the requirements for the degree of
Doctor of Philosophy
(Physics)
in The University of Michigan
2008

Doctoral Committee:

Professor Georg A. Raithel, Chair
Professor Paul R. Berman
Professor Roseanne J. Sension
Associate Professor Luming Duan
Assistant Professor Aaron E. Leanhardt

This work is dedicated to my parents, Don and Connie, and to my wife, Sarah.

ACKNOWLEDGEMENTS

I would first like to thank Professor Georg Raithel for giving me the opportunity to work in his lab and for the innumerable things he has taught me. Georg is an outstanding experimentalist who is continually thinking of new and unique ways to do things and who never seems to be at a loss to explain challenging or interesting data. His enthusiasm for physics has been a great inspiration to me and is reflected in all his interactions with students or colleagues. While Georg is a busy person, he always made time to come by the lab and help his students and he is an excellent and patient teacher. I believe that I will be a better scientist by trying to emulate Georg.

It has also been a privilege to work closely with Paul Berman throughout my graduate career. Paul has been like a second advisor to me and his ideas, insights, and wisdom have been essential to the success of our research. He is also an excellent and patient teacher and much of what I know of quantum mechanics and quantum optics I learned from Paul. He has provided valuable perspective as a theorist and has taught me that it takes patience and careful thought to truly understand a problem.

It has been a pleasure to work with all of the outstanding people that have comprised Georg's group throughout my time as a member. Graduate students and postdocs Jeff Guest, Alisa Walz-Flannigan, Natalya Morrow, Spencer Olson, Jae-Hoon Choi, Tara Cubel, Eberhard Hanis, Rahul Mhaskar, Rui Zhang, Brenton Knuffman, Rachel Sapiro, Eric Paradis, Xuhuai Zhang, Mudessar Shah, Kelly Younge, Cornelius

Hempel, Mallory Traxler, and Andrew Schwarzkopf have made the lab a fun and intellectually exciting environment in which to work. I especially thank Tara and Kelly who played an integral role in all of the work described below. I thank Rui, Rachel, Brenton, and Eric for editing chapters of my thesis and I particularly thank Kelly who read the whole manuscript and offered numerous valuable suggestions.

I would like to thank several members of the physics and engineering faculty at Valparaiso University who encouraged me and enabled me to follow my current career path. Professor Doug Tougaw's tireless efforts in advising and scheduling made the difficult task of adding physics as a second major a reality. I fell in love with physics as a freshman in Professor Stan Zygmunt's class. The enthusiasm for science and the support that he and Professors Robert Manweiler, Shirvel Stanislaus, and Donald Koetke provided throughout my years at V.U. had a tremendous influence on me.

There are many people who have made my time in Ann Arbor more fun, rewarding, and enriching. I thank Jack, Ross, Kyrie, Kate, and Doug for the fun we had at lunch every Friday. I thank Beth Miller and everyone involved with the youth program at First United Methodist Church of Ann Arbor for inspiring me to be a leader, challenging me to think outside of myself, and helping me to become a better person.

It has been a real blessing to live so close to all of the members of the Wittrock family for the last five years. Dave and Phyllis' love and support and the time they have made for Sarah and me at their home, taking us out to dinner, or golfing made me feel at home in Ann Arbor from the moment I arrived. Spending time with the whole Wittrock family on the weekends or in the summer enriched Sarah's and my life immensely. The time spent playing with Olivia, Abbey, Silvia, and Emily has been one of the highlights of this period of my life.

Finally, I am forever indebted to my family for their love and support. My sisters, Kate and Sarah, have always loved me for who I am and their hard work, sense of humor, and integrity are continual sources of inspiration for me. Additionally, I would not be who I am without the love and encouragement of my parents. My parents told their children from a young age that they could do whatever they wanted in life and we believed it. My parents provided the support and the means for us no matter what we wanted to do. My father never, ever missed a sporting event or activity that I participated in and continually encouraged me to do my best in whatever I did while never basing his love on the results. My mother is my intellectual and spiritual companion and her love, support, and wisdom encourage me to be who I am and make me a better person every day. Finally, I thank my wonderful wife, Sarah, whose understanding, encouragement, and patience have made these past five years a joy. Her sense of humor, positive attitude, and unconditional love brighten every day. Her ability to listen, empathize, and support on a day-to-day basis has guided me through the ups and downs of this five-year journey.

TABLE OF CONTENTS

LIST OF TABLES

Table

LIST OF FIGURES

Figure

LIST OF APPENDICES

Appendix

ABSTRACT

Systems of cold, interacting Rydberg atoms are of interest because they exhibit a wide range of collective quantum phenomena. This thesis describes experimental and theoretical work related to these systems with an emphasis on two phenomena: Rydberg excitation blockades and quantum-state-changing collisions.

I begin by presenting a detailed calculation of the interaction energies of two Rydberg atoms for a variety of orientations, quantum states, and applied electric fields. The calculated energies are used to interpret the experimental results that follow. I then describe measurements showing that the widths of the distributions of Rydberg excitation number are related to the effectiveness of a Rydberg excitation blockade. These distributions are investigated as a function of principal quantum number, n, and applied electric field. In the presence of a Förster resonant field, sub-Poissonian distributions are measured. I next present a spectroscopic measurement of the energy level shift of a system of atoms which collectively shares two Rydberg excitations. The qualitative nature of the shift depends sensitively on the type of interactions between the atoms (van der Waals or dipole-dipole) and may be changed by changing the quantum state or applied electric field. This measurement provides the first spectroscopic proof that Rydberg excitation blockades are operative. Finally, I describe measurements of the probability for quantum state-changing and Penning-ionizing collisions to provide evidence for intrinsic, electric field-free-interaction resonances and complex many-body interactions in systems of cold Rydberg atoms.

CHAPTER I

Introduction

Systems of Rydberg atoms, or atoms with high principal quantum number, n, represent an ideal platform for the study of a diverse range of quantum phenomena, owing to properties which scale in a definite way with n [3, 4]. Due to the large magnitude of n, many properties of Rydberg atoms are exaggerated relative to those for ground-state atoms. For example, the orbital radius of a Rydberg atom scales as n^2 leading to a geometric cross section that scales as n^4. Therefore, Rydberg atoms are enormously larger than ground-state atoms and exhibit collision cross sections that are orders of magnitude higher (about $10^3 - 10^5$ times for $n = 40 - 100$). Other examples include binding energy, which scales as n^{-2}, and radiative lifetime, which scales as $n^3 - n^5$, depending on the angular momentum quantum numbers of the state in question. Therefore, Rydberg electrons are loosely bound and highly sensitive to external perturbations such as stray electric fields and blackbody radiation. However, they exhibit extremely long lifetimes (hundreds of microseconds) and narrow (sub-MHz) transition widths when sources of decoherence are minimized.

The property which has stimulated the most recent experimental and theoretical work, however, is strong interactions among neutral Rydberg atoms separated by relatively large (several μm) distances. These long-range interactions arise because

of transition dipole moments to nearby states which scale as n^2 and electric polarizabilities which scale as n^7. Rydberg-Rydberg interactions give rise to coherent many-body processes that have potential applications in quantum-information science and lead to a number of interesting coherent and incoherent collision-induced dynamics. It is the interactions between Rydberg atoms – their properties and their manifestations in experimental systems – that are the subject of this thesis.

1.1 Coherent many-body processes in cold Rydberg gases

In order to study the coherent, many-body dynamics of Rydberg atom systems, it is important to eliminate the decohering effects of thermal motion. Additionally, one must employ an atomic ensemble with a high enough density that many-body interaction effects become important. Historically, Rydberg atom experiments were performed using atomic beams and vapor cells, and suffered from thermal motion. Recent developments in the area of neutral-atom laser cooling and trapping [5], however, have opened up a whole new world of possibilities for studying coherent properties of Rydberg-atom systems. The ability to prepare relatively high density ($\sim 10^{10} - 10^{12}$ cm^{-3}) and low temperature (hundreds of μK) ensembles of ground-state atoms which may then be excited to Rydberg states allows an experimenter to eliminate the effects of thermal motion and perform experiments on Rydberg atoms which are stationary on experimental time scales ($\sim \mu$s). Systems of cold Rydberg atoms are often termed "frozen Rydberg gases" because the atoms within the system interact strongly while moving only a negligible fraction of their separations during an experiment [6, 7].

Several experiments have shown that there is a close connection between frozen Rydberg gases and condensed matter physics systems such as amorphous solids and

spin glasses [6–10]. When an ensemble of cold atoms is excited into Rydberg states, the excitations are delocalized and shared collectively among all atoms within certain regions over short (several hundred ns) time scales [11]. For example, the first excited state of an N-atom ensemble is a state with one shared excitation, $|N,1\rangle = \frac{1}{\sqrt{N}}\Sigma_{i=1}^{N}|g_1, g_2, ..., r_i, ..., g_N\rangle$, where the subscripts are atom labels, $|g\rangle$ denotes an atom in the ground state, and $|r\rangle$ an atom in the Rydberg state. This system is analogous to Mott-Wannier excitons in crystals [12]. On slightly longer time scales (several μs), excitations are no longer coherently shared; instead, the decohering effects of stray electric and magnetic fields, atomic motion, or blackbody radiation project the excitations onto single atoms. These excitations may undergo quantum diffusion processes whereby they coherently travel or "hop" from atom to atom while the atoms largely remain frozen in space [6, 7, 9, 13]. This situation is analogous to Frenkel excitons in crystals [12]. The analogy between atomic systems and excitons is strengthened by the recent observation of Bose-Einstein condensation of excitons [14].

In addition to producing exciton-like behavior, interactions in cold Rydberg-atom systems may lead to resonant or near-resonant dipole-dipole energy transfer between atoms. This energy transfer has been studied as a function of applied electric field [6, 7], in the presence of an extra, controllably-introduced perturbing state [15, 16], and as a function of dimension of the system [17] in order to provide evidence for the coherent interaction of many atoms simultaneously, or many-body interactions. Dephasing of dipole-dipole energy transfer in these many-atom systems has been studied [9, 13] and nearly instantaneous ionization has been attributed to many-body processes [18]. Finally, direct optical excitation of dipole-forbidden transitions has been observed at an avoided crossing caused by strong, coherent interactions [19].

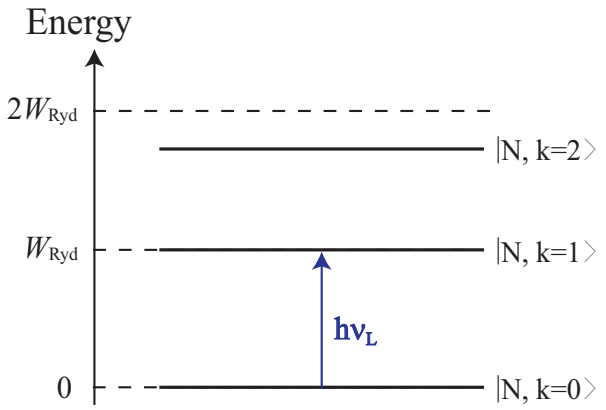

Figure 1.1: The first three energy levels of a system of N atoms containing k collective Rydberg excitations.

A property of coherent, many-body excitations of cold Rydberg-atom systems which has generated considerable recent interest is a phenomenon called an "excitation blockade," which has several proposed applications in quantum information science [2, 20–22]. As mentioned above, excitation of ensembles of cold atoms into Rydberg states produces collective quantum states in which k Rydberg excitations are coherently distributed among all N atoms in a given region. Because of van der Waals and dipole-dipole interactions between Rydberg atoms, the energy levels of the collective system deviate from an equidistant ladder $W_k = kW_{\rm Ryd}$, where k is the number of Rydberg excitations and $W_{\rm Ryd}$ the energy of a single, isolated Rydberg atom [11]. In the illustration in Fig. 1.1, the energy of the second excited state, $|N, 2\rangle$, is lowered by the Rydberg-Rydberg interaction energy, ΔW. The energies of higher excited states $|N, k\rangle$, $k > 2$ are shifted by amounts different than the shift of $|N, 2\rangle$, corresponding to the interaction energy of three or more Rydberg atoms. If the excitation laser is tuned to the lowest transition, $|N, 0\rangle \rightarrow |N, 1\rangle$, and the excitation bandwidth is less than $\Delta W/h$, where h is Planck's constant, there will be negligible excitation of all but the first collective state, $|N, 1\rangle$. This phenomenon, called an excitation blockade because excitations with $k > 2$ are "blocked," has

been observed in several independent experiments [11, 23–27] and has been studied theoretically [28–32].

1.1.1 Applications of the dipole blockade

A 2000 paper by Jaksch and coworkers [20] details the use of a Rydberg excitation blockade based on dipole-dipole interactions (a "dipole blockade") to achieve a quantum phase gate using two neutral atoms. A quantum phase gate, when combined with a Hadamard gate to achieve qubit (quantum-bit) rotations, realizes a controlled-NOT (CNOT) gate [33]. The CNOT gate can be used to implement any arbitrary quantum logic operation [34]. The authors of Ref. [20] first describe a scheme to implement a quantum phase gate that does not rely on the dipole blockade; however, such gates suffer from decoherence associated with significant mechanical forces on the involved atoms when both are in the Rydberg state. They then present a second scheme which relies on the dipole blockade to suppress excitation of the doubly-excited state in Fig. 1.1. Since the doubly-excited state is never populated, mechanical effects due to Rydberg-Rydberg interactions are suppressed. The experimental implementation of this phase gate is one of the long-term goals of the project described in this thesis. Therefore, I will present a brief explanation of the operation of this gate, which is schematically illustrated in Fig. 1.2.

The gate is based on two atoms which can each be in superpositions of two qubit states, $|g\rangle$ and $|e\rangle$, associated with different long-lived hyperfine ground states. Each atom is assumed to be individually addressable with a time-dependent Rabi frequency $\Omega_i(t)$, where i is the atom label (1 or 2), and $\Omega_i \ll \Delta W$. State $|e\rangle$ is not coupled to any other level, and $\Omega_i(t)$ couples atom i from the state $|g\rangle$ to the Rydberg level, $|r\rangle$. In general, the two-level system $\{|g\rangle, |r\rangle\}$ driven by an optical pulse with

pulse area $\theta = \int_{\infty}^{-\infty} \Omega_i(t')\,dt'$ will evolve to the state $|\psi\rangle = \cos\frac{\theta}{2}|g\rangle - \imath \sin\frac{\theta}{2}|r\rangle$. The gate proceeds in the following steps:

i) A π-pulse is applied to atom 1 (denoted in Fig.1.2 as π_1)

ii) A 2π-pulse is applied to atom 2 ($2\pi_2$)

iii) A π-pulse is again applied to atom 1 (π_1).

The essential idea of the gate is that the dipole blockade will prevent the population of the two-atom state $|rr\rangle$ if the system begins in state $|gg\rangle$. Therefore, if the system is initially in the state $|gg\rangle$, $|ge\rangle$, or $|eg\rangle$, it will acquire a phase of π. If it is in the state $|ee\rangle$, it will remain unchanged (see Fig. 1.2). Thus, a phase gate which changes the phase of the two-qubit state by π for all states except $|ee\rangle$ is realized.

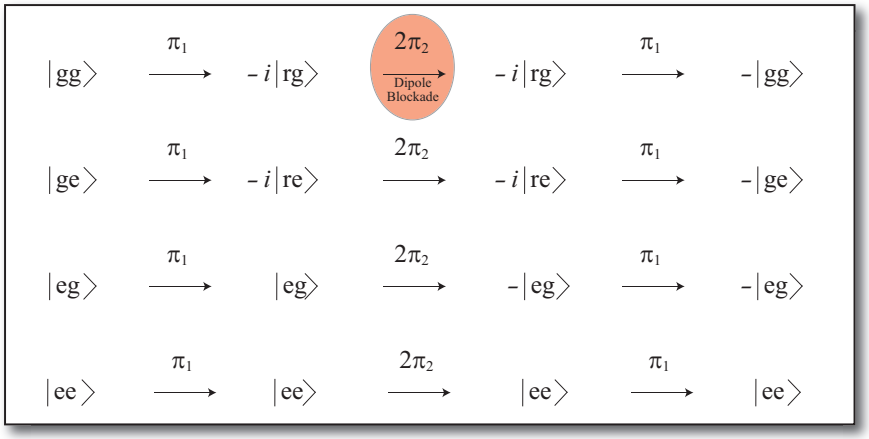

Figure 1.2: Schematic illustration of the operation of a quantum phase gate utilizing the dipole blockade.

The design and implementation of phase gates similar to the one described above have been investigated in detail [35–39] and several groups are currently working towards its experimental realization. Highly efficient Rydberg excitation using π-pulses [40] and STIRAP [41] has been demonstrated. Additionally, atom-trapping ge-

ometries which allow strong dipole-dipole interactions across adjacent trapping sites have been realized using holographic atom traps [42–44] and single atoms trapped in an optical lattices with a large (~ 5 μm) lattice constant [45].

In addition to its application in the above quantum phase gate proposal, the dipole blockade plays a central role in several other promising applications. Saffman and Walker propose a scheme to create a single-photon source with controlled emission direction using four-wave mixing in a blockaded system [21]. Lukin and coworkers propose using the dipole blockade to create a mesoscopically entangled ensemble and show that an entangled state of many atoms with one shared excitation may realize a quantum phase gate [2]. Bouchoule and Mølmer suggest using this entangled state to create a spin squeezed state [22]. A spin squeezed state may be used in schemes to improve spectroscopic resolution and in atomic clocks.

1.2 Incoherent collisional processes in cold Rydberg gases

We have seen that coherent interactions among Rydberg atoms give rise to a number of interesting and potentially useful phenomena. However, incoherent collisional processes in cold Rydberg atom systems lead to a wide variety of equally interesting physics. For example, in addition to the above described analogy with solids, systems of cold Rydberg atoms are closely related to a different, novel state of matter: ultracold plasmas. Ultracold plasmas, or plasmas with electron and ion temperatures of $T_{\rm e} \sim 1-1000$ K and $T_{\rm ion} \geq 100$ μK, may be formed by photoionizing cold ground-state atoms with a laser tuned just above the ionization threshold [46]. However, systems of cold Rydberg atoms may spontaneously evolve into ultracold plasmas [47–49] and Rydberg atoms may be created from free electrons and free ions in expanding ultracold plasmas [50]. A connection between ultracold plasmas and

Rydberg atoms is made by the interactions between Rydberg atoms. The strong, often attractive forces between Rydberg atoms leads to motion on attractive molecular potentials and leads to state mixing and often ionization, which may lead to plasma formation [51].

Motion of atoms on strong attractive potentials, however, has much more universal impact on the properties of cold Rydberg gases than just the evolution of a system between Rydberg gases and cold plasmas. Depending on the detailed nature of the quantum states of the interacting atoms, motion along attractive potentials and subsequent state-mixing may give rise to very disparate phenomena. Such phenomena include the formation of bound states between two Rydberg atoms [52, 53], or "Rydberg molecules," and the conversion of internal atom energy to center-of-mass-energy [54, 55], thereby creating pairs of fast "Rydberg atoms" which move away from one another at high speeds. Motion along attractive molecular potentials also leads to high rates of n-changing and ℓ-changing collisions that can significantly affect the evolution dynamics of a cold Rydberg gas (n and ℓ are the principal quantum number and angular momentum quantum numbers of the colliding atoms) [48, 49, 53].

Experiments have also been performed that probe the dynamics of Rydberg-atom interactions as a function of atom-atom separation or applied electric field. Since the Rydberg-Rydberg interaction potential is dependent on the separation between two or more atoms to be excited, detuning the Rydberg excitation laser by different amounts allows an experimenter to excite atoms at various places on an attractive or repulsive molecular potential. This technique has been used to probe the pair separation distribution of atoms, provide information on the nature of interaction potentials, and investigate Penning ionization [56, 57]. Additionally, an applied electric field has been used to tune a Förster resonance and probe the energy transfer

dynamics of interacting atoms when one interaction channel is exactly resonant [58].

1.3 Thesis outline

In this thesis, I will describe contributions that my co-workers and I have made to the field of interactions among cold Rydberg atoms. I discuss theoretical calculations of Rydberg-Rydberg interaction energies, experiments related to the coherent nature of the many-body states into which Rydberg-atom systems are excited, and collisional measurements which demonstrate the coherent and incoherent evolution of these systems. Thus, this work represents a relatively broad picture of Rydberg-Rydberg interactions and their experimental manifestations.

Specifically, I begin in Chapter II by presenting a detailed calculation of two-body Rydberg-Rydberg interaction potentials as a function of principal quantum number n, angular momenta ℓ and j, atom-atom orientation, and applied electric field. Although I will later discuss certain cases in which a two-body picture of Rydberg atom interactions fails, the potentials presented in this section will provide considerable insight into all experiments presented in this thesis. In Chapter III, I discuss two methods to laser cool and trap ground-state ^{85}Rb atoms and describe how these atoms are excited to Rydberg states. I describe the method used to detect the number of excitations created as well as their quantum state distribution. In Chapter IV, I discuss two methods that may be used to measure the effect of a Rydberg excitation blockade. I describe the advantages of a technique that we have developed, the "counting statistics" method, and present detailed experimental investigations of the effectiveness of Rydberg excitation blockades using this technique. After describing how one may observe the effects of an excitation blockade, I describe in Chapter V measurements which use spectroscopic techniques to directly probe the

energy structure of the first two transitions in the ladder in Fig. 1.1. Spectroscopically measuring the energy shift of the state $|N, 2\rangle$ amounts to a direct proof that the excitation blockade mechanism is operative. Finally, in Chapter IV, I discuss measurements of the probabilities for state-changing and Penning-ionizing collisions in ensembles of interacting Rydberg atoms. This includes short-time, coherent energy transfer collisions and time-delayed, motion-induced collisions. These measurements provide evidence for intrinsic, field-free interaction resonances (discussed in Chapter II) and many-body physics in systems of interacting Rydberg atoms.

CHAPTER II

Computation of binary interaction energies

In this chapter I present a two-body calculation of Rydberg-Rydberg interaction energies for different quantum states and atom-atom orientations. The qualitative features of these results will provide considerable insight into nearly all experiments described in this thesis. Additionally, the potentials calculated here are used for quantitative comparison with experiment when appropriate. A two-atom picture, however, sometimes fails in describing certain experimentally observed phenomena. As discussed in Chapter VI, some results may only be explained by including many-body interactions. Nonetheless, the two-atom picture described here is very useful in understanding many of the experiments described below and we will note the limits of its validity when necessary.

2.1 Computation of binary energy level shifts

In classical electrodynamics, it common to obtain the energy of a localized charge distribution placed in an external potential by summing the contributions of successive terms in a multipole expansion of the energy [59, 60]. If two charge distributions each having no net charge but nonzero dipole moments are brought close together, the interaction energy will be given, to lowest order, by the dipole-dipole term in

this expansion. This dipole-dipole interaction energy is given (in atomic units[1]) by

$$V_{\rm dd} = \frac{\mathbf{p}_1 \cdot \mathbf{p}_2 - 3(\mathbf{n} \cdot \mathbf{p}_1)(\mathbf{n} \cdot \mathbf{p}_2)}{R^3} \quad , \tag{2.1}$$

where $\mathbf{R}$ is the vector between the dipole moments, $\hat{\mathbf{n}}$ is a unit vector along $\mathbf{R}$, and $\mathbf{p}_1$ and $\mathbf{p}_2$ are the dipole moments of the two distributions.

The situation for two neutral atoms is quite similar, with $V_{\rm dd}$ becoming the *operator* $\hat{V}_{\rm dd}$ and $\mathbf{p}_1$ and $\mathbf{p}_2$ becoming dipole moment operators. This operator describes the interaction energy between two atoms with dipole moment operators $\hat{\mathbf{p}}_{\rm i} = -\mathbf{r}_{\rm i}$, where $\mathbf{r}_{\rm i}$ is the coordinate of electron i relative to the nucleus of atom i. This operator has nonzero coupling matrix elements of the type $\langle B| \otimes \langle C|V_{\rm Int}|A\rangle \otimes |A\rangle$, where $|A\rangle$, $|B\rangle$ and $|C\rangle$ are single-particle Rydberg states. In this chapter I calculate quantum-mechanically the effect of these couplings on the energy of two particles initially in the state $|A\rangle \otimes |A\rangle$.

Similar to the treatment of classical charge distributions, higher-order atomic multipole moments can be defined and the effect of the interaction between these multipole moments may be calculated quantum mechanically. In the following we estimate the relative importance of such terms and show that, for systems of interest in this thesis, it is sufficient to restrict our attention to dipole-dipole interactions. The electric-dipole interaction operator in Eq. 2.1 scales as $\hat{V}_{\rm dd} \sim n^4/R^3$, where n is the principal quantum number of the interacting Rydberg atoms [51]. If there is no external electric field applied, the electric-dipole interaction produces energy level shifts only in second order, because low-angular-momentum Rydberg states of alkali atoms in zero electric field do not have permanent dipole moments. For this general case, the level shifts scale as $\sim n^{11}/(sR^6)$, where the parameter s is a measure for

[1] Atomic units are used throughout this thesis. In atomic units the electron's mass and charge, the Bohr radius, Planck's constant, and $4\pi\epsilon_o$ are all unity by definition. Thus, distances are measured in units of Bohr radii, energies in terms of the Hartree energy ($\frac{\hbar^2}{m_e a_o^2}$), and angular momenta in units of Planck's constant.

the magnitude of the energy detunings of the involved interaction channels and is of order 0.1 or less [51]. For P and D states, the quadrupole-quadrupole interaction occurs in first order and leads to shifts that scale as $\sim n^8/R^5$ [61]. Therefore, the ratio of the quadrupole-quadrupole interaction to the second-order dipole-dipole interaction scales as sR/n^3. For the interatomic separations of interest in this thesis ($R \sim 10n^2$), this ratio is $\sim 1/n$. We therefore restrict our calculations to the dipole-dipole interaction, which represents the dominant interaction at the atomic separations of interest. It is noted that in more general cases quadrupolar and higher interactions will also become important [53, 61–64].

In the case of zero external field, computation of the energy level shifts due to the electric-dipole interaction requires the evaluation of two-atom matrix elements of the form

$$\langle n'', \ell'', j'', m_{\rm j}''| \otimes \langle n', \ell', j', m_{\rm j}'|\hat{V}_{\rm dd}|n, \ell, j, m_{\rm j}\rangle \otimes |n, \ell, j, m_{\rm j}\rangle \quad , \tag{2.2}$$

where $\hat{V}_{\rm dd}$ is given in Eq. 2.1. For the purposes of our calculation, we assume that the initial state is a product of two single-atom states, *i.e.* not a state reflecting coupled angular momenta. The geometry of the problem is depicted in Fig. 2.1.

Dropping the hats on quantum mechanical operators for convenience, $\hat{V}_{\rm dd}$ can be written as

$$\begin{aligned} V_{\rm dd} \;=\; & \frac{p_{1\rm x}p_{2\rm x}\left(1-3\sin^2\theta\right)+p_{1\rm y}p_{2\rm y}+p_{1\rm z}p_{2\rm z}\left(1-3\cos^2\theta\right)}{R^3} \\ & -\frac{3\sin\theta\cos\theta\left(p_{1\rm x}p_{2\rm z}+p_{1\rm z}p_{2\rm x}\right)}{R^3} \end{aligned} \tag{2.3}$$

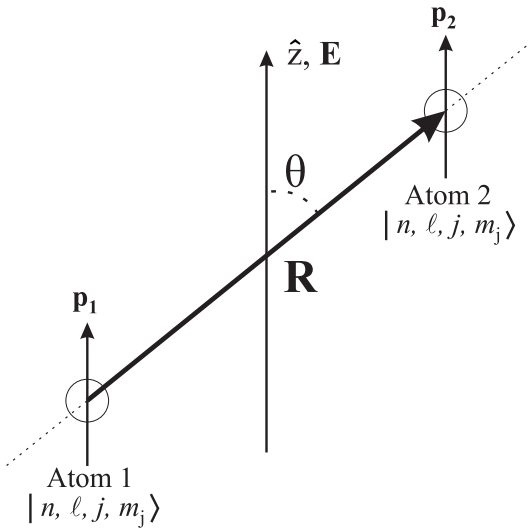

Figure 2.1: Two interacting Rydberg atoms separated by a vector $\mathbf{R}$ which defines an angle θ with the quantization ($\hat{\mathbf{z}}$) axis. In cases where an electric field $\mathbf{E}$ is applied, the quantization axis is parallel to the field.

or

$$\begin{aligned} V_{\rm dd} \;=\; & \frac{p_{1+}p_{2-} + p_{1-}p_{2+} + p_{1z}p_{2z}\,(1-3\cos^2\theta)}{R^3} \\ & - \frac{\frac{3}{2}\sin^2\theta\,(p_{1+}p_{2+} + p_{1+}p_{2-} + p_{1-}p_{2+} + p_{1-}p_{2-})}{R^3} \\ & - \frac{\frac{3}{\sqrt{2}}\sin\theta\cos\theta\,(p_{1+}p_{2z} + p_{1-}p_{2z} + p_{1z}p_{2+} + p_{1z}p_{2-})}{R^3} \end{aligned} \tag{2.4}$$

where the first subscript of the p-components identifies the atom number, $p_\pm = -\frac{1}{\sqrt{2}}(x \pm iy)$, and $p_z = -z$. The matrix elements of $V_{\rm dd}$ are independent of the azimuthal angle of $\mathbf{R}$. From the expression in Eq. 2.4, we see that calculating two-particle matrix elements of $V_{\rm dd}$ involves evaluating the single-particle matrix elements $\langle n', \ell', j', m_{\rm j}'|p_{\alpha,\beta}|n, \ell, j, m_{\rm j}\rangle$ where α is the particle number and $\beta \in \{+, -, z\}$.

2.1.1 Determination of Rydberg atom wavefunctions

In the following, I explain the essential details of the numerical method used to obtain the single-particle radial wavefunctions, $\psi(r)$, required to calculate the single-particle matrix elements $\langle n', \ell', j', m_{\rm j}'|p_{\alpha,\beta}|n, \ell, j, m_{\rm j}\rangle$ of which the two-particle matrix

elements in Eq. 2.2 are composed. The radial Schrödinger equation is integrated using an algorithm that continuously adjusts the step size such that it is smaller than, but close to, $2\pi/\tilde{v}$ divided by a constant, f, where $\tilde{v} = \sqrt{|2E + 2/r - l(l+1)/r^2|}$ (E is the single-particle level energy). In the classically allowed region, the step size approximately equals the de Broglie wavelength divided by f. To ensure reliable integration through the classical turning points, where the local wavelength diverges, the step size is limited to a maximal value of $d_{\rm max}$. For the data presented in this paper, the step size parameters have been set to $f = 200$ and $d_{\rm max} = 1$. Since the local wavelength of the Rydberg-electron wavefunction is very large at locations far away from the core, the step-size adjustment considerably speeds up the integration. The accuracy of $\psi(r)$ is consistent over a broad range of r because the number of points per wavelength at which the wavefunction is determined is approximately fixed. The wavefunctions are integrated inward. Assuming that the wavefunction has known values ψ_0 and $\psi_{\rm p}$ at locations r_0 and $r_{\rm p}$ ($r_0 < r_{\rm p}$), respectively, a location $r_{\rm m}$ is determined using the above step width rules ($r_{\rm m} < r_0$ and $r_0 - r_{\rm m} \lesssim \min(d_{\rm max}, 2\pi/(\tilde{v}(r_0)f))$). To determine the wavefunction $\psi_{\rm m}$ at location $r_{\rm m}$, we use

$$\begin{aligned} h &= (r_{\rm p} - r_0)(r_0 - r_{\rm m})(r_{\rm p} - r_{\rm m}) \\ f_p &= 2(r_0 - r_{\rm m})/h \\ f_m &= 2(r_{\rm p} - r_0)/h \\ \psi_m &= ((-p^2(r_0) + f_{\rm p} + f_{\rm m})\psi_0 - f_{\rm p}\psi_{\rm p})/f_{\rm m} \quad , \end{aligned}$$

where $p^2(r) = 2E + 2/r - l(l+1)/r^2$. This method allows for continuous changes of the step size $r_0 - r_{\rm m}$. To estimate the effect of numerical errors in the wavefunction calculations on the van der Waals level shifts, we have performed test calculations with finer step sizes (parameters $f = 400$ and $d_{\rm max} = 0.3$). Based on the results,

the numerical errors of the van der Waals level shifts presented here are estimated at about one percent or less.

2.1.2 Computation of energy level shifts in zero electric field

To calculate van der Waals energy level shifts due to $V_{\rm dd}$ in zero external electric field, we sum the level shifts due to many perturbing channels in second-order perturbation theory using the calculated matrix elements of $V_{\rm dd}$. Explicitly, the van der Waals shift of the two-particle state $2 \times |n, \ell, j, m_{\rm j}\rangle$ is given by the sum

$$\Delta W^{(2)} = - \sum_{\substack{n',\ell',j',m'_{\rm j}, \\ n'',\ell'',j'',m''_{\rm j}}} \frac{|\langle n'', \ell'', j'', m''_{\rm j}| \otimes \langle n', \ell', j', m'_{\rm j}|V_{\rm dd}|n, \ell, j, m_{\rm j}\rangle \otimes |n, \ell, j, m_{\rm j}\rangle|^2}{\Delta} \quad , \tag{2.5}$$

where $\Delta = W_{|{\rm n}'',\ell'',{\rm j}'',{\rm m}''_{\rm j}\rangle} + W_{|{\rm n}',\ell',{\rm j}',{\rm m}'_{\rm j}\rangle} - 2 \times W_{|{\rm n},\ell,{\rm j},{\rm m}_{\rm j}\rangle}$ is the infinite-separation energy defect and $W_{|A\rangle}$ is the single-atom energy of state $|A\rangle$. To reduce the amount of data in the calculation of the level shifts, we include only two-particle couplings with $|\langle ...|V_{\rm dd}|...\rangle| > 10^{-4} \times n^{*4}/R^3$, where $n^* = n - \delta_\ell$ is the effective principal quantum number.[2] It is noted that all non-continuum matrix elements of $V_{\rm dd}$ are calculated before the small ones are discarded. Furthermore, in the sum in Eq. 2.5 we only include terms with $|\Delta| < 100$ GHz. We have confirmed in test calculations with unlimited $|\Delta|$, which include all couplings as small as $|\langle ...|V_{\rm dd}|...\rangle| > 10^{-6} \times n^{*4}/R^3$, that the described limitation of the sum in Eq. 2.5 does not change the calculated van der Waals shifts by more than about one percent. By restricting the sum in the described way, we find that typically of the order of hundreds of two-particle states $|n'', \ell'', j'', m''_{\rm j}\rangle \otimes |n', \ell', j', m'_{\rm j}\rangle$ still contribute, although the dominant contributions usually come from only five to ten two-particle states, with one or two of those often accounting for $70 - 90\%$ of the level shift.

[2] The angular momentum-dependent quantum defect, δ_ℓ, accounts for the deviation of the potential of a singly-charged alkali ion from a perfect Coulomb potential.

In our calculations, we have included single-particle basis states with principal quantum numbers over a restricted n-range and have verified that the inclusion of more bound states does not noticeably change the results. We have not included continuum states in our calculation. Continuum states are important in calculations of van der Waals shifts of atomic ground states or low-lying states, where in the sum in Eq. 2.5 there are no near-resonant terms with very small Δ. For instance, for basic estimates of ground-state level shifts, one may approximate all energy denominators by the ionization energy and use a closure relation to compute the sum in Eq. 2.5 [65]. The closure relation incorporates all continuum states. In contrast, for Rydberg-atom pairs the energy denominators in Eq. 2.5 vary from tens of MHz for the near-resonant two-particle states to about 10^{15} Hz for two-particle states near the ground state, leading to an enormous variation in the significance of terms. Typically, there are several near-resonant terms, and it is found that those dominate the van der Waals shifts of Rydberg atoms. Due to this resonant behavior the introduction of continuum states will not likely make a significant difference.

2.1.3 Computation of energy level shifts in nonzero electric fields

In cases where an external electric field is applied, the field-free eigenstates, $|n, \ell, j, m_{\rm j}\rangle$, are no longer eigenstates of the single-atom Hamiltonian. Therefore, to proceed with a perturbative calculation of the binary interaction energies, we first calculate the single-atom eigenstates of the Hamiltonian $H = H_{\rm at} + Ez$, where $H_{\rm at}$ is the field-free, single-atom Hamiltonian and $\mathbf{E} = E\hat{\mathbf{z}}$ is the applied electric field. We label the single-atom eigenstates as $|\lambda, m_{\rm j}\rangle$, where λ is an index which uniquely identifies each Stark state of a given $m_{\rm j}$. If two Rydberg atoms interact in the presence of an applied electric field, interaction energies occur that are both first and second order in the coupling matrix elements. In the following, we outline the calculation

of energy level shifts in an applied electric field for three cases: when a strong field induces permanent dipole moments in the atoms which may interact in first order, when a weak field induces an exact resonance for one interaction channel and produces a level shift in first order, and when the field is weak and non-resonant and the level shifts occur in second order.

In large (several V/cm for $45D_{5/2}$) electric fields, the Stark eigenstates are not states of definite parity and the diagonal single-atom matrix elements $\langle \lambda, m_\mathrm{j}|p_{\alpha,\mathrm{z}}|\lambda, m_\mathrm{j}\rangle$ of the dipole operator are nonzero. This leads to a first-order dipole-dipole interaction energy of the type

$$\Delta W^{(1)} = \langle \lambda, m_\mathrm{j}| \otimes \langle \lambda, m_\mathrm{j}|V_\mathrm{dd}|\lambda, m_\mathrm{j}\rangle \otimes |\lambda, m_\mathrm{j}\rangle \quad . \tag{2.6}$$

If the Stark eigenstates have large permanent electric dipole moments, $\langle \lambda, m_\mathrm{j}|p_{\alpha,\mathrm{z}}|\lambda, m_\mathrm{j}\rangle$, the level shift in Eq. 2.6 dominates.

In smaller electric fields ($\lesssim$ 1 V/cm for $45D_{5/2}$), the atoms do not have significant permanent electric dipole moments, yet the interactions may still produce level shifts which are first order in V_dd. In this scheme, called a Förster resonance, the electric field is used to tune two different two-particle states $|\lambda, m_\mathrm{j}\rangle \otimes |\lambda, m_\mathrm{j}\rangle$ and $|\lambda'', m_\mathrm{j}''\rangle \otimes |\lambda', m_\mathrm{j}'\rangle$ into exact resonance ($\Delta = W_{|\lambda', m_\mathrm{j}'\rangle} + W_{|\lambda'', m_\mathrm{j}''\rangle} - 2 \times W_{|\lambda, m_\mathrm{j}\rangle} = 0$). These resonances are referred to as Förster resonances. In the case of a Förster resonance, diagonalization of the two-particle Hamiltonian within the subspace of degenerate two-particle states leads to two mixed eigenstates with first-order dipole-dipole energy level shifts of

$$\Delta W^{(1)} = \pm\sqrt{2}\langle \lambda'', m_\mathrm{j}''| \otimes \langle \lambda', m_\mathrm{j}'|V_\mathrm{dd}|\lambda, m_\mathrm{j}\rangle \otimes |\lambda, m_\mathrm{j}\rangle \quad , \tag{2.7}$$

which can dominate all other level shifts. The $\sqrt{2}$ comes from the indistinguishability of the $|\lambda', m_\mathrm{j}'\rangle \otimes |\lambda'', m_\mathrm{j}''\rangle$ and $|\lambda'', m_\mathrm{j}''\rangle \otimes |\lambda', m_\mathrm{j}'\rangle$ states.

In cases where the Stark eigenstates have negligible permanent dipole moments and there are no electric-field-induced Förster resonances, there still exists a second-order van der Waals interaction of the type

$$\Delta W^{(2)} = -\sum_{\substack{\lambda', m_{\rm j}', \lambda'', m_{\rm j}'' \\ \Delta \neq 0}} \frac{|\langle \lambda'', m_{\rm j}''| \otimes \langle \lambda', m_{\rm j}'| V_{\rm dd} |\lambda, m_{\rm j}\rangle \otimes |\lambda, m_{\rm j}\rangle|^2}{\Delta} \tag{2.8}$$

which may lead to significant level shifts, similar to van der Waals interactions in zero applied field.

Since the single-particle dipole matrix elements $\langle \lambda', m_{\rm j}'| p_{\alpha,\beta} |\lambda, m_{\rm j}\rangle$ scale with effective principal quantum number n^* as n^{*2}, the two particle matrix elements scale with n^* and R as:

$$\langle \lambda'', m_{\rm j}''| \otimes \langle \lambda', m_{\rm j}'| V_{\rm dd} |\lambda, m_{\rm j}\rangle \otimes |\lambda, m_{\rm j}\rangle \propto n^{*4}/R^3 \quad . \tag{2.9}$$

Although, strictly speaking, n is not a good quantum number in a substantial electric field (hence the state labels $|\lambda, m_{\rm j}\rangle$), this scaling law is approximately true if n^* is taken to be the n^* value of the zero-field state in the Stark map that is adiabatically connected to the state in question. Additionally, the infinite-separation energy denominator, Δ, in Eq. 2.8 effectively scales with n^* as n^{*-3}. Thus, we have the general n^* and R scaling for interactions in the presence of an applied electric field. In a field which induces permanent dipole moments or a Förster resonance, the level shifts scale as:

$$\Delta W^{(1)} \propto n^{*4}/R^3 \quad . \tag{2.10}$$

In fields for which no interaction channels are resonant and the atoms have no permanent dipole moments, the level shifts scale as:

$$\Delta W^{(2)} \propto n^{*11}/R^6 \quad . \tag{2.11}$$

These are equivalent to the usual dipole-dipole and van der Waals scaling, respectively.

Much of the research described in this thesis deals with interactions among Rydberg atoms in zero applied electric field. However, the experiments in Chapters IV and V involve Rydberg-Rydberg interactions in the presence of a Förster resonant field and in the presence of a small, nonresonant electric field. Therefore, in the following I present interaction potentials for two-body Rydberg-Rydberg interactions for three cases: in zero applied field, in a Förster resonant electric field, and in a weak electric field where atoms interact via second-order van der Waals interactions. The case in which the Rydberg atoms are given permanent electric dipole moments will not be discussed; however, interaction potentials and a discussion of the relevance of these potentials to Rydberg excitation blockade experiments is discussed in detail in Ref. [66].

2.2 Energy level shifts in zero electric field

2.2.1 Rb $nD_{5/2}$ Rydberg states

In all of the experiments described in this thesis, Rydberg excitations are created via a two-step process from the ground S-state to $S_{1/2}$, $D_{3/2}$, and $D_{5/2}$ Rydberg states, through an intermediate P-state. Since the transitions into $D_{5/2}$ states have the highest oscillator strength, these states are often studied experimentally [10, 11, 15] and they are used for most of the experiments presented below. Thus, I first investigate the binary interaction-induced energy level shifts for $nD_{5/2}$ Rydberg states of rubidium in zero applied electric field.

In Fig. 2.2, I present scaled binary energy level shifts of $2 \times |nD_{5/2}, m_{\rm j}\rangle$ states as a function of n for $\theta = 0$ (a) and as a function of θ for $n = 60$ (b). The scaled level

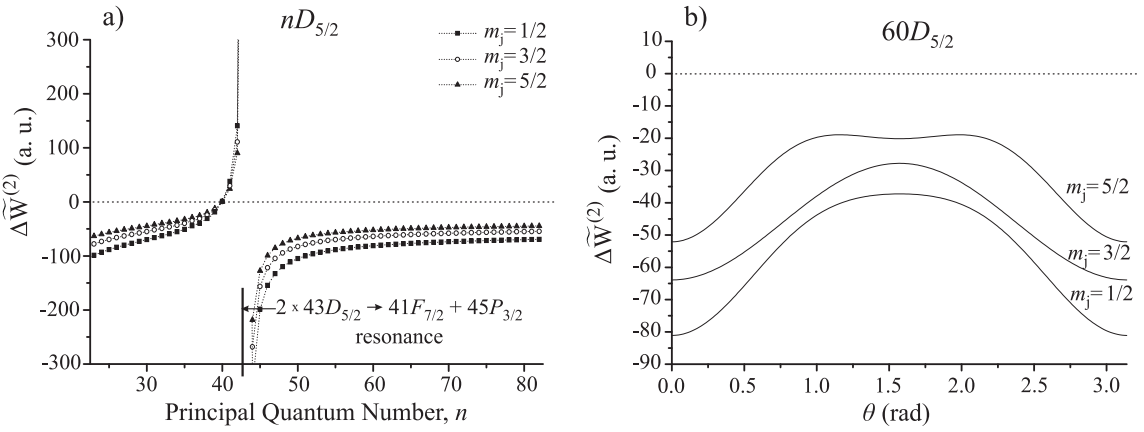

Figure 2.2: a) Scaled energy level shifts, $\Delta\widetilde{W}^{(2)}$, of $2 \times |nD_{5/2}, m_j\rangle$ states as a function of n for different m_j quantum numbers and $\theta = 0$. b) $\Delta\widetilde{W}^{(2)}$ of $2 \times |60D_{5/2}, m_j\rangle$ states as a function of θ for different m_j quantum numbers.

shifts are defined by

$$\Delta\widetilde{W}^{(2)}(n, \ell, j, m_j, \theta) \equiv \Delta W^{(2)}(n, \ell, j, m_j, R, \theta) \times (R^6/n^{*11}) \quad , \tag{2.12}$$

with $\Delta W^{(2)}(n, \ell, j, m_j, R, \theta)$ given in Eq. 2.5. Due to the scaling, the scaled shift $\Delta\widetilde{W}^{(2)}$ does not depend on R.

In Fig. 2.2(a), one can distinguish between regions of qualitatively different behavior. In the ranges $n \gtrsim 50$ and $n \lesssim 35$, the scaled energy shift is roughly a constant function of n for any given m_j, while in the range $35 \lesssim n \lesssim 50$ it is characterized by a prominent dispersive feature. These differences can be attributed to the number of relevant channels in Eq. 2.5 and their dependence on n.

In the ranges $n \gtrsim 50$ and $n \lesssim 35$, the channel,

$$2 \times nD_{5/2} \rightarrow (n-1)F_{7/2} + (n+1)P_{3/2} \quad , \tag{2.13}$$

dominates all other channels in the sum in Eq. 2.5 and accounts for roughly $70-80\%$ of the total energy shift. The product-state sum indices m_j' and m_j'' of Eq. 2.5 are omitted in the channel notation used in Eq. 2.13. In many cases the channel in Eq. 2.13 has multiple sub-channels that correspond to different dipole-allowed

combinations of $m_{\rm j}'$ and $m_{\rm j}''$. The allowed sub-channels have fairly large coupling strengths $|\langle ...|V_{\rm dd}|...\rangle| \sim 1 \times n^{*4}/R^3$, where the numerical prefactor "1" depends somewhat on θ and on the $m_{\rm j}$ values. However, the allowed sub-channels also have large energy denominators ($\Delta \approx 1$ GHz $\times(\frac{59}{n^*})^3$), which limit the magnitude of the resultant second-order shift. Because of the n^{*4}/R^3 scaling of the couplings and the $1/n^{*3}$ scaling of Δ [3], the contribution to the second-order shift due to this strong, highly-detuned channel scales as n^{*11}/R^6. Since in the ranges $n \gtrsim 50$ and $n \lesssim 35$ this contribution dominates, the scaled shifts $\Delta\widetilde{W}^{(2)}$ are approximately constant, as observed in Fig. 2.2.

In the range $35 \lesssim n \lesssim 50$, a different, nearly resonant channel significantly contributes to the perturbative sum and interrupts the n^{*11}/R^6 scaling of the energy shifts. This channel,

$$2 \times nD_{5/2} \rightarrow (n-2)F_{7/2} + (n+2)P_{3/2} \quad , \tag{2.14}$$

has a coupling strength (for $\theta = 0$)

$$|\langle ...|V_{\rm dd}|...\rangle| \sim 0.36 \times n^{*4}/R^3 \tag{2.15}$$

in the vicinity of $n = 43$ and a small, nearly resonant energy denominator of

$$\Delta \approx 79(n^* - 41.8) \text{ MHz} \quad , \tag{2.16}$$

i.e. the energy denominator undergoes a zero crossing between $n = 43$ and 44. In the vicinity of $n = 43$, the scaled level shift of the state $2 \times |nD_{5/2}, m_{\rm j} = 5/2\rangle$ due to the channels in Eqs. 2.13 and 2.14 approximately follows, for $\theta = 0$,

$$\Delta\widetilde{W}^{(2)} \approx -\left[37 + \frac{149}{(n^* - 41.8)}\right] \quad . \tag{2.17}$$

In the range $40 \leq n \leq 47$, the level shift due to the near-resonant channel (Eq. 2.14 and second term in Eq. 2.17) is greater than that due to the off-resonant channel

(Eq. 2.13 and first term in Eq. 2.17). Since the level shifts due to these two terms have different n-dependencies, the total shift does not follow a simple scaling law in this n-range.

The scaled level shifts in Fig. 2.2 are obtained perturbatively, and therefore care must be taken when interpreting and using them. For any given n and R, one may determine the absolute van der Waals level shift (in atomic units) from Fig. 2.2 by multiplying the scaled shift with n^{*11}/R^6. However, the result is only valid if, for the significant terms in the sum in Eq. 2.5, the coupling strengths $|\langle ...|V_{\rm dd}|...\rangle|$ are smaller than their energy denominators Δ. Generally, for each two-particle Rydberg state $2 \times |n, \ell, j, m_{\rm j}\rangle$ a critical radius $R_{\rm c}$ exists such that the perturbative method is valid for $R > R_{\rm c}$. Similar considerations apply to Figs. 2.3 and 2.4 below.

The scaled level shifts of the two-particle states $2 \times |60D_{5/2}, m_{\rm j}\rangle$ as a function of θ are shown in Fig. 2.2(b). Analogous curves for different $2 \times |nD_{5/2}, m_{\rm j}\rangle$ states may be obtained approximately by multiplying the curves shown in Fig. 2.2(b) by the ratios

$$\frac{\Delta\widetilde{W}^{(2)}(n, l = 2, j = 5/2, m_{\rm j}, \theta = 0)}{\Delta\widetilde{W}^{(2)}(n = 60, l = 2, j = 5/2, m_{\rm j}, \theta = 0)} \quad , \tag{2.18}$$

which follow from the data shown in Fig. 2.2(a). The similarity among the curves $\Delta\widetilde{W}^{(2)}(n, l = 2, j = 5/2, m_{\rm j}, \theta)$ vs. θ for different n reflects the fact that the dominant channels, Eqs. 2.13 and 2.14, have the same angular-momentum quantum numbers. Thus, the same terms in Eq. 2.4 have nonzero matrix elements for each channel.

2.2.2 Rb $nD_{3/2}$ and $nS_{1/2}$ Rydberg states

In this subsection I examine the scaled energy level shifts, $\Delta\widetilde{W}^{(2)}$, as a function of n and θ for excitation into $nD_{3/2}$ and $nS_{1/2}$ Rydberg states. In parts (a) of Figs. 2.3 and 2.4, I plot the scaled level shifts as a function of n for $\theta = 0$. In parts (b) of

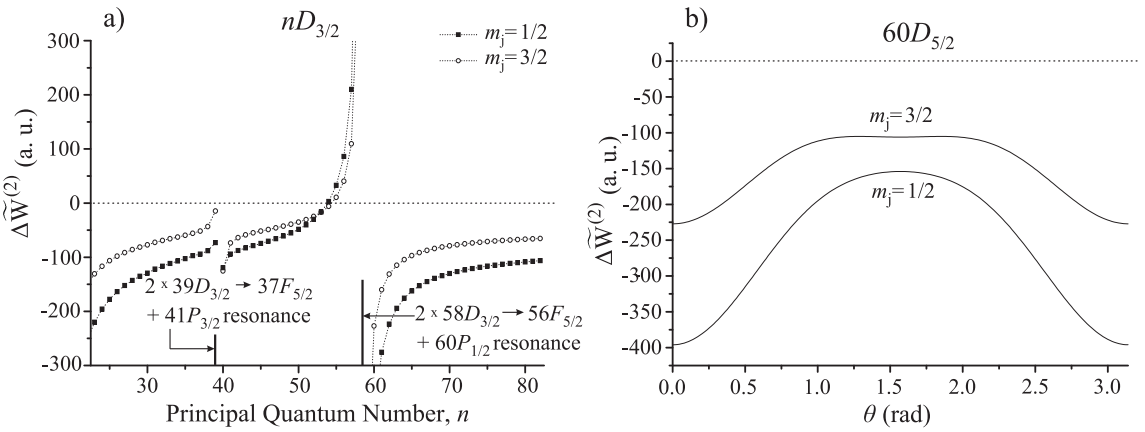

Figure 2.3: a) Scaled energy level shifts, $\Delta\widetilde{W}^{(2)}$, of $2 \times |nD_{3/2}, m_j\rangle$ states as a function of n for different m_j quantum numbers and $\theta = 0$. b) $\Delta\widetilde{W}^{(2)}$ of $2 \times |60D_{3/2}, m_j\rangle$ states as a function of θ for different m_j quantum numbers.

Figs. 2.3 and 2.4, I plot the scaled level shifts as a function of θ at fixed $n = 60$. In the following, I discuss some qualitative features of these plots. The level shifts for excitation into $nP_{3/2}$ and $nP_{1/2}$ states are not discussed here, but are examined in detail in Ref. [66].

The scaled energy level shifts of the states $2 \times |nD_{3/2}, m_j\rangle$, shown in Fig. 2.3(a), exhibit a behavior similar to that of the states $2 \times |nD_{5/2}, m_j\rangle$, except that two interaction channels, $2 \times nD_{3/2} \rightarrow (n-2)F_{5/2} + (n+2)P_{3/2}$ and $2 \times nD_{3/2} \rightarrow (n-2)F_{5/2} + (n+2)P_{1/2}$, become nearly resonant at $n = 39$ and $n = 58$, respectively. The resonances manifest themselves as dispersive-shaped features in the graph of $\Delta\widetilde{W}^{(2)}$. The resonance centered at $n = 39$ is weaker than the one at $n = 58$ due to a smaller coupling strength, $|\langle ...|V_{dd}|...\rangle|$. Away from these two resonances, the scaled level shift varies little with n because an off-resonant channel with large coupling strength, $2 \times nD_{3/2} \rightarrow (n-1)F_{5/2} + (n+1)P_{1/2}$, is responsible for the majority ($\gtrsim 60\%$) of the level shift. The dependence of the scaled level shifts of $2 \times |nD_{3/2}, m_j\rangle$ on θ, shown in Fig. 2.3(b), resembles that of $2 \times |nD_{5/2}, m_j\rangle$, shown in Fig. 2.2(b). In both cases, the level shifts are always negative and only moderately sensitive to θ.

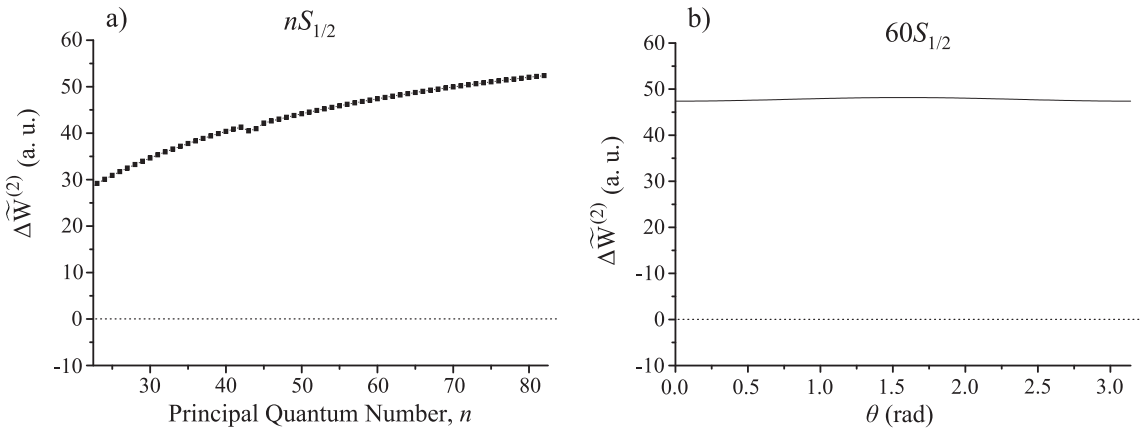

Figure 2.4: a) Scaled energy level shifts, $\Delta\widetilde{W}^{(2)}$, of $2 \times |nS_{1/2}, m_{\rm j} = 1/2\rangle$ states as a function of n for $\theta = 0$. b) $\Delta\widetilde{W}^{(2)}$ of $2 \times |60D_{5/2}, m_{\rm j} = 1/2\rangle$ states as a function of θ.

The considerable difference in the respective magnitudes of the level shifts is due to the fact that the case $n = 60$ happens to be quite close to a resonance in Fig. 2.3(a) but not in Fig. 2.2(a).

The scaled level shifts of the states $2 \times |nS_{1/2}, m_{\rm j} = 1/2\rangle$, shown in Fig. 2.4(a) and (b), are qualitatively different than the shifts for D-states in that they are large and positive for all n and θ. Four channels of the type $2 \times nS_{1/2} \rightarrow nP_{\rm j'} + (n-1)P_{\rm j''}$ account for most of the level shift in the displayed region, where $\{{\rm j'}, {\rm j''}\} = 1/2$ or $3/2$. None of the channels become resonant at any n in the displayed range. The level shifts of the states $2 \times |nS_{1/2}, m_{\rm j} = 1/2\rangle$ are almost entirely independent of θ, reflecting the spherical symmetry of s-state wavefunctions. (The shifts are not entirely spherically symmetric because of spin orientation effects and fine-structure coupling).

In all cases discussed so far, the detailed values of the infinite-separation energy defects, Δ, depend sensitively on the accuracy and precision of quantum defects used in the calculations. In almost all cases I have used the most currently published quantum defects for Rb from Refs. [67, 68]. Comparing the results to values obtained with alternative sets of quantum defects from other sources, *i.e.* Ref. [1] and Ref. [69],

we have seen that typically the energy detunings vary by amounts of order tens of MHz. Variations of that size significantly affect the energy shifts only very close to the resonances in Figs. 2.2 and 2.3. This is the reason that the figures in Ref. [66] have resonant n-values that differ from the resonant n-values given here by ± 1.

2.2.3 Experimental implications of the level-shift calculations

Figures 2.2, 2.3 and 2.4 enable one to choose Rydberg states with properties that are appropriate for specific applications. For example, in quantum-information-processing applications, states with level shifts that are large and relatively insensitive to variations in θ and magnetic quantum numbers are desirable. If Rydberg states with these interaction properties are used, experimental variations in angle and polarization will not translate into excessive gate inefficiencies. Inspecting Figs. 2.2-2.4 it is seen that large shifts may be obtained by choosing a principal quantum number near an interaction resonance, *e.g.* near $n = 43$ for excitation into $D_{5/2}$-states. Another way to achieve large shifts is to exploit the generic van der Waals scaling (absolute shift $\propto n^{*11}$ for sufficiently large atom-atom separation), which in all cases studied leads to large shifts for $n \gtrsim 70$. Rydberg atoms in $nS_{1/2}$ states appear to be particularly attractive candidates, because their energy shifts are large, near-isotropic, and positive, leading to mutual repulsion between atoms and therefore inhibition of ionizing interactions triggered by attractive forces between atoms [51].

Figures 2.2, 2.3, and 2.4 can also be used to select Rb Rydberg states in applications of dense Rydberg-atom gases and cold plasmas. In cases where state-changing and ionizing collisions between atoms are not desired, one looks for positive energy level shifts with weak dependence on magnetic quantum numbers and θ. These properties lead to repulsive forces between atoms that inhibit close, inelastic collisions.

Among the cases studied, all $nS_{1/2}$ states and nD states in limited, small ranges of n ($n = 41 - 43$ for $D_{5/2}$ and $n = 55 - 57$ for $D_{3/2}$) meet these requirements. Alternatively, one may accelerate the onset of collision-induced effects by choosing states with negative, large, and resonantly-enhanced shifts, *e.g.* $nD_{5/2}$ with $n \approx 44$ or $nD_{3/2}$ with $n \approx 59$. A dense cloud of Rydberg atoms initially prepared in one of these states will exhibit a high initial rate of atom-atom collisions triggered by attractive forces between the atoms, leading to rapid ionization and accelerated transition of the cloud into a cold plasma [47–49, 51, 70]. Finally, in applications where strong interactions are not desired, one may choose a state for which the energy shifts contributed by two different channels cancel, resulting in a small net shift. Examples include the $54D_{3/2}$ and $40D_{5/2}$ states. These issues are experimentally explored in Chapter VI.

2.3 Energy level shifts in nonzero electric fields

2.3.1 Förster resonances

As mentioned above, one may enhance interaction energies by applying a relatively weak electric field to tune a Rydberg-Rydberg collisional interaction, such as the ones described in Sect. 2.2, into exact resonance [2, 6, 7, 24, 71], thereby inducing a Förster resonance. For sufficiently large atom-atom separations, the resultant resonant shift dominates any other van der Waals shifts that may also be present. As an example, we consider the channel $2 \times nD_{5/2} \rightarrow (n-2)F + (n+2)P_{3/2}$. In this case, the electric fields required to tune these interactions into exact resonance are too small to change the angular-momentum-character of the involved P- and D-states and to break their fine-structure coupling, as illustrated in the Stark map for $n = 45$ shown in Fig. 2.5 (upper two panels). As a result, in weak electric fields the P- and D-states are not significantly perturbed, and we may use electric-field-free quantum numbers

(ℓ, j, and $m_{\rm j}$) to identify those states. However, the very small fine-structure of the involved F-state is broken in the electric-field range of interest, as is apparent in the bottom panel of Fig. 2.5. Therefore, we label the F-states by magnetic quantum numbers for electron spin and orbital angular momentum, $m_{\rm s}$ and m, respectively. (In some cases, even the orbital-angular-momentum character of the involved F-state becomes significantly perturbed.)

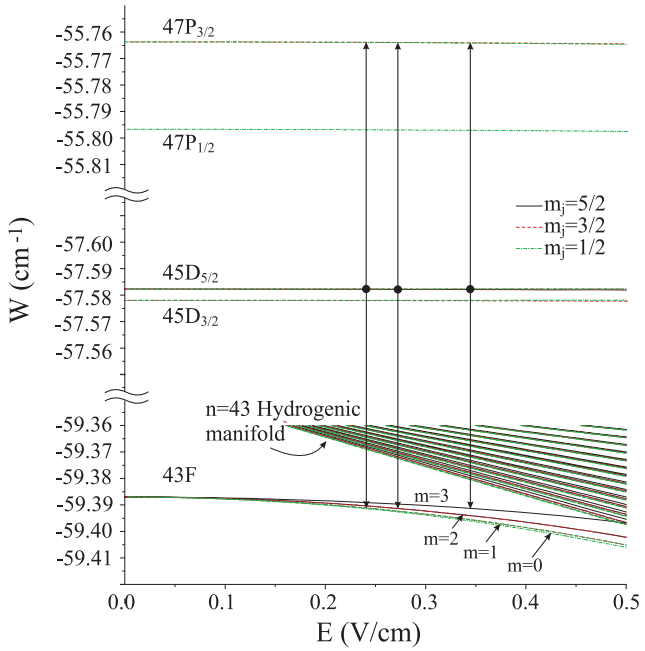

Figure 2.5: Stark map showing the detailed energy structure of the $45D$, $47P$, and $43F$ states. The vertical arrows indicate the resonant transitions corresponding to the interaction channels in Eq. 2.19.

The detailed coupling scheme of the Förster resonances $2 \times nD_{5/2} \rightarrow (n-2)F + (n+2)P_{3/2}$ is most transparent if we assume that the $2 \times |nD_{5/2}\rangle$ state has $m_{\rm j} = 5/2$. In this case, the operator in Eq. 2.4 allows only the three couplings:

$$2 \times |nD_{5/2}, m_{\rm j} = 5/2\rangle \rightarrow |(n+2)P_{3/2}, m_{\rm j} = 3/2\rangle + |(n-2)F, m_{\rm s} = 1/2, m\rangle \quad , \quad (2.19)$$

where $m = \{1, 2, 3\}$. In zero electric field, the couplings have infinite-separation energy defects with magnitudes ranging from 0 to ~ 400 MHz for $40 \leq n \leq 60$, as shown in Fig. 2.6(a). In the range $n \geq 44$ they can be tuned into resonance by appli-

cation of electric fields of up to about 0.4 V/cm, which tune the infinite-separation energy defects downward toward negative values. The tuning largely occurs through the Stark shifts of the F-levels, which have, due to their small quantum defect, the largest electric polarizabilities among the involved states ($\alpha \approx -2.1$ GHz/(V/cm)^2, -1.7 GHz/(V/cm)^2 and -1.1 GHz/(V/cm)^2 for $43F$, $m = 1$, 2, 3, respectively). Since the polarizabilities depend on m, the couplings in Eq. 2.19 come into resonance at slightly different electric fields, as shown in Fig. 2.6(b). By inspecting Eq. 2.4, it is seen that the coupling strengths follow angular and radial dependencies $-\frac{3}{2}\chi_1 \sin^2(\theta)/R^3$, $-\frac{3}{\sqrt{2}}\chi_2 \sin(\theta)\cos(\theta)/R^3$, and $\chi_3(1-\frac{3}{2}\sin^2(\theta))/R^3$, with reduced coupling strengths $\chi_{\rm m}$ for $m = 1$, 2, 3. In Fig. 2.6(c) I show the reduced coupling strengths scaled by n^{*4} at the resonant electric fields as a function of n. In the range $44 \leq n \lesssim 48$, the scaled χ-values are fairly constant, reflecting the fact that in this range of n the F-states $|(n-2)F, m_{\rm s} = 1/2, m\rangle$ with $m = 1, 2, 3$ are mostly unperturbed. For $n \gtrsim 49$ the state $|(n-2)F, m_{\rm s} = 1/2, m = 3\rangle$ becomes increasingly mixed with high-ℓ hydrogenic states, leading to a spread of F-character over multiple states and, therefore, to an abrupt drop of the χ-value of the strongest resonance (χ_3). The resonances involving $|(n-2)F, m_{\rm s} = 1/2, m = 2\rangle$ and $|(n-2)F, m_{\rm s} = 1/2, m = 1\rangle$ exhibit similar reductions in strength at somewhat higher values of n.

If one of the sub-channels in Eq. 2.19 is exactly resonant, the resultant level shifts of the two-atom states are first-order and are given by $\sqrt{2}$ times the coupling strength of the resonant channel (see Eq. 2.7). The two-particle states that correspond to the two eigenvalues in Eq. 2.7 are given by the symmetric and antisymmetric combinations of $2 \times |nD_{5/2}, m_{\rm j} = 5/2\rangle$ and $|(n-2)F, m_{\rm s} = 1/2, m\rangle \otimes |(n+2)P_{3/2}, m_{\rm j} = 3/2\rangle$. For instance, at $n = 45$, $R = 5$ μm, $\theta = 0$, and $E = 0.34$ V/cm the resonance for $m = 3$ generates two such superposition states at energy separations of about

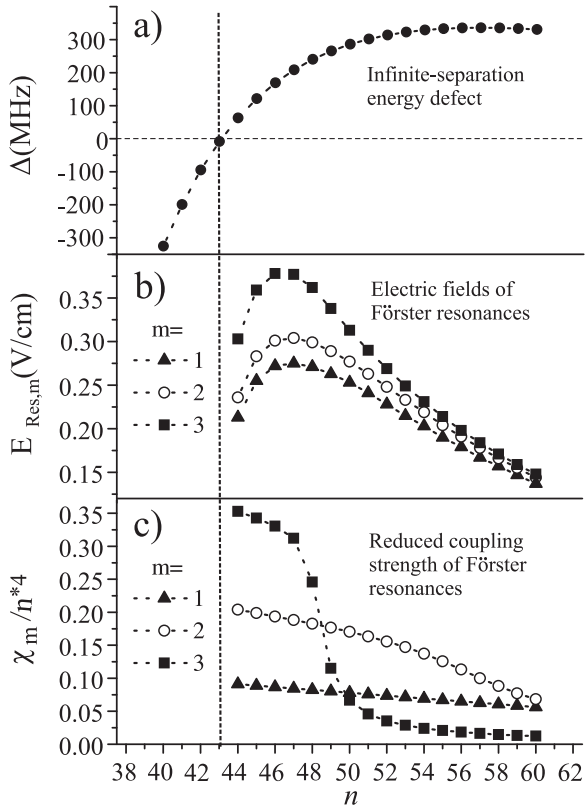

Figure 2.6: a) Infinite-separation energy defects, Δ, of the channel $2\times nD_{5/2} \rightarrow (n-2)F+(n+2)P_{3/2}$ vs n. b) Electric fields, $E_{\mathrm{Res,m}}$ at which the magnetic sub-channels identified in Eq. 2.19 become resonant. c) Scaled reduced coupling strengths, χ_{m}/n^{*4}, $m \in \{1,2,3\}$, of the channels in panel b) vs n. (The values of Δ in part b) differ slightly from those in Fig. 2.7 because an older value for the F-state quantum defect [1] was used. Using the most recent F-state quantum defect will change these values by about 5%.)

± 15 MHz from the interaction-free energy.[3] In comparison, the van der Waals shift of the state $2 \times |45D_{5/2}, m_{\mathrm{j}} = 5/2\rangle$ at $E = 0$ would only be of the order of 1 MHz. Therefore, strong binary Rydberg-Rydberg interactions may be turned on and off by tuning interactions of the type in Eq. 2.19 into and out of resonance by switching weak electric fields. This technique of controllably enhancing the Rydberg-Rydberg interaction strength is used in Chapters IV and V.

[3] To calculate this, I used Eq. 2.7 and χ_{m} from Fig. 2.6.

2.3.2 van der Waals shifts in electric fields

The channels identified in Eq. 2.19 cause some shifts even if the electric field, E, does not induce an exact Förster resonance. For sufficiently large separation, R, these level shifts can be calculated in second order, as a function of θ and E, using Eq. 2.8.

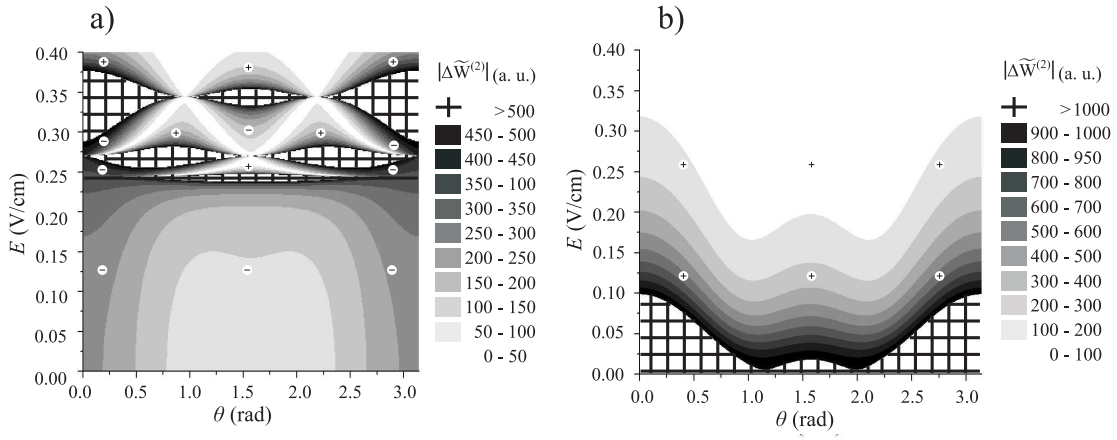

Figure 2.7: Scaled energy level shifts, $\Delta\widetilde{W}^{(2)}$ of the $2\times|45D_{5/2}, m_{\rm j}=5/2\rangle$ (a) and $2\times|45D_{5/2}, m_{\rm j}=5/2\rangle$ (b) states as a function of θ and the applied electric field. The magnitude of the scaled shifts are shown on the right and the signs of the shifts are indicated on the plots.

As an example, in Fig. 2.7a I plot the energy level shift of the state $2\times|45D_{5/2}, m_{\rm j}=5/2\rangle$ as a function of E and θ. In the range $E \lesssim 0.20$ V/cm, the van der Waals shifts are always negative and have a weak dependence on θ. The interaction channels in Eq. 2.19 generate prominent resonant features that follow angular patterns proportional to $[\chi_1 \frac{3}{2}\sin^2(\theta)]^2$ near 0.24 V/cm, $\propto [\chi_2 \frac{3}{\sqrt{2}}\sin(\theta)\cos(\theta)]^2$ near 0.27 V/cm, and $\propto [\chi_3(1-\frac{3}{2}\sin^2(\theta))]^2$ near 0.34 V/cm. (Note that these fields correspond to the Förster resonant fields given in Fig. 2.6b and that the angular patterns correspond to the squares of the angular dependencies mentioned in the discussion of Eq. 2.19.) For electric fields just below a resonance, the shifts are negative, because the energy defect, Δ, of the nearest-resonant term is > 0. For electric fields just above

a resonance, the shifts tend to be positive, because the energy defect, Δ, of the nearest-resonant term is < 0. Between resonances, the sign of the second-order shift varies as a function of θ due to the competing effects of two nearby resonances with different angular profiles, one producing positive and the other producing negative second-order shifts.

As a second example, I plot the level shift of the state $2 \times |43D_{5/2}, m_{\rm j} = 5/2\rangle$ in Fig. 2.7b. This figure will be relevant to the discussion of Sect. 5.4. In contrast to the case of $45D_{5/2}$, the level shifts for $43D_{5/2}$ are positive for the entire electric field range displayed and there exists a near Förster resonance in zero applied field. The dominant interaction channel at $n = 43$ (Eq. 2.14) has an energy denominator of about -10 MHz (see Eq. 2.16) which becomes more negative with increasing E until, at a field $E \sim 0.45$ V/cm, it is no longer the dominant channel and the level shift due to several channels cancel and produce a small net shift. Thus, there are no exact Förster resonances for $43D_{5/2}$ in the range $0 \leq E \leq 0.45$ V/cm.[4]

I have investigated in great detail van der Waals shifts of other quantum states in an applied electric field. The resonances of the states $2 \times |nD_{5/2}, m_{\rm j} = 3/2\rangle$ and $2 \times |nD_{5/2}, m_{\rm j} = 1/2\rangle$ are qualitatively similar to those of the states $2 \times |nD_{5/2}, m_{\rm j} = 5/2\rangle$ discussed here, but have more than three allowed angular-momentum sub-channels (up to eight) and occur at somewhat different electric fields. Many more Förster resonances occur at fields larger than the ones displayed in Fig. 2.7a. However, due to the increasingly complicated underlying Stark maps, these higher-field Förster resonances follow rather erratic patterns and are usually weak. Therefore, any experimental applications of Förster resonances will likely employ simple cases, such as the ones discussed in this section.

[4] An exact Förster resonance for $43D_{5/2}$ may, however, be realized using Stark shifts induced by AC rather than DC electric fields. See for example Ref. [72].

CHAPTER III

Creating and analyzing cold Rydberg-atom gases

In this thesis, we are concerned with ensembles of Rydberg atoms in which atom-atom interactions dominate the excitation and evolution dynamics. Thus, we are mainly interested in ensembles where thermal motion of the Rydberg atoms is negligible, *i.e.* ensembles of cold Rydberg atoms. Rydberg atoms may be produced when an atom absorbs energy from either a collisional partner or its surroundings and one of its valence shell electrons is promoted into a state of high principal quantum number n [3]. However, since there are, at present, no techniques available for the active cooling of Rydberg atoms, the only appropriate method for the preparation of cold Rydberg atoms is photoexcitation of laser-cooled ground-state atoms. In this section I describe the methods we use to obtain cold samples of ground-state atoms, photoexcite these atoms into Rydberg states, and detect the number of Rydberg excitations created and their internal-state distribution.

3.1 Laser cooling and trapping of ground-state atoms

3.1.1 Magento-optical traps

In all experiments presented below, a vapor-cell magneto-optical trap (MOT) is used to laser cool and trap ensembles of ^{85}Rb ground-state atoms. The MOT is the most widely used, versatile, and simplest method of obtaining ensembles of cold ($\lesssim$

1 mK) ground-state atoms. The MOT cools and traps atoms as a result of position-dependent radiation pressure forces. The vapor-cell MOTs we employ consist of a pair of anti-Helmholtz coils wrapped around rubidium vapor cells and three pairs of counterpropagating and suitably σ-polarized laser beams [73]. The coils produce a quadrupole magnetic field of the form $B(r) = (-\alpha x/2, -\alpha y/2, \alpha z)$ (with $\alpha = 30 - 55$ Gauss/cm) and thus induce a linear Zeeman shift of the atomic states with non-zero magnetic quantum number, $m_{\rm F}$. The laser beams propagate in the $\pm x$, $\pm y$, and $\pm z$ directions, and are red-detuned from the transition $5S_{1/2}$, $F = 3 \rightarrow 5P_{3/2}$, $F' = 4$ by about three times the natural linewidth, $\gamma = 6$ MHz. The beams are σ-polarized in a way that an atom displaced from the trap center in any given direction predominantly scatters light from the laser beam that provides a dissipative radiation-pressure force pointing towards the trap center. This property is achieved by a combination of optical pumping into the extreme $m_{\rm F}$ sublevels and the red-shift of the dominant transition due to the Zeeman effect. A schematic illustration of the operation of a MOT is shown in Fig. 3.1. Details on the experimental implementation of a MOT are provided in [5, 73].

Our vapor-cell MOTs yield densities of ^{85}Rb ground-state atoms of order 10^{10} cm^{-3} at temperatures near the Doppler limit ($\sim 140\mu$K or an average thermal velocity of 12 cm/s [5]). The MOT has a diameter of ~ 500 μm and contains $\sim 10^6$ atoms. In the applications described below, it is often beneficial to increase the MOT density and atom number above these values. MOT atom numbers and densities can be increased using a double-trap design, in which a secondary, ultra-high-vacuum MOT is loaded by a cold atomic beam extracted from a primary, vapor-loaded trap. In this design, most atoms entering the range of the secondary MOT have a velocity less than the MOT capture velocity (~ 10 m/s [5]), while the background pressure

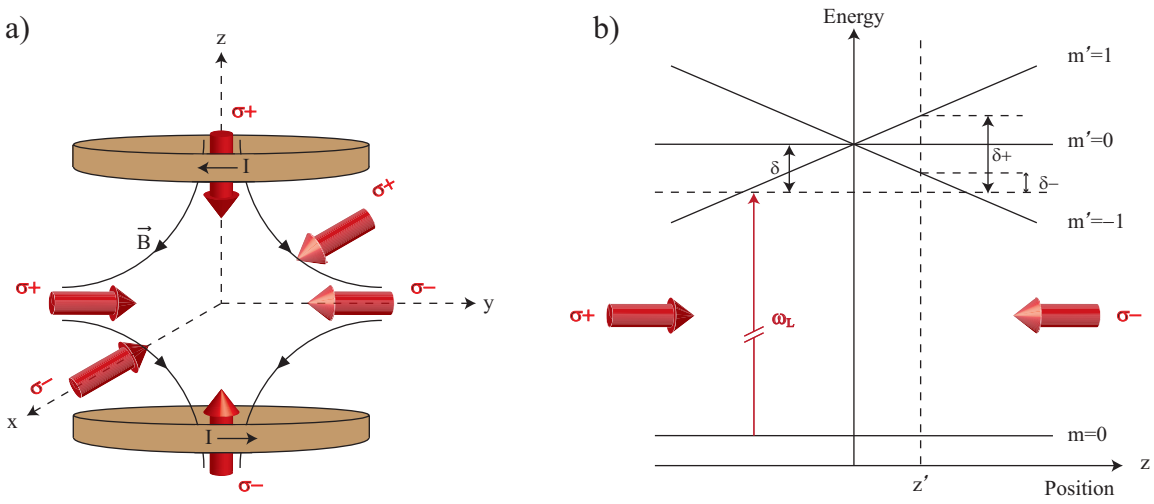

Figure 3.1: a) Spatial configuration of laser beams and magnetic field coils for a magneto-optical trap. b) Energy-level diagram of relevant atomic levels in a MOT configuration, illustrating cooling and trapping along the z axis. Fine structure and hyperfine structure of the involved states is neglected.

and the collision-induced atom loss rate are suppressed. Due to these factors, the densities and atom numbers achievable in double-MOT systems are larger than those in plain vapor-cell MOTs.

The double-MOT system used here is of the so-called LVIS type (Low Velocity Intense Source), first demonstrated in Ref. [74]. An LVIS can be implemented in several ways [74–78]; here we employ the strategy first described in Refs. [75, 76]. We use a collimated "pusher" beam which is $\sigma+$-polarized so it resonantly drives the $5S_{1/2},\ |F = 3, m_{\rm F} = 3\rangle \rightarrow 5P_{3/2},\ |F' = 4, m'_{\rm F} = 4\rangle$ cycling transition in ^{85}Rb. The beam exerts a radiation pressure force on the pre-cooled atoms trapped in the primary MOT and expels them with a relatively low velocity (~ 10 m/s) towards the secondary MOT. Thus, the pusher beam forms a directed, cold atomic beam from which the secondary MOT may be loaded.

In order to minimize unwanted deflection of the cold atomic beam due to radiation pressure forces caused by the near-resonant primary MOT trapping beams, we simultaneously pulse off the primary MOT trapping beams and pulse on the pusher

beam for 20 ms each experimental cycle, which is one-tenth of the cycle. For the remainder of each cycle, the primary MOT re-collects atoms to be used in the next loading cycle. In this way, we are able to achieve secondary MOTs with density and atom number of 5×10^6 and $\sim 4 \times 10^{10}\text{cm}^{-3}$, respectively. Absorption images of the secondary MOT with the pusher beam disabled (a) and enabled (b) are shown in Fig. 3.2, illustrating the increase in density and atom number of the secondary MOT when it is loaded from a cold atomic beam. Details on the technique of absorption imaging, including how it may be used to compute the density of clouds of cold atoms, may be found in Refs. [79, 80].

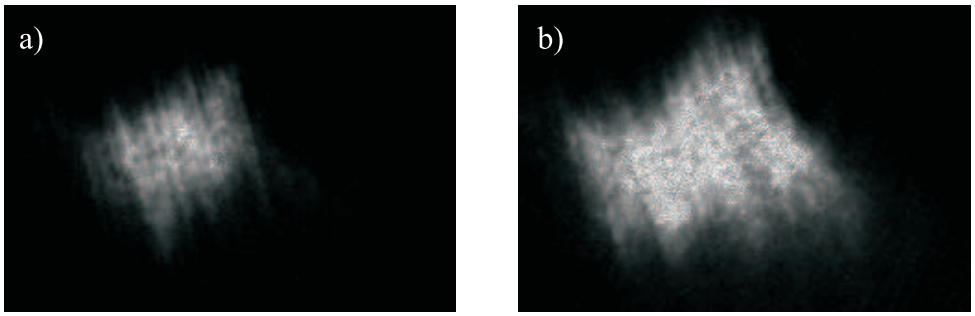

Figure 3.2: a) An absorption image of the secondary MOT with loading only from the rubidium background vapor. There is no loading from the LVIS. b) An absorption image of the secondary MOT and with loading from the LVIS. The MOT in (a) has 2×10^6 atoms and a density of $3 \times 10^{10}\text{cm}^{-3}$, while the MOT in (b) has 5×10^6 atoms and a density of $4 \times 10^{10}\text{cm}^{-3}$.

3.1.2 Optical dipole traps

For some of the experiments described below (Sect. 4.3, Chapter V, and Sect. 6.4) it is not sufficient to create Rydberg excitations from ensembles of atoms in a MOT. In these experiments it is necessary to achieve even higher ground-state atom densities than are possible in a double-MOT system and to employ atomic clouds that have a much smaller width. Additionally, small, dense atom clouds with relatively few Rydberg excitations may more readily be applied to quantum information processing schemes with few qubits than large systems with many excitations. For these

reasons, we implement an optical dipole trap [81–83] to realize cigar-shaped ground-state atom clouds with peak densities of $\sim 4 - 5 \times 10^{11}$ cm^{-3}, atom numbers of $\sim 3 \times 10^4$, and highly uniform, narrow spatial profiles with widths of order 10 μm.

Optical dipole traps rely on the electric-dipole interaction between an applied light field and the induced dipole moment of an atom. An optical dipole trap is often realized by focusing an intense laser beam that is highly red-detuned from the dominant ground to first excited state transition through an ensemble of pre-cooled atoms[1] (such as atoms in a MOT). The atoms will collect in the most intense part of the beam (*i.e.* in the beam waist) achieving a smaller and higher density atomic ensemble than is possible using a MOT.

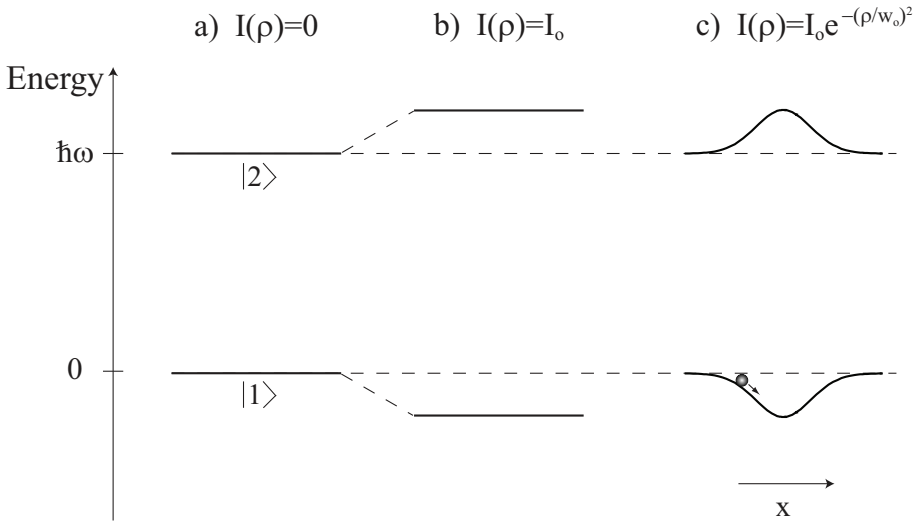

Figure 3.3: The energy level structure of a two-level atom as a function of position in the presence of red-detuned laser light of intensity $I(\rho)$ (ρ is the cylindrical coordinate). a) Intensity = 0 b) constant intensity c) Gaussian intensity profile. For a light field with a Gaussian intensity profile, an attractive potential well forms for ground-state atoms.

To understand the operation of an optical dipole trap, it is useful to consider the effect of the intense, far off-resonant laser light on the energy level structure of a two-level atom [84]. The Schrödinger equation for the probability amplitudes of

[1]Optical dipole traps are not deep enough to collect substantial numbers of atoms with high (>several mK) temperature.

a two-level atom with states $|1\rangle$ and $|2\rangle$ driven by an optical field is given (in the interaction representation) by

$$\dot{c}_1(\rho,t) = -\frac{i}{2}\Omega^*(\rho,t)e^{i\delta t}c_2(\rho,t) \tag{3.1}$$

$$\dot{c}_2(\rho,t) = -\frac{i}{2}\Omega(\rho,t)e^{-i\delta t}c_1(\rho,t) \tag{3.2}$$

where $\delta = \omega_{\rm L} - \omega_{\rm o}$ is the atom-field detuning, ρ is the radial coordinate describing the position of an atom within the beam, and $\Omega(\rho,t)$ is the transition Rabi frequency. If the laser field is turned on slowly compared with δ^{-1} (a good approximation if δ is large), we can adiabatically eliminate the excited state and

$$c_2(\rho,t) = -\frac{i}{2}\int_{-\infty}^{t}\Omega^*(\rho,t')e^{-i\delta t'}c_1(\rho,t')\,dt' \approx \frac{\Omega(\rho,t)e^{i\delta t}}{2\delta}c_1(\rho,t) \quad . \tag{3.3}$$

Thus, Eq. 3.1 becomes

$$i\dot{c}_1(\rho,t) \approx \frac{|\Omega(\rho,t)|^2}{2\delta}c_1(\rho,t) \quad . \tag{3.4}$$

Since the laser intensity is proportional to $|\Omega(\rho,t)|^2$, we see that the energy of state 1 is shifted by an amount proportional to the intensity of the applied light field divided by its detuning from the atomic resonance[2].

Equation 3.4 allows for a simple interpretation of the trapping potential of an optical dipole trap, since the energy level shift of the ground state is negative for $\delta < 0$ (or red-detuned trapping light) and proportional to the intensity of the applied light field. If the laser field is uniform in space, the energy of levels $|1\rangle$ and $|2\rangle$ are shifted by a constant amount, as illustrated in Fig. 3.3b. If, however, the applied light field has a spatially varying intensity profile, the energy levels will be shifted by an amount which is proportional to that varying intensity. In particular, if a Gaussian beam is focused through an ensemble of cold atoms, the ground-state energy level

[2]From Eqs. 3.1 and 3.2 it is apparent that the energy shift of state 2 is the same as for state 1 with the replacement $\delta \to -\delta$. Therefore, the energy shift of state 2 is equal and opposite the energy shift of state 1.

shifts of the atoms will follow the Gaussian intensity profile of the beam. The energy of each atom will be minimized in the spatial location that has the highest light intensity. Therefore, a Gaussian-shaped potential well is formed for the atoms, as seen in Fig. 3.3c. This well can be tightly confining (oscillation frequencies of tens of kHz) but is usually shallow (trap depths of $\sim$ mK).

Additional insight may be gained by adopting a more sophisticated treatment of the problem where one solves the density matrix equations of a two-level atom in the presence of a focused light field of arbitrary frequency and intensity. Following the treatment of Ref. [84], one finds that the force, $\mathbf{f}$, on an atom due to the applied light field has two terms: a dissipative term, $\mathbf{f}_{\text{diss}}$, and a gradient term, $\mathbf{f}_{\text{grad}}$. The dissipative term gives rise to radiation pressure forces due to light scattering (which is exploited in a MOT) and the gradient term gives rise to conservative forces due to the interaction of atomic dipole moments with the inhomogeneous laser field (similar to the principle behind a Stern-Gerlach apparatus). It can be shown that $\mathbf{f}_{\text{diss}} \propto |\Omega(\rho,t)|^2/\delta^2$ and $\mathbf{f}_{\text{grad}} \propto |\Omega(\rho,t)|^2/\delta$. Therefore, for large atom-field detunings, δ, (such as used for an optical dipole trap) the gradient term dominates and there is little photon scattering and concomitant heating.

In our system, we realize an optical dipole trap by focusing a $\sim$ 5 W, 1064 nm laser beam through our LVIS-loaded secondary MOT to achieve cigar-shaped atom distributions with full-width at half-maximum (FWHM) diameters of 16 μm $\times$ 16 μm $\times$ 150 μm. The beam is highly red-detuned from the 780.23 nm, $5S_{1/2} \rightarrow 5P_{3/2}$ D2 transition in Rb and it produces a trap with depth $\sim$ 1 mK. There is some heating involved in the transfer of atoms into our dipole trap, so their temperature after loading is also $\sim$ 1 mK. Typical traps have densities of $4 - 5 \times 10^{11}$ cm^{-3} and atom numbers of $\sim 3 \times 10^4$. Images of typical dipole traps are shown in Fig. 3.6.

3.2 Experimental procedure

Once ^{85}Rb atoms are cooled and trapped in either a MOT or an optical dipole trap they can be excited to Rydberg states in different ways. One could turn off the atom trapping light at the time of excitation and excite directly from the $5S_{1/2}$ ground state to nP Rydberg states via a one photon UV transition (transition wavelength ≈ 297 nm) [23]. Alternatively, one may employ a two-photon transition to the Rydberg state. A particularly convenient two-photon transition of Rb into nS or nD Rydberg states is

$$5S_{1/2} \rightarrow 5P_{3/2} \rightarrow nS, nD \tag{3.5}$$

because both the lower and upper transitions have near-IR or visible wavelengths (780.23 nm and $\approx$ 480 nm, respectively) and the oscillator strengths of the two transitions are considerably higher than those of the $5S_{1/2} \rightarrow nP$ transitions (for $n \gtrsim 10$). The respective photoionization cross-sections, which represent a measure for the excitation probabilities one can obtain for equal photon fluences and laser linewidths, are $\sigma_{\mathrm{PI}} = 1.7 \times 10^{-20}$ cm^{-2} for Rb $5S_{1/2}$ [85] and 1.5×10^{-17} cm^{-2} for Rb $5P_{3/2}$ [86]. In all experiments discussed below the two-photon excitation method, shown schematically in Fig. 3.4, is utilized.

The experiments described in the following chapters proceed in very similar ways. Therefore, in the remainder of this section I give a brief outline of the general experimental procedure and then focus on the details of its implementation in the remainder of the chapter. A schematic illustration of the essential components of our experimental apparatus is shown in Fig. 3.5a and an experimental timing diagram is shown in Fig. 3.5b. Each experimental cycle atoms from the LVIS are pushed in the $+x$ direction (as defined in Fig. 3.5a) and are collected in a secondary

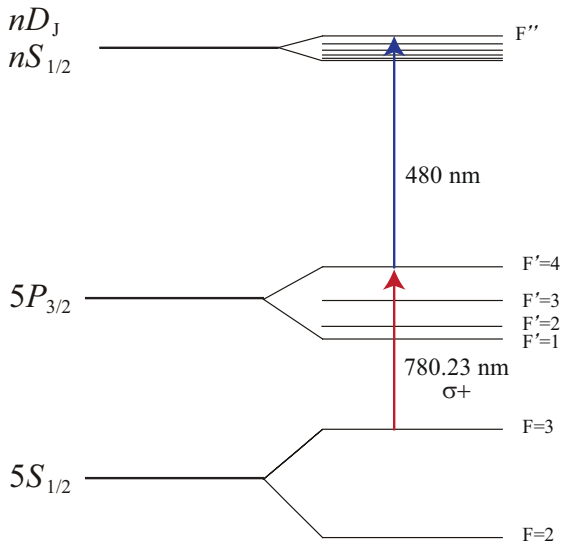

Figure 3.4: Atomic energy level structure of ^{85}Rb relevant to the two-step excitation from the $5S_{1/2}$ ground state to nD or nS Rydberg states.

MOT located between two cylindrically shaped electrodes. Small voltages may be applied to each electrode to excite atoms in the presence of some electric field or large voltages may be applied in order to ionize Rydberg atoms (see Sect. 3.4). In some experiments atoms are excited to Rydberg states directly from the secondary MOT, while in others atoms are collected in an optical dipole trap before excitation. In the former case, the first signal in Fig. 3.5b is not present and the MOT trapping light is turned off $\tau_1 + \tau_2 = 10$ μs before the application of optical excitation pulses. In the latter case, the dipole trap is loaded by overlapping the MOT and dipole trapping beams for 30 ms in time, then turning off the secondary MOT trapping light and allowing atoms not trapped in the focus of the dipole trap beam $\tau_1 = 38$ ms to fall away. We then turn off the dipole trapping light before excitation to eliminate the effects of AC Stark shifts on the Rydberg transition. The atoms are allowed a time $\tau_2 = 1$ to 150 μs to freely expand before the application of the optical pumping and Rydberg excitation pulses.[3] Since the atoms expand isotropically in the transverse

[3]The true values of τ_2 may be up to 2 μs longer than the values quoted here. This is because there is a low intensity tail on the falling edge of the dipole trap light pulse and it is difficult to determine exactly when all the

direction, this allows us to controllably vary the density of the atoms at the time of Rydberg excitation. In general the density profiles will be Gaussian along the three axes in Fig. 3.5a; however, for long τ_2 and spatially narrow excitation lasers, the atomic distribution will be nonuniform in the excitation volume only along the axis of the excitation beams. Absorption images our optical dipole trap for various expansion times, τ_2, are shown in Fig. 3.6.

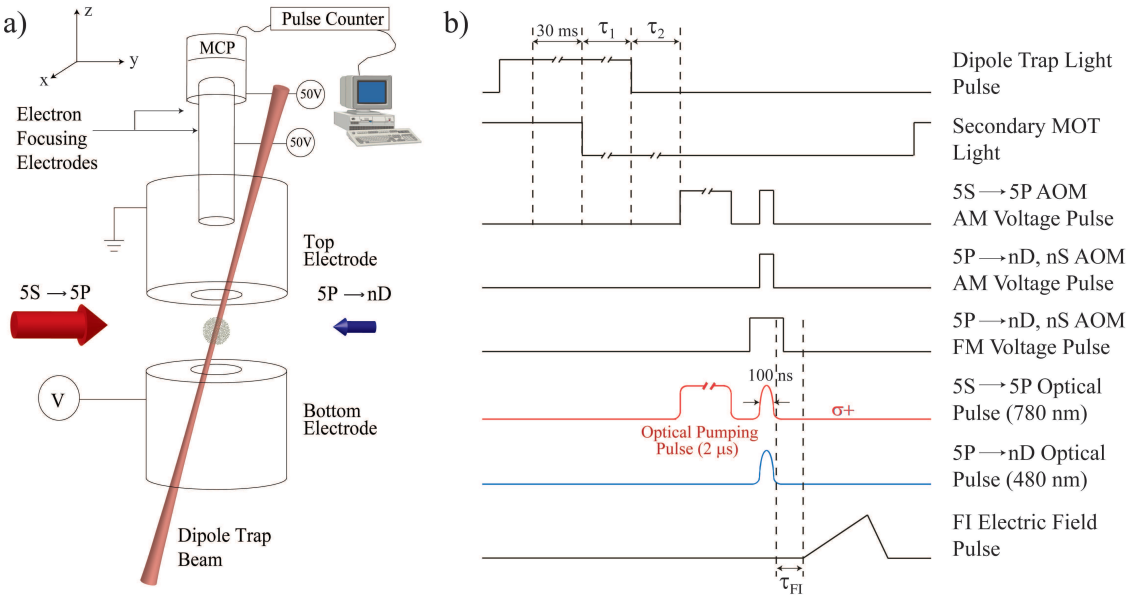

Figure 3.5: a) Schematic illustration of the essential details of our experimental apparatus. b) Timing diagram of the relevant events comprising one experimental cycle of atom trapping, Rydberg excitation, and detection.

Optical excitation proceeds in two steps. First, we apply a resonant (780.23 nm), $\sigma+$-polarized laser pulse of 2 μs duration to the atom cloud, coupling the $5S_{1/2}$ ground state to the $5P_{3/2}$ state. This pulse optically pumps the atoms into the $|F = 3, m_F = 3\rangle$ substate of the $5S_{1/2}$ ground state. After a delay of 300 ns, we perform the two-step excitation to Rydberg states using coincident laser pulses which each have an intensity FWHM of $\sim$ 100 ns. The lower step in the transition is achieved by applying a 780.23 nm, $\sigma+$-polarized laser pulse to populate the $5P_{3/2}$,

light is extinguished. The uncertainty in τ_2 is insignificant compared to other sources of uncertainty in determining dipole trap densities and widths.

$|F' = 4, m'_F = 4\rangle$ state. We ensure that the $5S_{1/2} \rightarrow 5P_{3/2}$ laser is exactly on resonance and determine its Rabi frequency (typically 3.5 MHz) using Autler-Townes spectroscopy [87]. The second step in the transition is driven with a laser pulse with variable polarization that travels in the direction opposite the lower-transition pulse and is resonant with the $5P_{3/2}$, $|F' = 4, m'_F = 4\rangle$ to nD or nS transitions (480 nm). During the 100 ns Rydberg excitation, the atoms move a few tens of nanometers, which is two orders of magnitude less than the average inter-atomic separation.

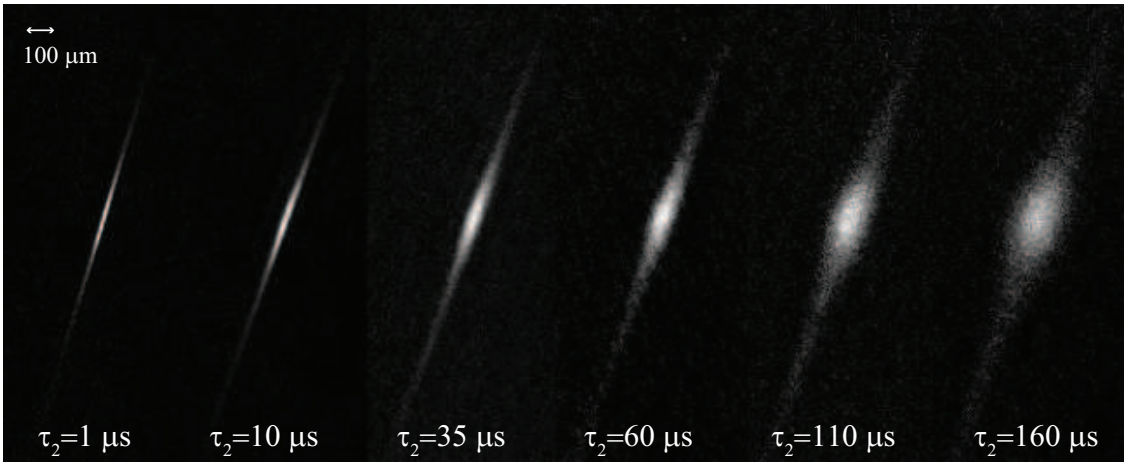

Figure 3.6: Absorption images of an optical dipole trap for different values of the expansion time, τ_2.

The spatial profiles of the two excitation pulses are illustrated in Fig. 3.7 for excitation in both a MOT and a dipole trap. The $5S \rightarrow 5P$ light is collimated to an intensity FWHM diameter of ~ 3 mm, or much larger than any dimension of the atom clouds. Therefore, near the symmetry axis of the beam, the Rabi frequency ($\propto$ the square root of the light intensity) is relatively constant in space. The upper transition has much smaller oscillator strength than the lower transition. Therefore it is necessary to focus the $5P \rightarrow nD/nS$ light to an intensity FWHM of ~ 15 μm to achieve Rabi frequencies comparable to those on the lower transition. This has the unwanted side effect that the upper transition Rabi frequency varies in space in the

transverse directions (due to the Gaussian spatial profile of the beam). We estimate the Rabi frequency on the upper transition to be about 3 MHz. The Rayleigh length of the upper transition beam is $\gtrsim 1$ mm, longer than any dimension of the trapped atom clouds.

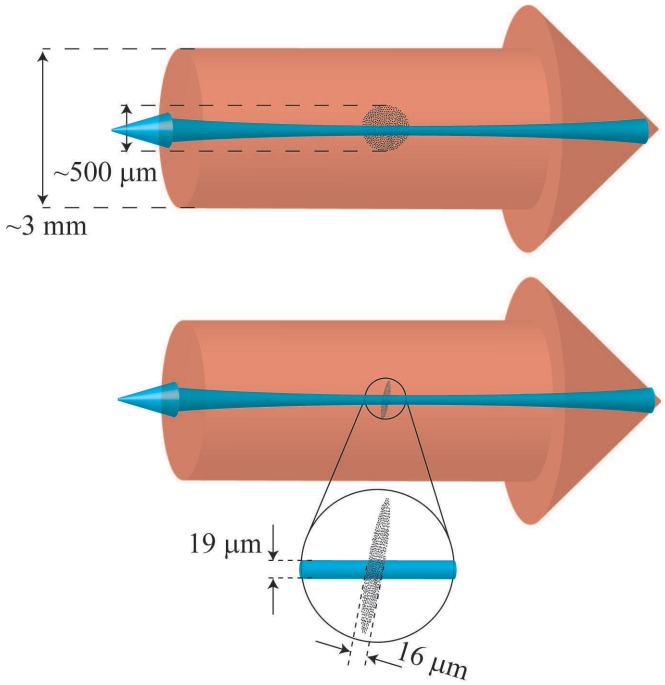

Figure 3.7: Spatial profile of the lower-transition ($5S_{1/2} \rightarrow 5P_{3/2}$) and upper-transition ($5P_{3/2} \rightarrow nD$, nS) Rydberg excitation lasers for excitation in a MOT (upper figure) and an optical dipole trap (lower figure).

After the ensemble has been excited into Rydberg states, it is given a time τ_{FI} to evolve before the number of Rydberg excitations and their Rydberg state distribution are detected. Details on Rydberg state detection are given in Sect. 3.4 below.

3.3 Details of Rydberg excitation

3.3.1 Laser pulses

The experiments described in Chapters IV and V are related to a blockade of Rydberg excitation, where it is necessary to achieve narrowband population transfer into Rydberg states (laser bandwidth $\delta\nu_{\mathrm{L}} \lesssim \Delta W$, where ΔW is the interaction-induced level shift of the state $|N, 2\rangle$). Therefore, the lower and upper transitions are driven using light from narrow-band (~ 2 MHz linewidth) continuous-wave (cw) lasers.

The lower transition light is derived from a cw external cavity diode laser that we constructed. The laser is frequency stabilized to an atomic absorption line using saturated absorption spectroscopy [88, 89]. We use active electrical feedback on both the laser diffraction grating position and diode current to maximize the laser's frequency stability. Pulses are created by passing the light through an amplitude-modulated (AM) acousto-optic modulator (AOM), and the pulses are then coupled into an optical fiber. The upper transition light is derived from a commercial external cavity diode laser with 960 nm wavelength that is frequency doubled to $\lambda = 480$ nm (Toptica DL100 with SHG). The upper-transition pulse is also created by modulating an AOM and coupling the modulated light into an optical fiber. However, unlike for the lower transition, we find that amplitude-modulation (AM) alone is not enough to extinguish unwanted light at the output of the fiber when the pulse is not supposed to be active. Using only AM, a small amount of 480 nm light ($\sim 10^{-4}$ of the incident light) may exit the fiber when the pulse is supposed to be off and this light is incident on the atomic ensemble at all times. Since, for much of one experimental cycle the MOT trapping beams (which drive the $5S_{1/2} \rightarrow 5P_{3/2}$ transition) are active, this unwanted 480 nm "leakage" light may interact with the MOT trapping light and create unwanted Rydberg excitations via the process in Eq. 3.5. Therefore, we also

frequency-modulate (FM) the AOM for a time longer than the amplitude modulation. The combined effect of the FM and AM pulses sweeps light away from the fiber input (due to the FM) while simultaneously reducing its amplitude (due to the AM) when the optical pulse is supposed to be inactive. The combination of AM and FM modulation improves the extinction ratio (when the pulse is off) at the fiber output to $\sim 10^{-6}$. All other laser pulses in our experiment are also derived by passing a cw laser beam through an AOM which is either amplitude- or frequency-modulated.

3.3.2 Rydberg excitation spectra

In all experiments we perform, it is necessary to measure experimentally an excitation spectrum of the Rydberg state that is being studied. An example is shown in Fig. 3.8: a spectrum for the 43D fine-structure doublet. To obtain a spectrum, the frequency of the lower-transition laser is held constant and the frequency of the $5P \rightarrow nD/nS$ laser is scanned in 1.6 MHz steps. The number of Rydberg excitations produced is measured for each frequency (see Sect. 3.4) and the results are displayed in plots such as Fig. 3.8. The upper-transition laser is scanned by locking it to a transmission peak of a scanning, pressure-tuned Fabry-Perot interferometer with a free spectral range of 500 MHz and finesse of $\sim$ 40. [90]. The frequencies of the interferometer's transmission lines are changed by changing the optical path length of the cavity. A stepper motor turns and moves a bellow, changing the pressure of the air in the cavity, and hence its index of refraction. Changing the index of refraction inside the cavity is equivalent to changing the cavity's optical path length. To precisely stabilize the laser frequency to a Fabry-Perot peak, we feed back on both the laser's diffraction grating position and diode current.

In Fig. 3.8, the FWHM of the Rydberg resonances is about 16 MHz. The natural linewidth of the Rydberg resonances near $n = 43$ is of order $\sim$ kHz and the linewidth

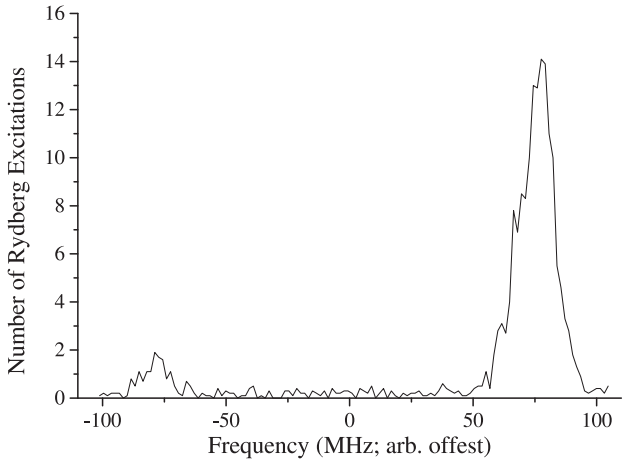

Figure 3.8: Experimental frequency spectrum of the 43D fine-structure doublet in ^{85}Rb.

of the Rydberg transition laser is $\sim$ 2 MHz. Therefore the line broadening evident in Fig. 3.8 must be primarily due to environmental fields (small stray electric fields and the inhomogeneous MOT magnetic field) or static Rydberg-Rydberg interactions (similar to pressure broadening).

Spectra such as the one displayed in Fig. 3.8 form the starting point for all of the experiments described below, as the spectra allow the precise frequency of a desired Rydberg transition to be determined in units of step numbers of the Fabry-Perot's stepper motor.

3.4 Rydberg atom detection

Since the photoabsorption cross-sections of atoms for transitions into Rydberg states are very small, in most spectroscopic studies of Rydberg atoms detection methods are employed in which the Rydberg atoms themselves are detected. Rydberg atoms may be detected directly in one of two ways. First, one may use photomultiplier tubes to observe the fluorescence emitted by Rydberg atoms as they radiatively decay to low-energy states. A second method uses the fact that the valence electron in a Rydberg atom is in a highly-excited state characterized (classically) by a large,

weakly bound orbit. As a result, Rydberg atoms ionize easily due to either collisional ionization or the application of a modest electric field (tens to hundreds of V/cm). After ionization, the free electrons and/or ions can be detected [3, 4].

In the experiments described in this thesis, we employ state selective (electric) field ionization (SSFI) to detect Rydberg atoms, a technique that allows one to not only detect and count all atoms in Rydberg states but also to obtain some information about the distribution of Rydberg states. The latter aspect is especially important in experiments in which the state distribution of Rydberg atoms changes due to collisions, such as those described in Chapter VI. SSFI involves the application of a time-varying electric field pulse to a sample of Rydberg atoms and identification of Rydberg states by the electric field at which they ionize.

Classically, a low angular momentum Rydberg atom in a static electric field, E, (along the z axis) will ionize when the saddle-point of the combined Coulomb-Stark potential

$$V = -1/r + Ez \tag{3.6}$$

has the same energy as the binding energy of that Rydberg state. This is illustrated schematically in Fig. 3.9. The assumption of saddle-point ionization leads to ionization electric fields for low-angular momentum Rydberg states of

$$E_{\mathrm{I,low}\ell} = \frac{1}{16n^{*4}} \quad , \tag{3.7}$$

where $n^* = n - \delta_\ell$ is the effective principal quantum number [3]. Each experimental cycle, we typically apply an electric-field ramp with a rise-time of about 2 μs, and detect the electrons liberated from the loosely-bound Rydberg atoms as a function of time[4]. We average ~ 1000 such events and peaks in the resulting signal (referred to as an SSFI spectrum) are usually identified with bound Rydberg states. The

[4]When we excite to states with $n \geq 54$, we use slower ramps with rise times ~ 100 μs.

identification of a peak at a given electric field with a possible Rydberg state is done using Eq. 3.7. Examples of SSFI spectra labeled with the corresponding quantum states are given in Chapters VI, V, and IV.

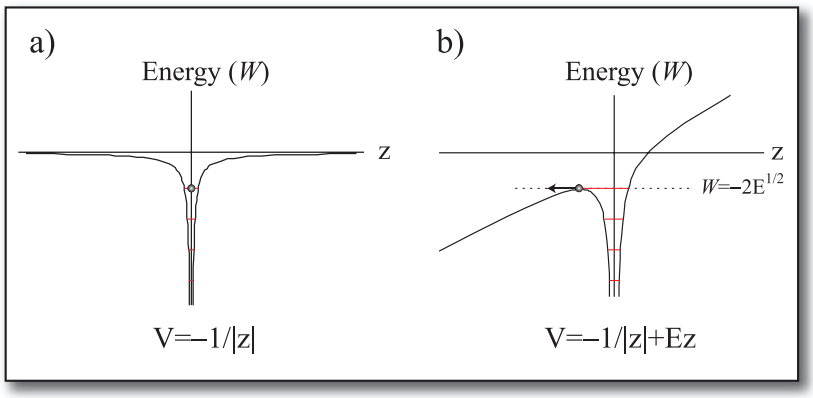

Figure 3.9: a) The $-1/r$ Coulomb potential of an atom in zero electric field. The energies of the bound states of the system are shown in red. b) The combined Coulomb-Stark potential of a Rydberg electron in the presence of an external electric field **E**. When E reaches a value where the energy of the saddle point in the combined potential, $-2E^{1/2}$, equals the energy of a bound Rydberg state, field ionization occurs.

This simple interpretation of SSFI spectra, however, neglects ambiguities in the assignment of Rydberg states that result from the time dependence of the ionization process and from the mapping of the multi-dimensional Rydberg atom state space onto the single dimension space of the electric field. In pulsed field ionization, the ionization field for a given Rydberg state will, in general, depend on the rise time of the electric field pulse. Due to the non-zero quantum defects, δ_ℓ, of non-hydrogenic atoms, the energy levels belonging to adjacent n-manifolds exhibit avoided crossings when plotted versus the electric field in a Stark map (see Fig. 3.10a) [3, 4]. During the field ionization pulse, atoms starting in a given initial state traverse the Stark map and ionize, producing a signal when they reach the ionization threshold of the Stark energy level on which they are traveling. While traversing the Stark map the atoms encounter anti-crossings with other Stark levels. Depending on the separation of the anti-crossings in the Stark map and on the rise time (or slew rate, $S = dE/dt$)

of the electric-field ramp, the atoms may pass through these anti-crossings adiabatically (remaining in the same energy level) or diabatically (jumping energy levels), resulting in different ionization electric fields. For a given initial state, diabatic passage typically results in higher ionization electric fields and broader peaks in the SSFI spectrum than adiabatic passage. If the slew rate is sufficiently low and the separation of the anti-crossings in the Stark map sufficiently large for the passage to be adiabatic, the ionization electric field is given by the classical ionization threshold in Eq. 3.7. This SSFI behavior is usually found for atoms that are initially in a low-angular-momentum (low-ℓ) state with a large (of order 1) quantum defect. In this case, illustrated by the green line in Fig. 3.10b for $43D$ states, atoms follow the classical SSFI behavior and the relationship between E and n^* is well-defined. However, there still can be some ambiguity in the assignment of a given quantum state to a peak in an SSFI spectrum because states of different n may have similar n^*. For example, nS states ($\delta_{\rm S} = 3.13$) and $(n-2)D$ states ($\delta_{\rm D} = 1.34$) ionize at similar electric fields because the respective values of $n^* = n - \delta_\ell$ are similar.

High-angular-momentum Rydberg states with large $|m|$ have Stark maps with very narrow anti-crossings, leading to diabatic field ionization behavior. For a given n, the ionization electric fields of high-$|m|$ states are in the range

$$E_{\rm I,high\ell} = \frac{1}{4n^{*4}} \rightarrow \frac{1}{9n^{*4}} \quad , \tag{3.8}$$

depending on the exact parabolic quantum numbers of the state. Blue-shifted levels tend to ionize at higher and red-shifted levels at lower electric fields[5] [3]. As a result, for high-$|m|$ states, SSFI does not allow for an unambiguous determination of n^*. Much more detail on electric field ionization of Rydberg atoms can be found in Ref. [3] and references therein. In the experiments described in this thesis we

[5]Note that since the ionization thresholds for blue- and red-shifted high-ℓ states are different than for low-ℓ states, they are not given by the red curve in Fig. 3.10b.

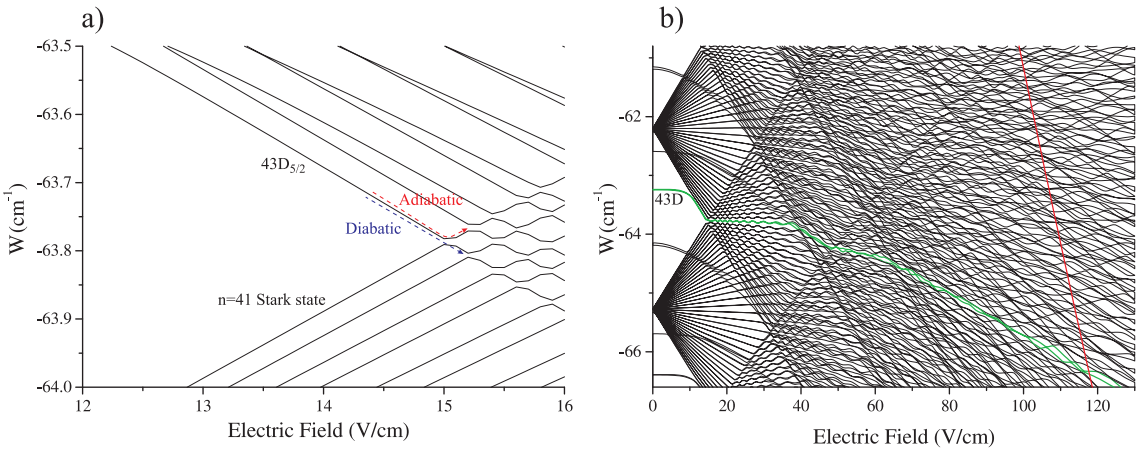

Figure 3.10: a) Stark map for $|m| = 5/2$ states in the vicinity the first anticrossing between the $43D_{5/2}$ state and the $n = 41$ hydrogenic manifold. The adiabatic (diabatic) path through the anticrossing is shown in red (blue). b) Stark map for $|m| = 1/2$ states in the vicinity of the $n = 41$ and 42 hydrogenic manifolds (with a larger displayed electric field range than in a). The low-ℓ classical ionization limit is displayed in red, illustrating the difference in ionization field for adiabatic and diabatic passage through the avoided level crossings. The adiabatic path to ionization taken by the $43D$ state through the Stark map is shown in green.

use mostly SSFI electric-field ramps that are slow enough that atoms in low-ℓ states ionize adiabatically, allowing for a well-defined assignment of n^*-values to peaks in SSFI measurements. We do, however, see evidence of diabatic passage in the SSFI of very high-lying low-ℓ states ($n \gtrsim 70$) and of high-$|m|$ states produced in collisions.

3.4.1 Experimental details of the SSFI method

In the following, I discuss a few experimental details of the SSFI method. The SSFI electric field pulse is applied to the sample by applying a negative voltage pulse to the lower cylindrical electrode pictured in Fig. 3.5a. The SSFI electric-field pulse ionizes Rydberg atoms and accelerates the liberated electrons toward a detector. In the space between the atom-trapping region and the detector we use electron focusing electrodes with circular cross sections, held at potentials of 50 V relative to the SSFI location, in order to control the electron trajectories and to increase the electron collection efficiency. The electrons then impinge on a microchannel plate detector (MCP). An MCP is a periodic array of fused thin lead glass capillaries (or channels)

sliced into a thin plate [91]. A single incident electron enters a channel, hits a channel wall, and releases secondary electrons. The latter are accelerated by voltages ~ 1000 V applied across the MCP, and produce more secondary electrons. We use a two-stage MCP with a gain in the range of 10^8. Our MCP is used in conjunction with a phosphor screen mounted behind the MCP rear face. The phosphor screen emits a localized fluorescent light burst when impacted by an electron shower and gives some information about the spatial distribution of the counts on the surface of the MCP. If the electron transfer function between the SSFI region and the MCP is sufficiently well defined, one can use the spatial image acquired on the phosphor screen to infer the spatial distribution of Rydberg atoms at the time of ionization. This capability is not currently exploited but experiments are planned which utilize this capability (see Sect. 7.2.1).

Electric pulses corresponding to single electron impacts are capacitively coupled out of the phosphor screen. In this way, each electron detected by the MCP/phosphor screen creates a voltage pulse of the order of 10 mV in height and 5 nanoseconds in duration. Typical detector efficiencies for systems like ours are in the range $0.5 \lesssim \eta \lesssim 0.85$ [91]. The pulses obtained from the MCP are pre-amplified and counted via a single-photon counter. Sequences of MCP pulses are simultaneously averaged and displayed as a function of time on an oscilloscope, along with the field-ionization voltage ramp, in order to produce SSFI spectra and infer the distribution of states.

CHAPTER IV

Measuring excitation blockades using counting statistics

In Chapter I we noted that strong interactions among Rydberg atoms may lead to a "blockade," or suppression, of Rydberg excitation. Several groups have demonstrated evidence of an excitation blockade based on always-present van der Waals interactions or electric field-induced dipole-dipole interactions. However, to our knowledge all experimental work on excitation blockades save that of our group [11, 71] has relied on the same technique to demonstrate the blockade; namely, a saturation of Rydberg excitation with some experimentally varied parameter [23–26]. In these experiments, hundreds to several thousands of Rydberg excitations are created.

In this chapter, I present a different approach to demonstrating the effectiveness of an excitation blockade. We examine the statistical distributions of the number of Rydberg excitations created each experimental cycle and show that the distributions become narrower when a blockade is effective. In particular, we show that sub-Poissonian distributions of the number of Rydberg excitations may be measured when sources of experimental noise are minimized. Our measurements were performed on systems with tens of Rydberg excitations, about two orders of magnitude fewer excitations than in other systems. In fact, our technique is ideally suited for measuring the effectiveness of an excitation blockade in systems with as few as one

or two Rydberg excitations, systems which may be useful in the implementation of neutral-atom quantum information processing schemes.

4.1 Measuring an excitation blockade

Rydberg excitation blockades are a consequence of the nature of the energy spectrum of the many-atom eigenstates of a system of interacting Rydberg atoms. The k-th excited state of an N-atom system, $|N,k\rangle$, is a state where all k excitations are coherently shared among the N atoms. The energy spectrum of the collective system consists of an non-equidistant ladder of energies (depicted in Fig. 1.1 and the inset of Fig. 4.1) where the states with $k > 1$ have an energy spacing $W_{\rm k} - W_{\rm k-1}$ different from $W_1 - W_0 = W_{\rm Ryd}$ because static Rydberg-Rydberg interactions perturb the interaction-free system. Therefore, if the system is excited on the first step of the ladder, and the interactions produce level shifts for $k > 1$ larger than $\delta\nu_{\rm L}$, where $\delta\nu_{\rm L}$ is the laser linewidth, then all excitations with $k > 1$ are shifted out of resonance with the exciting laser, or "blockaded." It is then only possible to create one Rydberg excitation in the system, regardless of the number of ground-state atoms or the intensity of the exciting laser.

If atoms are excited to Rydberg states within an extended atomic ensemble, one expects to obtain not one excitation, but multiple regions inside of which one collective excitation occurs, as shown schematically in Fig. 4.1. Inside of each region, an entangled state is created whose energy spectrum is identical to the spectrum sketched in Fig. 1.1. This breaking up of the excitation volume into "bubbles" is a consequence of the finite range of Rydberg-Rydberg interactions.[1] Far enough from a singly-excited entangled superposition of atoms, the atom-atom interaction strength

[1] The bubbles are not real, they are a convenient heuristic construction that reflects the following fact. If we perform a quantum measurement where we project all many-body entangled states $|N,1\rangle$ in different regions of the excitation volume onto individual atoms and measure the positions of these Rydberg atoms, the pair correlation function will be zero for some volume around each detected atom.

decreases by enough that another singly-excited state may be created. The radius of these bubbles, R_b, is determined by assuming that $2R_\mathrm{b}$ is the distance at which the interaction-induced shift, ΔW, equals the laser linewidth, $\delta\nu_\mathrm{L}$. This picture of the Rydberg excitation blockade in an extended atomic ensemble naturally suggests two methods for measuring the effect of a blockade. These two methods will be described in Sections 4.1.1 and 4.1.2.

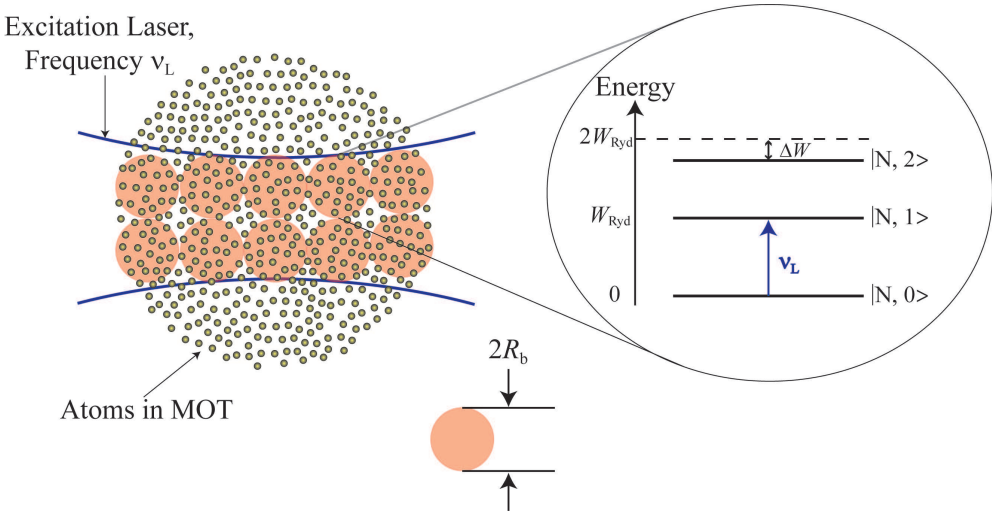

Figure 4.1: Illustration of an ensemble of atoms in a MOT with a Rydberg excitation blockade of range R_b. The excitation volume is defined by overlap of the excitation laser (blue lines) and the atom cloud. Each bubble in the excitation volume represents a region inside of which there is, ideally, one Rydberg excitation. The energy spectrum of the collective quantum state of atoms in each bubble is shown in the inset.

4.1.1 Saturation of excitation number

The most straightforward method for observing the effect of an excitation blockade is to count the number of Rydberg excitations detected as a function of some parameter that increases the strength of the Rydberg-Rydberg interactions. For example, one may compare the number of Rydberg excitations detected when exciting to a low n state, where van der Waals interactions are weak, to the number detected when exciting to a high n state, where van der Waals interactions are strong. Since the bubble radius grows as the interactions become stronger, fewer bubbles may

fit in a given excitation volume for strong interactions than for weak interactions. Thus, if identical atomic ensembles are excited into different Rydberg states with equal Rabi frequencies, the blockade will manifest itself as a reduction of the number of excitations detected for excitation to high n states compared with excitation to low n states. Identical considerations apply if the interactions are enhanced via the application of an external electric field to realize a dipole blockade. To enhance Rydberg-Rydberg interactions, a Förster-resonant electric field may be applied to tune an interaction channel into exact resonance (see Eq. 2.7) or a larger field may be applied to induce permanent dipole moments in the Rydberg atoms (see Eq. 2.6). In either of these cases, the dipole blockade is manifested as a suppression of the number of excitations created when the field is applied relative to the number created when the field is absent [24–26].

4.1.2 Counting statistics

We have developed a different method to quantify the effect of an excitation blockade. This method, which is based on the counting statistics of the number of Rydberg excitations created, may be understood as follows. We assume that there is a negligible probability to excite in each bubble a state $|N, k\rangle$ with $k > 1$ and that the probability to excite $|N, 1\rangle$ is high. Therefore, the total number of Rydberg excitations produced for each realization of the excitation process approximately equals the number of bubbles which fit into the excitation volume (see Fig. 4.1). Since the excitation volume is fixed, this number is not expected to fluctuate considerably. In the limit that the $|N, 1\rangle$ state is created in every bubble the same number of excitations would be created every time atoms are excited. In realistic systems, however, we don't expect to create exactly the same number of excitations for each experimental cycle and we expect some width to the distribution of the number

of detected excitations. For identically prepared systems, the distributions will be narrower when the interactions are strong and the blockade is effective than when the interactions are weak and excitation is random. Our method for observing the effect of an excitation blockade involves varying some parameter (n or an applied electric field) that changes the Rydberg-Rydberg interaction strength and measuring the width of the excitation number distributions. The narrower the distribution, the more effective the excitation blockade.

To quantitatively characterize the width of the Rydberg excitation distributions, we use the Mandel Q-parameter, defined by the variance in the number of excitations divided by the mean minus 1,

$$Q = \frac{< N_{\rm e}^2 > - < N_{\rm e} >^2}{< N_{\rm e} >} - 1 \quad . \tag{4.1}$$

Values of $Q > 0$ correspond to super-Poissonian (wider than Poissonian) distributions, $Q = 0$ to Poissonian distributions, and $Q < 0$ to sub-Poissonian (narrower than Poissonian) distributions [92]. We expect that as we vary a parameter that changes the interactions from weak to strong, the counting statistics will change from Poissonian (which is expected for random excitation) to sub-Poissonian (which is expected for correlated numbers of excitations). Theoretical calculations support our conjecture that sub-Poissonian distributions should be observed in the limit of strong interactions [28, 29]. We expect, however, that experimental noise sources such as laser frequency and intensity instabilities, finite detector efficiency, and spatially inhomogeneous Rabi frequencies will somewhat lessen the sub-Poissonian nature of the detected distributions. How much these sources of noise broaden the distributions is discussed below.

4.1.3 Comparison of the two methods

As noted above, the excitation-saturation method is the most straightforward method to quantify the effect of an excitation blockade. Since this method relies on a decrease in the total number of excitations, N_e, to demonstrate a blockade, it yields the most conclusive results when N_e is large. The counting-statistics method, however, relies on the statistics of the number of excitations created and its effectiveness is independent of the precise value of N_e. As N_e changes, the width of the counting distributions will change but the Q-value ($\propto \sigma/\sqrt{N_e}$) does not. Therefore, our method is particularly well-suited to measure the effect of a blockade in systems with small N_e. In fact, systems with only one or two excitations may show a marked variation in the value of the Mandel-Q parameter as the strength of the interactions is tuned.

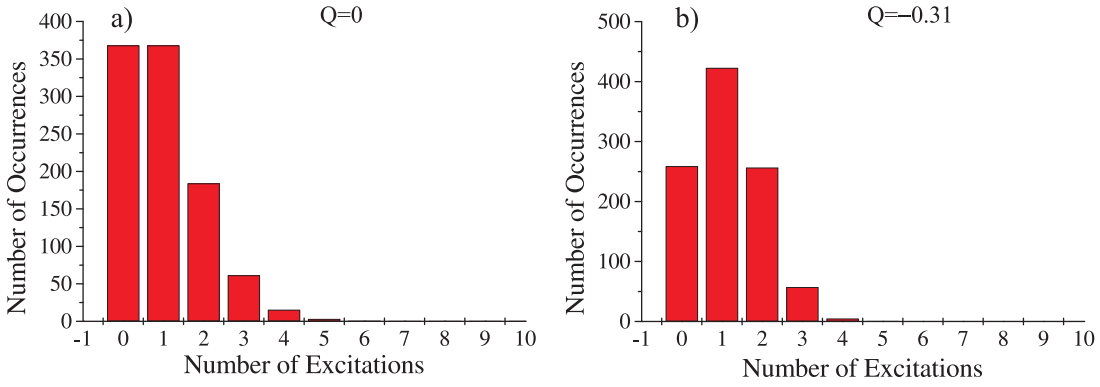

Figure 4.2: Hypothetical Rydberg atom counting distributions which each have a mean number of excitations equal to one. While it would be difficult to distinguish how effective the blockade is in the ensembles that produced these statistics using the excitation saturation method, the counting statistics are clearly distinguishable.

To illustrate this point, I present Fig. 4.2. In Figs. 4.2a and b I show hypothetical atom-counting distributions which each have a mean value of one Rydberg excitation. The distribution in a) has $Q = 0$ (Poissonian) and the distribution in b) has $Q = -0.31$ (significantly sub-Poissonian). Thus, we can clearly distinguish between cases

with a weak blockade (Poissonian statistics) and a strong blockade (sub-Poissonian statistics) when the average number of counts is very small. However, in systems with only one or two Rydberg excitations, the difference in the total number of excitations for weak and strong interactions may not be significant compared with experimental noise.

The ability to measure an excitation blockade in systems with few excitations is important because the first neutral-atom quantum gates will likely be realized in such systems. More generally, however, systems with few excitations are of interest because it is easier to obtain shot-noise-limited measurements in such systems than in systems with many excitations. Technical noise (*i.e.* systematic and random noise due to experimental conditions) and shot noise (*i.e.* statistical noise intrinsic to the measurement process) lead to uncertainty in the number of excitations detected, N_{e}, of μN_{e} and $\sqrt{N_{\mathrm{e}}}$, respectively, where μ is a constant. Therefore the fractional uncertainty in a measurement, *i.e.* the uncertainty as a percentage of the total number of excitations created, is independent of N_{e} (and equal to μ) for technical noise and equals $1/\sqrt{N_{\mathrm{e}}}$ for shot noise. Therefore, measurements in large systems are limited by technical noise while in small systems they are limited only by shot noise. The accuracy of technical noise-limited measurements will be determined by the quality of the experimental apparatus, while shot noise-limited measurements will be as accurate as the statistics of the quantum measurement process allow. To measure the blockade most effectively and obtain shot-noise limited measurements one requires

$$\mu < 1/\sqrt{N_{\mathrm{e}}} \quad . \tag{4.2}$$

This point may be made more clear with the help of a few numerical examples. If $N_{\mathrm{e}} \sim 1000$, as in some of the published work on excitation blockades [23–25], we

must have the relative technical noise $\mu < 3\%$ to in order to be shot-noise limited according to Eq. 4.2. This is a very stringent requirement. Conversely, if we have $N_e = 4$, one requires relative technical noise of only $\mu = 50\%$ to obtain shot-noise-limited measurements, which should be very easy to implement. Finally, if we make the reasonable assumption that the relative noise, μ, in the number of detected Rydberg excitations is about 20%, we need $N_e < 25$ to obtain shot-noise limited measurements.

We have seen evidence for excitation blockades using the excitation-saturation method in systems with few (~ 10) excitations. However, since the counting statistics method is superior for systems with few excitations, I focus on this method in the present chapter. In the next two sections I present experiments that use this method to demonstrate the effect of the van der Waals blockade and dipole blockade, respectively.

4.2 Measuring the effectiveness of the van der Waals blockade using counting statistics

4.2.1 Experimental details

In this experiment, we excite atoms in a MOT to $nD_{5/2}$ Rydberg states using the two-photon excitation scheme described in Sect. 3.2 and the spatial beam geometry shown in the upper panel of Fig. 3.7. There are, however, a few notable departures from the general experimental procedure described in Sect. 3.2. The Rabi frequencies of the lower transition are varied and fall in the range from 3 to 9 MHz. Additionally, in this section we examine Rydberg excitation distributions for $54 \leq n \leq 88$. Because the oscillator strength of the $5P_{3/2} \rightarrow nD_{5/2}$ transition scales with n^* as n^{*-3} [3], many more Rydberg excitations are generated at low n than at high n for a given upper transition laser intensity. Therefore, to avoid detector saturation we adjust the

intensity of the upper transition laser pulse to ensure that ~ 30 Rydberg excitations are detected each time atoms are excited, regardless of n. Given a conservative estimate of the MCP detector efficiency ($\eta \sim 0.5$), this corresponds to the generation of ~ 60 excitations.

Great care was taken to realize a MOT with a smooth spatial profile and little spatial jitter. By imaging the MOT fluorescence directly onto a CCD camera with a 1:10 imaging system, we were able to see fine details of the distribution of ground-state atoms in the MOT. We observed spatial structures on the MOT separated by $\sim$ hundreds of micrometers due to light intensity modulation caused by interference between different trapping beams. We also observed fluctuations in the MOT shape and center of mass position on the order of 10% of the MOT diameter. Since these density and spatial modulations will affect how many ground-state atoms are in each bubble and how the upper transition laser overlaps with the MOT, they will broaden the detected Rydberg atom counting statistics. Therefore, we used irises to limit the diameter of the trapping beams to ~ 5 mm and used a high magnetic field gradient (50 G/cm) to create a MOT with a diameter smaller than the width of one interference fringe. We also adjusted the precise overlap of the trapping beams to minimize jitter in the MOT shape and position. In order to further limit these unwanted effects we disabled the loading of the secondary MOT from the LVIS. These procedures lead to a MOT with a full width of about 300 μm and density of $\sim 5 \times 10^{-9}$ cm^{-3}.

4.2.2 Q-values vs. n

To perform the experiment, we set the frequency of the upper transition laser on resonance with the $|0r\rangle \rightarrow |1r\rangle$ transition and count the number of Rydberg excitations created using field ionization. We typically perform this procedure 1000 times

and calculate the Q-value of the measured distribution of the number of excitations. This was done for $nD_{5/2}$ states in the range $54 \leq n \leq 88$ and the Q-values are displayed as points in Fig. 4.3, referenced to the left axis. The error bars represent the typical spread in measured Q-values for repeated measurements under identical conditions. This figure illustrates the gradual development of the blockade as n is increased and the magnitude of the level shifts, $\Delta W^{(2)}$, as n^{*11}. For $n \lesssim 58$, the detected Q-values are ~ 1, the largest of the displayed values. Thus, for $n \lesssim 58$ the excitation number distributions are wide and the blockade appears to be highly ineffective. In the range $58 \lesssim n \lesssim 77$, the detected Q-value drops from ~ 1 to ~ 0, leveling to ~ 0 for $n \approx 77$. We attribute this narrowing of the counting statistics with n to an excitation blockade in the Rydberg atom excitation process that becomes increasingly important for larger n. Figure 4.3 demonstrates the transition between the uncorrelated domain ($n \lesssim 58$) and the blockade domain ($n \gtrsim 77$).

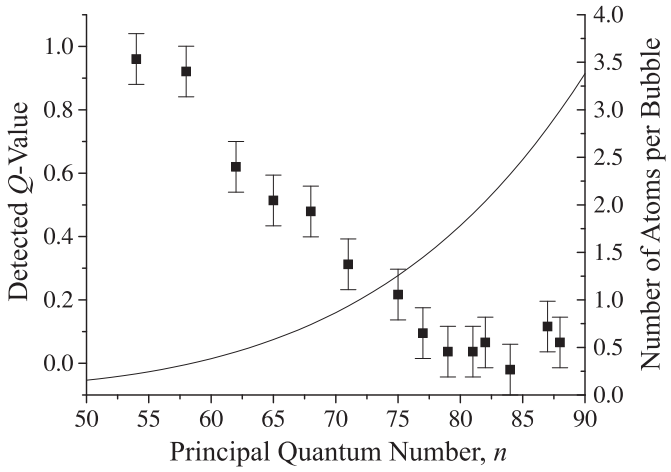

Figure 4.3: The symbols depict Q-values measured as a function of principal quantum number, n, for excitation to $nD_{5/2}$ states in a MOT (left axis). The average number of detected Rydberg atoms was kept constant at about 30. The line shows the calculated number of atoms in each bubble with volume $V_{\rm b}$, determined using the interaction energies of Fig. 2.2 (right axis).

Note that in Fig. 4.3 we do not observe sub-Poissonian statistics at high n, where the blockade is expected to be effective, while at low n we observe super-Poissonian

statistics, or $Q \sim 1$. At low n, technical noise (e.g., super-Poissonian shot-to-shot fluctuations of the ground-state atom number due to MOT jitter, variations in the single-atom excitation efficiency due to a spatially varying upper transition Rabi frequency, and noise in the laser frequency and intensity) causes the statistics to be super-Poissionian ($Q \sim 1$). At large n, the Rydberg excitation number distributions are significantly narrowed by the blockade effect, causing the Q value to decrease from 1 to about 0. In the absence of technical noise, one would expect $Q \sim 0$ at low n and substantially negative at high n [28, 29]. The relative changes in Q are, however, unaffected by technical noise and we conclude that the significant narrowing of the counting statistics is due to the van der Waals blockade.

4.2.3 Comparison with theory

The calculations of the energy level shifts, $\Delta W^{(2)}$, presented in Sect. 2.2.1 may provide additional insight into the experimental data of Fig. 4.3. Two things stand out in particular. First, since this experiment was performed on ensembles of randomly placed atoms in a MOT, the dependence of the energy level shifts of $D_{5/2}$-states on the polar angle θ between two atoms (defined in Fig. 2.1) will manifest itself as an average over the energy shift at all angles. The theoretical results presented in Fig. 2.2b reveal that the scaled level shifts are large in magnitude for all θ, never change sign, and do not vary by more than a factor of two as a function of θ. The insensitivity of the level shifts to experimental variations in θ is consistent with the observation of a significant narrowing of the counting statistics in Fig. 4.3 as n is increased, due to the blockade effect. If the θ-dependence was such the energy shift averaged over all angles was zero, no such narrowing of the statistics would be observed as n is increased.

Second, the results of Sect. 2.2.1 also explain why the Q-values exhibit a smooth

transition from $Q \sim 1$ at low n to $Q \sim 0$ at high n. Any strong resonance of the type apparent in Figs. 2.2 or 2.3 would lead to an enhancement of the energy level shifts and a dip in the Q-value centered at the principal quantum number at which the resonance occurs. The scaled van der Waals level shifts in Fig. 2.2(a) reveal that over the range studied here, $54 \leq n \leq 88$, there is no resonant channel for $nD_{5/2}$ states, and consequently the energy shifts are van der Waals in nature and scale smoothly with n^* as n^{*11}. This translates into a gradual increase of the blockade effectiveness and a monotonic decrease of the Q-value with increasing n.

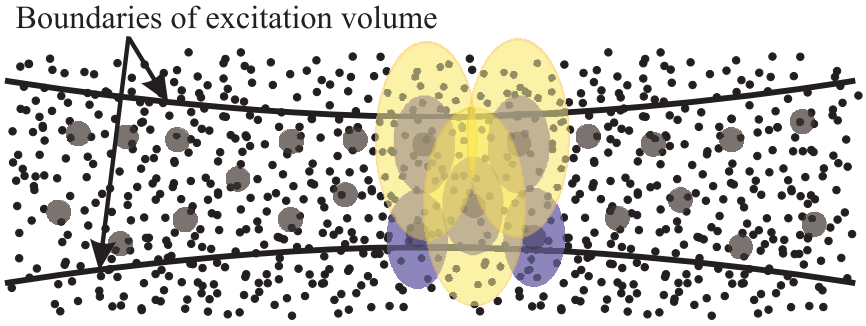

Figure 4.4: Graphical representation of a Rydberg-excitation blockade inside an extended atomic ensemble, illustrating the difference in the single-excitation volume and the bubble volume. Within the boundaries of the excitation volume (lines), Rydberg excitations created in a cloud of ground-state atoms (dots) are localized and detected at certain atoms (dark gray spheres) using a quantum measurement process. Due to the Rydberg blockade, each detected Rydberg atom defines a volume $V_{\rm se}$ (yellow) in which no other Rydberg atoms can be detected. Of order 8 such volumes overlap one another. The non-overlapping region "belonging" to each detected Rydberg atom defines the bubble volume, $V_{\rm b}$. In general, these volumes are not spherical because of the angular dependence of the energy level shift, $\Delta W^{(2)}$.

This smooth scaling is further illustrated by examining how many atoms are in the volume associated with each bubble, $V_{\rm b}$, as a function of n. This is equivalent to examining the volume associated with a single excitation, or $V_{\rm se}$ as a function of n. In Fig. 4.4 we illustrate the difference between the volumes $V_{\rm b}$ (blue) and $V_{\rm se}$ (yellow). The two volumes are related by $V_{\rm b} = 1/8 V_{\rm se}$, where the factor 1/8 is due to the fact that, in a three-dimensional configuration, about eight single excitation

regions may overlap each other.

The single excitation volume, $V_{\rm se}$, can be estimated by

$$V_{\rm se}(n) = 2\pi \int_0^{\pi} \sin\theta \, d\theta \int_0^{R_{\rm se}(n,\theta)} r^2 dr \tag{4.3}$$

where $R_{\rm se}(n,\theta)$ is the radial coordinate of the surface at a given n and polar angle θ at which the energy level shift equals the laser linewidth (2 MHz in the experiment). We determine $R_{\rm se}(n,\theta)$ by solving

$$\Delta W^{(2)}(n, R_{\rm se}, \theta) = 2 \text{ MHz} \tag{4.4}$$

for $R_{\rm se}$, where $\Delta W^{(2)}$ is given in Eq. 2.5 and plotted as a function of n and θ in Fig. 2.2. Due to the variation in the magnitude of $\Delta W^{(2)}$ with the angle θ (defined in Fig. 2.1), the single-excitation volume will, in general, not be spherical, as indicated in Fig. 4.4. To model the experiment, we use $l = 2$, $j = 5/2$, and $m_{\rm j} = 5/2$ in the expression for $\Delta W^{(2)}$. To estimate the number of all atoms $N_{\rm b}$ in $V_{\rm b}$ as a function of n, we multiply the values of $V_{\rm b}(n) = \frac{1}{8} V_{\rm se}(n)$ obtained from Eq. 4.3 by the ground-state atom density (5×10^9 cm^{-3}). The results for $N_{\rm b}$ are shown as the solid line in Fig. 4.3 (referenced to right y-axis).

For $55 \lesssim n \lesssim 70$, where the Rydberg-atom counting distribution has a Q-value in the range $1 \gtrsim Q \gtrsim 0.4$, $N_{\rm b}$ is in the range $0.25 \lesssim N_{\rm b} \lesssim 1$. This value is too low to ensure the creation of one Rydberg excitation in each bubble for our excitation efficiency (which is < 1). The resultant uncertainty in the overall number of Rydberg excitations in the whole atomic sample, together with technical noise, results in the super-Poissonian Rydberg-atom counting distributions observed for this n range. For $n \gtrsim 75$, where the Q-values saturate at about 0, $N_{\rm b}$ varies from approximately 1.5 to 3.5. Given our finite excitation efficiency, these values of $N_{\rm b}$ allow us to come closer to ensuring that one Rydberg excitation is created in each bubble. Therefore,

the counting statistics are significantly narrower than for low n. As N_b increases, the counting statistics become narrower, since it becomes more likely that the state $|N, 1\rangle$ is excited in each bubble. It should be noted that our estimates of N_b depend sensitively on our estimate of the ground-state atom density (5×10^9 cm^{-3}) and the laser linewidth (2 MHz) in the experiment. Since these values represent conservative estimates, we believe that the actual values of N_b may be larger than the ones shown in Fig. 4.3. In particular, since later measurements of MOT densities lead us to believe we may have underestimated the density by a factor of about 2, the values of N_b may be up to twice as large as those shown in Fig. 4.3.[2]

4.3 Measuring the dipole blockade using counting statistics

Thus far I have presented evidence for the always-present van der Waals blockade of Rydberg excitation in a MOT where we detect about 30 excitations. In a followup experiment we sought to reduce the effect of technical noise with the aim of observing significantly sub-Poissonian counting distributions. Additionally, we sought to move towards systems expected to be applicable in the context of quantum information processing (systems with few excitations and controllable interactions). Therefore, I next present an experiment examining distributions of fewer Rydberg excitations to measure the effectiveness of a dipole blockade, or a blockade which is controllably enhanced via the application of an external Förster resonant electric field (see Sections 2.1.3 and 2.3.1).

In this experiment we examine the counting statistics of Rydberg excitations created from atoms in an optical dipole trap. The dipole trap is created using the methods described in Chapter III and the excitation geometry is shown in the lower

[2]We did not have the capability to measure MOT densities using shadow imaging at the time this experiment was performed.

panel of Fig. 3.7. In order to maximize the ground-state atom density, we use a short delay between dipole trap light shutoff and the optical excitation pulses, or $\tau_2 = 1$ μs (in the notation of Fig. 3.5).

There are several advantages to exciting atoms collected in an optical dipole trap compared with a MOT. First, the excitation volume is defined by the overlap of the upper transition beam and a narrow, cigar shaped atom distribution. This results in a smaller excitation volume and fewer Rydberg excitations than we find for excitation in a MOT (of order 10 detected excitations). As mentioned above, if we assume $\mu \approx 20\%$, we need $N_e < 25$ excitations for our measurements to be shot-noise limited. This is not the case in the experiment performed using the MOT (where $N_e \approx 30$) but is achieved using an optical dipole trap. Further, we have found that atom clouds produced using an optical dipole trap have much less spatial jitter and more uniform atom density than the clouds produced in MOTs, resulting in a smaller value of μ. Additionally, the density we achieve in our optical dipole trap ($\sim 5 \times 10^{11}$ cm^{-3}) is a factor of ~ 100 higher than in the MOT described above ($\sim 5 \times 10^{9}$ cm^{-3}), resulting in two orders of magnitude more ground-state atoms per bubble. This means that each Rydberg excitation is collectively shared by more atoms and the likelihood that the $|N, 1\rangle$ state is excited in each bubble is improved. Finally, by choosing a trap narrower (16 μm FWHM) than the upper transition laser beam (19 μm FWHM for this experiment), we lessen the effects of the spatially inhomogeneous upper transition Rabi frequency. This point is best illustrated by examining the excitation geometry for the experiment in the MOT and dipole trap respectively, as shown in Fig. 4.5. In a MOT, there is some excitation in the transverse wings of the upper transition Gaussian beam, where the intensity is lowest and the blockade is not effective. In the dipole trap, where the upper transition

beam is wider than the atom cloud, we have this issue only in one direction (shown in Fig. 4.5 as the z direction) and not the other (x) direction. This further reduces unwanted broadening of the Rydberg excitation number distributions.

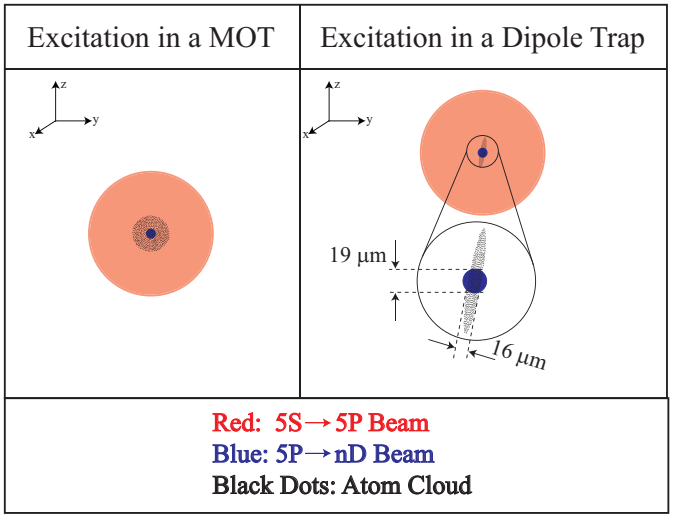

Figure 4.5: Spatial profile of the lower-transition ($5S_{1/2} \rightarrow 5P_{3/2}$) and upper-transition ($5P_{3/2} \rightarrow nD$, nS) Rydberg excitation lasers for excitation in a MOT (left figure) and an optical dipole trap (right figure). This figure is identical to Fig. 3.7 except that we view the two beams along their mutual axis of propagation (the y-axis).

4.3.1 Q-values in applied electric fields

This experiment proceeds in a similar fashion to the experiment described in Sect. 4.2 except that the Rabi frequencies of the lower and upper transitions are fixed at the values given in Chapter III (3.5 and 3 MHz, respectively) and atoms were collected in an optical dipole trap before they are excited to Rydberg states. We examine the Rydberg atom counting distributions for excitation to the $45D_{5/2}$ state in zero applied field and an applied Förster resonant field, E_{F}, to demonstrate the enhancement of the excitation blockade due to larger interaction energies when E_{F} is applied. An electric field is applied to the atom cloud by applying a small voltage to the lower electrode in Fig. 3.5 during excitation.

In order to realize a Förster resonance for $45D_{5/2}$ atoms, we tune the following

channel

$$2 \times 45D_{5/2} \rightarrow 43F + 47P_{3/2} \tag{4.5}$$

into resonance via an applied electric field, as shown in Fig. 2.5. In zero electric field, the infinite separation energy defect is $\Delta = W_{43\mathrm{F}} + W_{47\mathrm{P}} - 2 \times W_{45\mathrm{D}} = 120$ MHz. With the application of a small DC electric field, one may continuously tune this energy defect from 120 MHz to ≈ 0 MHz. In zero applied field, when the energy defect is large compared with the coupling strength of many of pairs of atoms in a bubble, the interactions are primarily van der Waals in nature ($\sim 1/R^6$, where R is the atom-atom separation), and are weaker and shorter-ranged. In the presence of a Förster resonant field, the energy defect is zero and the interactions are primarily dipole-dipole in character ($\sim 1/R^3$) and are stronger and longer-ranged. Thus, we expect larger bubbles in which more atoms collectively share one Rydberg excitation when the Förster resonant field is applied. Therefore, when the Förster resonant field is applied it is more likely that the $|N, 1\rangle$ state is populated in each bubble, the excitation blockade is more effective, and the Rydberg excitation number distributions are narrower.

In order to determine experimentally the Förster resonant electric field, E_{F}, we follow the procedure of Refs. [58, 70]. We vary an applied electric field and examine the state-selective field ionization (SSFI) spectra obtained $\tau_{\mathrm{FI}} = 100$ ns after Rydberg excitation. There should be a distinct maximum in the amplitudes of the signal corresponding to the $43F$ and $47P_{3/2}$ states when the energy detuning of the channel in Eq. 4.5 is zero. This is because the rates for two atoms in $45D_{5/2}$ to undergo long-range energy transfer collisions into $43F$ and $47P_{3/2}$ states via this channel are strongly enhanced when the detuning of the channel is zero (see Chapter VI). In Fig. 4.6a I show a series of SSFI signals for excitation into the $45D_{5/2}$ state for the

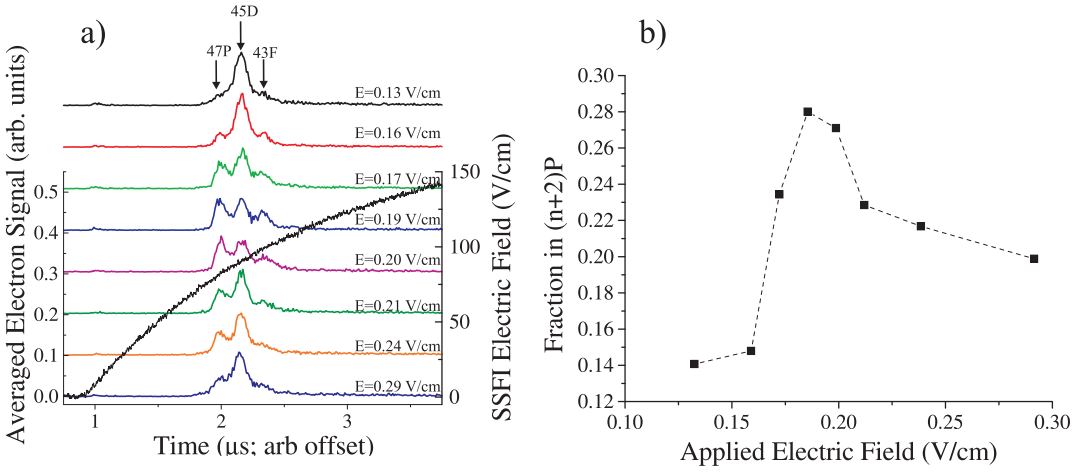

Figure 4.6: Effect of an applied electric field, E, on the probability for state-mixing collisions for excitation into the $45D_{5/2}$ state. Panel a) shows SSFI signals after an interaction time of $\tau_{\rm FI} = 100$ ns for different values of E along with the SSFI electric field pulse. Panel b) shows the fraction of the total SSFI signal in $47P$ states as a function of E.

indicated values of the applied electric field. The fraction of the FI signal in $47P$ and $43F$ states clearly depends on the applied field. In Fig. 4.6b I plot the fraction of the FI spectrum in $47P$ states as a function of the applied electric field and determine the resonant field $E_{\rm F} = 0.19$ V/cm. This value is somewhat lower than the calculated values of Förster-resonance fields given in Fig. 2.6 of 0.24 V/cm, 0.27 V/cm, and 0.34 V/cm, which are expected to merge into a single signature in the experiment, as seen in Fig. 4.6b. Stray electric fields in the atom trapping region likely cause the discrepancy between the measured and the theoretical Förster-resonance fields. We believe the stray fields are caused by the presence of the 50 V electron focusing electrodes shown in Fig. 3.5a. We cancel the longitudinal component of this field using a small extra voltage applied to the cylindrical field-ionization electrodes but we cannot cancel the transverse components.[3] In the following, we use the electric fields $E = 0$ and $E = E_{\rm F} = 0.19$ V/cm to study the counting statistics of Rydberg

[3]We determine the extra voltage to apply to the electrodes to minimize the unwanted electric field in the atom trapping region by tuning our upper transition laser to excite an $nP_{3/2}$ level. Since the transition $5P_{3/2} \rightarrow nP_{3/2}$ is dipole-forbidden, it can only be driven in the presence of an electric field. We minimize the stray electric field by minimizing the $nP_{3/2}$ Rydberg atom signal as the small compensation voltage is varied.

excitations for van der Waals and dipole-dipole interactions, respectively.

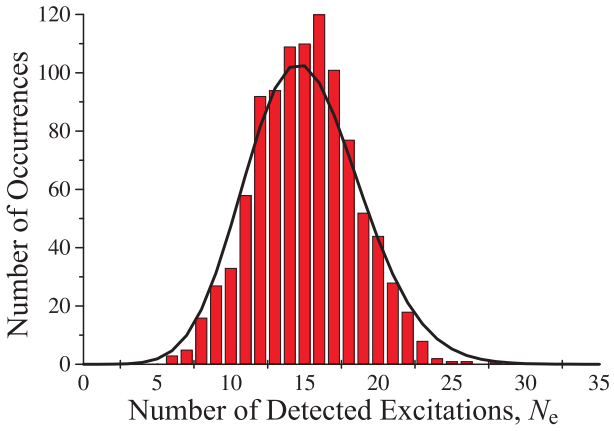

Figure 4.7: Probability distribution of the number of detected Rydberg excitations when the frequency of the upper transition laser is chosen to excite the $45D_{5/2}$ state in a field E_F, obtained from 1000 experimental cycles. The Q-value of this distribution is -0.24. For reference, a Poisson distribution with the same mean is plotted as the solid line.

Using the procedure outlined above, we obtain the Rydberg excitation number distributions for excitation in zero applied field and an applied field $E = E_F$. Figure 4.7 illustrates the fact that the improvements to the experimental procedure do indeed allow us to measure sub-Poissonian counting distributions. This figure shows the distribution of the number of excitations in an applied field of E_F along with a Poissonian distribution with the same average. A cursory inspection of the figure reveals that the Rydberg excitation statistics are sub-Poissonian. The distribution has a Q value of -0.24, the narrowest single distribution we have measured. The distribution is significantly more sub-Poissonian than any values given in Fig. 4.3. We attribute the improved statistics to the improvements to this experiment described above.

It is important to distinguish the Q-value of the distribution that we detect, henceforth referred to as Q_D, from the Q-value of the actual distribution of Rydberg excitations, Q_A, that we would detect if we had a detector with efficiency $\eta = 1$. Q_A is related to Q_D through $Q_D = \eta Q_A$ [92]. If we assume that our MCP detector has a

typical detection efficiency ($\eta \sim 0.5$), we find that the distribution shown in Fig. 4.7 has $Q_{\mathrm{A}} \approx -0.5$. Thus, the true distributions of number of Rydberg excitations are significantly narrower than the distributions that we detect.[4] Values of $Q_{\mathrm{A}} \approx -0.5$ are in the same range as the Q-values predicted in Ref. [29] for a similar system.

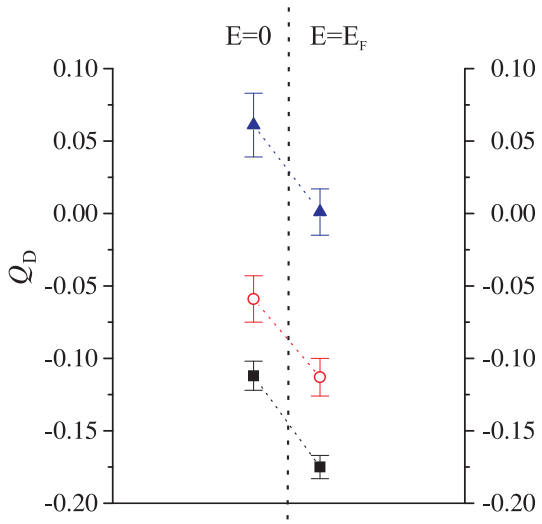

Figure 4.8: Average detected Q-value for excitation in the presence of no electric field and an applied field of E_{F} for three densities: $\rho = 5 \times 10^{11}\mathrm{cm}^{-3}$ (squares), $\rho = 2 \times 10^{11}\mathrm{cm}^{-3}$ (circles), and $\rho = 1 \times 10^{11}\mathrm{cm}^{-3}$ (triangles). The density is varied by varying the amount of time atoms are held in the dipole trap, τ_1, before excitation.

In Fig. 4.8, I plot the average value of Q_{D} for excitation in the presence of no applied field and in the presence of an applied field E_{F}. Q_{D} values are measured for several distributions with 1000 averages each. These values of Q_{D} are averaged and I display them along with the uncertainty, which is given by the standard deviation of the measured Q_{D}-values divided by the square root of the number of averages. This was done for three different ground-state atom densities.

One may immediately see that there is a marked reduction in the Q_{D}-value when the atoms are excited in the presence of an electric field E_{F} compared with the excitation in zero field. We attribute this drop to an increase in the magnitude of

[4] This also implies that the true distributions for the points in Fig. 4.3 are actually more super-Poissonian than the displayed values indicate.

the level shifts, *i.e.* a strengthening of the excitation blockade, when $E_{\rm F}$ is applied. It is clear from the figure that a reduction in ground-state atom density increases $Q_{\rm D}$-value of the Rydberg-atom counting distributions. However, the reduced density does not diminish the *relative* change in the $Q_{\rm D}$-value when the statistics in zero field are compared with the statistics in a field $E_{\rm F}$. The effectiveness of a blockade may only be measured by relative changes in $Q_{\rm D}$ since the absolute value of $Q_{\rm D}$ depends sensitively on experimental conditions. Therefore, we conclude that in the displayed range of densities, the counting statistics become broader as density is decreased but the dipole blockade mechanism becomes no less effective, *i.e.* the relative change in Q for $E = 0$ and $E = E_{\rm F}$ is independent of density.

To further illustrate the reasons for the improved values of $Q_{\rm D}$ in this experiment, I estimate the average number of ground-state atoms per bubble. For the $E = 0$ case, I follow the procedure described in Sect. 4.2.3 since the interactions are primarily van der Waals in nature (see Fig. 2.2). For the case $E = E_{\rm F}$, the energy detuning of the channel in Eq. 4.5 is zero, so it is not valid to use Fig. 2.2a, which was obtained perturbatively, to calculate the bubble radii. Instead I assume the energy level shift is given by the matrix element in Eq. 2.7 which has a value of $\sqrt{2} \times |\langle ...|V|...\rangle| = \sqrt{2} \times 0.36 n^{*4}/R^3$ for the channel in Eq. 4.5 for $\theta = 0$ (see Eq. 2.15 and Fig. 2.1). I assume the θ-dependence of the energy shift is $|1 - \frac{3}{2}\sin^2\theta|$, which is found from the angular dependence of the terms which change $m_{\rm J}$ by ± 1 in Eq. 2.4, as required by the channel in Eq. 4.5. I then use the procedure outlined in Sect. 4.2.3 to calculate the bubble volume. The number of atoms per bubble which result from this calculation are given in Table 4.1 for each density and electric field.

For the highest density displayed in Fig. 4.8, $\rho = 5 \times 10^{11}$ cm^{-3}, $N_{\rm gs} = 20$ in zero field and $N_{\rm gs} = 90$ in an applied field $E_{\rm F}$. Therefore, it is no surprise that the $Q_{\rm D}$-

Density (cm^{-3})	$E = 0$	$E = E_\mathrm{F}$
5×10^{11}	20	90
2×10^{11}	7	40
1×10^{11}	4	20

Table 4.1: Number of atoms per bubble for $E = 0$ and $E = E_\mathrm{F}$

values corresponding to both cases are sub-Poissonian, with the case E_F being the most highly sub-Poissonian. For densities $\rho = 2 \times 10^{11}$ cm^{-3} and $\rho = 1 \times 10^{11}$ cm^{-3}, $N_\mathrm{gs} = 7$ and 4 in zero field and $N_\mathrm{gs} = 40$ and 20 in a field E_F. Thus it is reasonable that the Q_D-values remain sub-Poissonian or near zero for the values displayed in Fig. 4.8, and that the statistics are always narrower in a field E_F for a given density.

Based on the listed values of N_gs, however, one would expect that all Q_D-values for $E = E_\mathrm{F}$ should be lower than all Q_D-values for $E = 0$, but this is not the case. We attribute this discrepancy to the method that we use to achieve lower densities in our dipole trap. In order to avoid unwanted effects from excitation in the spatial wings of our Rydberg excitation laser (see Fig. 4.5), we wish to keep the FWHM of the dipole trap less than the FHWM of the laser beam. Therefore, we cannot lower the density by allowing the atoms in the dipole trap to freely expand before excitation, as described in Sect. 3.2. To achieve lower densities without affecting the width of the atom distributions, we hold the atoms in the dipole trap while the MOT trapping light is off for longer times τ_1 before exciting them to Rydberg states. This allows resonant stray light, that we cannot eliminate, more time to scatter atoms out of the dipole trap. The longer the atoms are subjected to resonant stray light, the hotter the atoms become and the less consistently the dipole trap fills from one experimental cycle to the next. We attribute the fact that all Q_D-values for $E = E_\mathrm{F}$ are not lower than all Q_D-values for $E = 0$ to added noise in our system as the density is lowered, introduced by the resonant stray light.

4.4 "False" blockades

While the extremely large electric polarizabilities and strong atom-atom forces that characterize Rydberg atoms make excitation blockades possible, they also lead to secondary effects which may "mimic" the blockade and make true signatures of the blockade difficult to detect. There is a trade-off between achieving a high single-atom Rydberg excitation probability, which is required for blockade effects to become noticeable, and avoiding collisions and the generation of free ions.

It is well-known that static or motion-induced collisions between Rydberg atoms may lead to Penning ionization, a process in which one collision partner is ionized and a nearly stationary free ion remains in the atom trapping region [48, 49, 51]. In fact, this process is explored in detail in Sect. 6.4.2 of this thesis. It has been pointed out, however, that free ions in the atom trapping region may generate substantial local electric fields that Stark-shift the energy levels of nearby atoms and cause an electric-field induced level shift of the collective state $|N, 2\rangle$. This can mimic the effect of a true excitation blockade [11, 24, 25, 93]. To illustrate this point, consider Fig. 2.5. There are three Förster resonances for $45D_{5/2}$ states in the range 0.2-0.4 V/cm, corresponding to different allowed m values for the F state [66]. One free charge creates an electric field in this range at distances of $6 - 8.5$ μm, distances larger than estimated bubble radii in the experiments described above. Therefore, one free charge present during excitation can create electric fields comparable to or larger than E_{F} for atoms in more than one bubble and significantly shifts the energy levels of the collective state $|N, 2\rangle$.

In order to minimize the effects of free charges on our excitation dynamics, we choose optical excitation pulses with intensity FWHM of ~ 100 ns, limiting atomic

motion and interactions during the pulse and minimizing the number of free ions present during excitation. We show in Sect. 6.4.2 that increasing the width of our excitation pulses by a factor of as little as five can lead to a five- to ten-fold increase in the number of free ions created during excitation. There is, however, a limit to how short the excitation pulses may become. As pulses become shorter, their transform-limited bandwidths grow and stronger interactions are required to ensure that interaction-induced level shifts are greater than the bandwidth. For example, a 1 ns pulse has a transform-limited bandwidth of ~ 150 MHz, while our 100 ns pulses have a transform limit of 1.5 MHz. Therefore, the bubble radius for excitation to the $45D_{5/2}$ state in the presence of a field E_{F} drops from ~ 5 μm to ~ 1 μm when a 1 ns pulse is used instead of a 100 ns pulse.

The negligible number of free ions created before and during excitation by our 100 ns pulses is illustrated in Fig. 4.9. For both excitation in a MOT and in a dipole trap, the fraction of the total electron signal that comes from free electrons is $\lesssim 1\%$. Since we detect $\sim 15-30$ electron counts on our MCP, this corresponds to an average of 0.15 to 0.3 free electrons detected per experimental cycle. Thus we conclude that the secondary effects associated with free ions are not significant in our experiment, and 100 ns pulses represent a good tradeoff between minimizing the creation of free ions while also minimizing the pulse bandwidth.

Another feature of Fig. 4.9 worth noting is that the SSFI spectrum for $E = E_{\mathrm{F}}$ contains a large amount of signal in the $43F_{7/2}$ and $47P_{3/2}$ states that are produced in state-changing collisions. While we will examine state changing collisions in great detail in Chapter VI, I note here that for van der Waals interactions at $n = 45$, 54, 68, and 79, the fraction of the electron signal resulting from state changing collisions are relatively low. In other words, most of the electron signal belongs to the initially

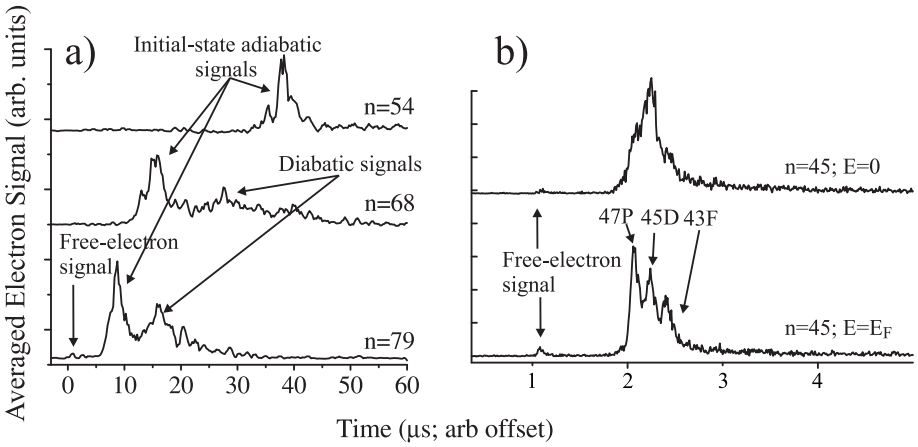

Figure 4.9: a) State selective field ionization spectra for excitation into the 54, 68, and $79D_{5/2}$ states in a MOT in zero applied electric field. b) Spectra for excitation into the $45D_{5/2}$ state in zero applied electric field and an applied field of $E_{\rm F}$.

excited state or diabatic field ionization peaks. However, in the presence of $E_{\rm F}$, there appears to be an extremely large probability for state-changing collisions. The fact that we still see a strong blockade appears to be a mystery since $43F_{7/2}+47P_{3/2}$ atom pairs may seemingly be created only by populating the $|N,2\rangle$ state. Although this is not entirely understood, theoretical work in progress suggests that the blockade may still function effectively while large numbers of $43F_{7/2}+47P_{3/2}$ pairs are produced. We will revisit this subject in Chapter VI and it will likely be discussed at length in future work.

A final process which may lead to "false" blockades is detector saturation. Saturation leads to detected atom distributions which have a false tendency towards smaller number fluctuations and will produce atom counting distributions which appear narrower than they actually are. There are two types of saturation which may lead to these unwanted effects. First, we count individual voltage pulses from the MCP after they have gone through a discriminator. Therefore, two pulses coming at the same instant of time and producing one pulse with double the amplitude will be counted as one pulse. We have taken great care to choose our FI ramp speeds so that

the MCP pulses, which have a width of 5 ns, have a negligible probability to overlap in time. For example, if 15 counts are detected in a 1 μs time interval, such as in Fig. 4.6b, the MCP counts will be separated by ~ 67 ns on average, which is over ten times their width. Second, spatial saturation can also lead to falsely narrow atom-counting distributions. If two electrons hit the same spot on the MCP detector, they will be recorded as one electron. We have verified that this does not significantly affect our measurements by measuring the Q_D-values of distributions obtained for excitation to the $84D_{5/2}$ state in a MOT for 50, 35, 20, 10 and 5 detected excitations. The Q_D-values did not change by more than ± 0.1, which is about the same range as the error bars on the points in Fig. 4.3. Thus, we conclude that detector saturation is not significant when we detect 30 excitations or less.

CHAPTER V

Double-resonance spectroscopy of interacting Rydberg-atom systems

In the previous chapter, I presented experimental evidence for excitation blockades in systems with relatively few Rydberg excitations and studies of the effectiveness of these blockades as a function of different experimental control parameters (principal quantum number and applied electric field). Likewise, several other groups have seen strong evidence for excitation blockades in similar systems [23–26]. However, until now there has been no direct spectroscopic proof that the blockade mechanism is operative. Such proof would require one to show that the excitation to the collective state involving two Rydberg excitations occurs at a transition frequency that differs from that of the first excitation. In this experiment, we use optical excitation pulses to probe the first two steps of the Rydberg excitation ladder, and so provide direct proof of the blockade mechanism [94].

5.1 Description of the experiment

In this chapter, I adopt a more realistic picture of the energy spectrum of the collective states $|N, k\rangle$ (where N atoms coherently share k Rydberg excitations) than the picture outlined in Figs. 1.1 and 4.1. The energy spectra in these figures are drawn for the simplifying case of two atoms in a bubble, so that the level shift of the state

$|N,2\rangle$ results from binary interactions of the kind considered in Chapter II. Thus, for van der Waals interactions the doubly-excited state in the Rydberg excitation ladder consists of a single discrete level, $|N,2\rangle$, which is shifted by $\Delta W^{(2)} \propto n^{*11}/R^6$ for van der Waals interactions[1] (see Sections. 2.2 and 2.3.2). Likewise, for dipole-dipole interactions the doubly-excited state consists of two discrete levels $|N,2\rangle_+$ and $|N,2\rangle_-$ which are symmetrically shifted above and below the interaction-free energy by $\Delta W^{(1)} \propto n^{*4}/R^3$ (see Eq. 2.7 and Sect. 2.3.1). The specific nature of the interaction and the number of states $|N,2\rangle$ that may be excited can be changed by the application of a static electric field, as described in detail in Appendix A.

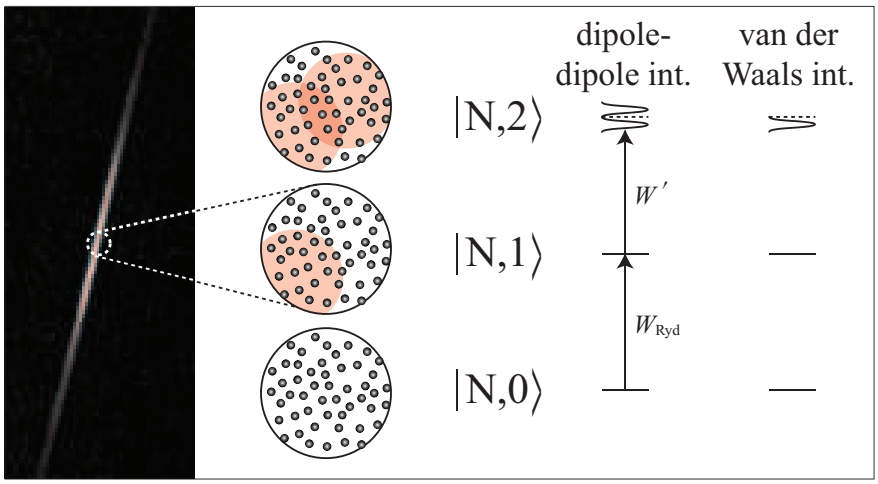

Figure 5.1: The left panel shows a shadow image of atoms in an optical dipole trap. The right panel shows a bubble with zero, one, or two Rydberg excitations. The nature of the energy-shifted band of states $|N,2\rangle$ depends on whether the interactions are resonant dipole-dipole or van der Waals in nature. Due to these interactions, the $|N,1\rangle \rightarrow |N,2\rangle$ transition energy, W', differs from the energy of a single Rydberg excitation, W_{Ryd}.

In the experiment described in this chapter, however, we spectroscopically measure the energy shift of the many-body states $|N,2\rangle$ for the realistic case where the number of atoms per bubble, N, is large. In this case the states $|N,2\rangle$ are not discrete, but form a *band* of energies, as indicated in Fig. 5.1, because the two

[1] There are actually two states $|N,2\rangle$ but only one has appreciable excitation probability. The state that is ignored has excitation probability proportional to $|\frac{V}{\Delta}|^2$ where V is the coupling strength and Δ the energy detuning of the dominant interaction channel (see Appendix A). Thus, if Δ is large, the probability to excite this state is small.

excitations are coherently shared among many atom pairs that are separated by a range of different distances.[2] The nature of these energy bands can be inferred by analogy with the level structure of the two-atom case (see Appendix A) or can be determined by direct calculation [2]. For dipole-dipole interactions, the states $|N, 2\rangle$ are composed of two bands of levels, symmetrically located above and below the value $2W_{\mathrm{Ryd}}$ (where W_{Ryd} is the single Rydberg-excitation energy) [2]. For van der Waals interactions, $|N, 2\rangle$ is composed of a single band of levels shifted by the values $\Delta W^{(2)}$ calculated in Chapter II. In our experiment we use two pairs of optical pulses to measure the energy shifts of the states $|N, 2\rangle$ for these two cases. One pair of laser pulses resonantly excites the state $|N, 1\rangle$, and a second pair of pulses is used to map out the energy bands associated with the states $|N, 2\rangle$.

5.2 Details of the experimental implementation

For the reasons described in Sect. 4.3, this experiment was performed using atom clouds created by an optical dipole trap rather than a MOT. In order to achieve high densities ($\sim 4 \times 10^{11}$ cm^{-3}) and narrow (16 μm wide) atom traps, we optically excite atoms $\tau_2 = 1$ μs after the dipole trap light is turned off. The lower and upper transition laser pulses are created via amplitude- and frequency-modulation of acousto-optic modulators (AOMs) as described in Sect. 3.3.1; however, this is the only experiment described in this thesis for which the pulse timing diagram shown in Fig. 3.5b does not apply. Unlike the other experiments, where Rydberg excitation occurs during one contiguous interval of time, this experiment involves two separate stages of Rydberg excitation. There is a separate stage to excite each of the first two steps in the ladder of Fig. 5.1.

[2]Since $|N, 2\rangle$ represents a *band* of states and not a single quantum state, it is not a proper ket. Nonetheless, for convenience and consistency with above discussions I adopt this notation.

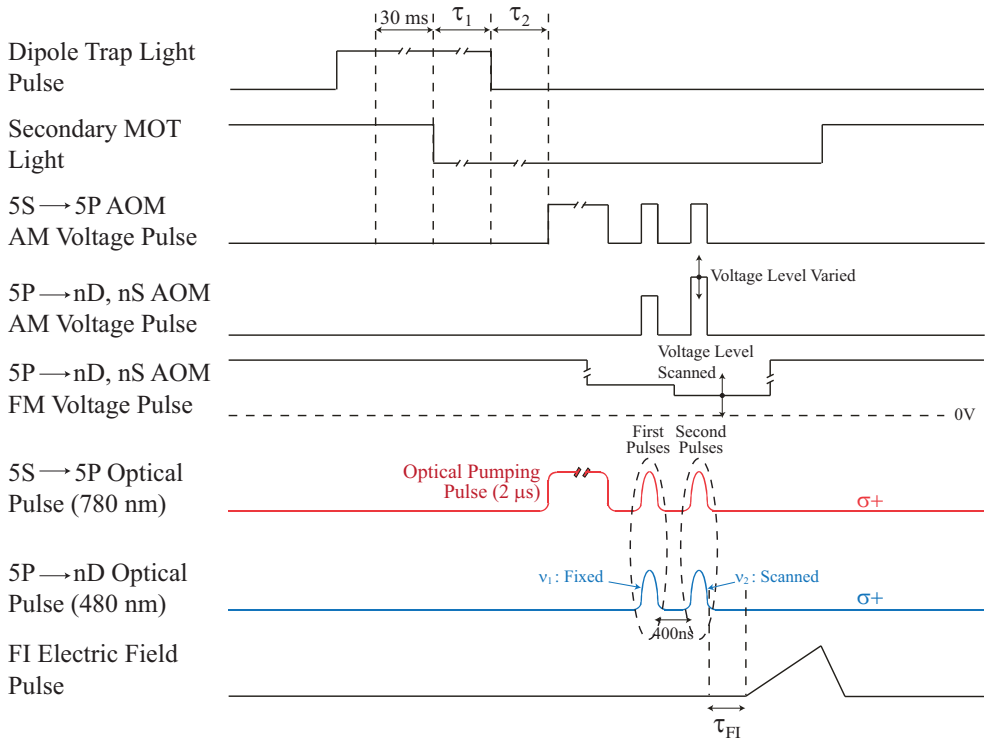

Figure 5.2: Experimental timing diagram for the double-resonance spectroscopy experiment described in this chapter.

To measure the spectra of the transitions $|N,0\rangle \rightarrow |N,1\rangle$ and $|N,1\rangle \rightarrow |N,2\rangle$, we apply two pairs of optical pulses, labeled as "first pulses" and "second pulses" in the timing diagram shown in Fig. 5.2. We need two *pairs* of pulses because each step in the energy ladder of Fig. 5.1 is the two-step excitation to a Rydberg state shown in Fig. 3.4. The two pairs of pulses are separated by 400 ns in time, which is the lower limit set by the switching time of the acousto-optic modulators (AOMs). Each pair of pulses contains a 780 nm pulse and a coincident 480 nm pulse, which we refer to as the lower-transition and upper-transition pulses, respectively.[3] The lower-transition pulses are always resonant with the $5S_{1/2} \rightarrow 5P_{3/2}$ transition. The frequency of the first upper-transition pulse, ν_1, is resonant with the interaction-free transition frequency of $5P_{3/2} \rightarrow 45D_{5/2}$, while the frequency of the second upper transition

[3]These are not to be confused with the $|N,0\rangle \rightarrow |N,1\rangle$ and $|N,1\rangle \rightarrow |N,2\rangle$ transitions in Figure 5.1.

pulse, ν_2, is scanned in 4 MHz steps about ν_1 using an AOM. The frequencies of the upper-transition pulses are controlled by the voltage sent to the frequency modulation input of the AOM. The first pair of pulses primarily drives the $|N,0\rangle \rightarrow |N,1\rangle$ transition shown in Fig. 5.1. The second pair of pulses is used to probe the energy shifts of the states $|N,2\rangle$ as the frequency ν_2 is scanned.

In the experiment it is essential to have a second upper-transition pulse (with frequency ν_2) of the same intensity as the first upper-transition pulse (with frequency ν_1). However, as the frequency ν_2 is scanned, there are unavoidable intensity variations that result from the frequency response of the optical system (AOM and fiber). We remedy this problem by actively controlling the intensity of the second pulse with a feedback scheme that utilizes the amplitude-modulation capability of the AOM. Since the details of this procedure are not essential to understanding the main results of this experiment, they are described in Appendix B.

5.2.1 Experimental procedure

In this experiment, as in Sect. 4.3, we excite to states that interact via either dipole-dipole or van der Waals interactions by changing the value of the electric field applied at the time of excitation. For $45D_{5/2}$ states, the level shifts of $|N,2\rangle$ are negative and primarily van der Waals in character in zero applied field (see Fig. 2.2). In an applied field $E_{\rm F}$ the interaction channel in Eq. 4.5 is exactly resonant, the atoms interact via dipole-dipole interactions, and the states $|N,2\rangle$ are symmetrically split about the interaction-free value, $2W_{\rm Ryd}$.

For this experiment, we again determine experimentally the Förster resonant electric field, $E_{\rm F}$, by following the procedure outlined in Sect. 4.3.1, *i.e.* we examine the amount of product-state mixing in the SSFI signals due to the channel in Eq. 4.5 as a function of the applied electric field. We determined that the resonant elec-

tric field $E_{\mathrm{F}} = 0.23$ V/cm. This value is slightly different than the value quoted in Sect. 4.3, presumably because of a minor systematic error in our electric-field calibration that was discovered after this experiment was complete. Although the two values of E_{F} disagree by a small amount, the method described here ensures that the atoms experience the true Förster resonant electric field, regardless of uncertainty in our measurement of its precise value. Maximizing the probability of state-changing collisions due to the channel in Eq. 4.5 ensures that the energy detuning of the channel is approximately zero, even if some experimental conditions change over a period of several months (the time between when these two experiments were performed).

In the following, we use the electric fields $E = 0$ and $E = E_{\mathrm{F}}$ to study Rydberg excitation spectra for van der Waals and dipole-dipole interactions, respectively. To characterize the band structure of the states $|N, 2\rangle$, we record the number of Rydberg excitations produced as we vary ν_2 for three cases: only the first pair of excitation pulses applied, only the second pair applied, and both pairs applied (henceforth referred to as S_1, $S_2(\nu_2)$, and $S_{1+2}(\nu_2)$). The value of S_1 is approximately constant because ν_1 is fixed. We only are interested in its average, denoted as $\overline{S}_1$. The spectrum $S_2(\nu_2)$ corresponds to the transition $|N, 0\rangle \rightarrow |N, 1\rangle$ in Fig. 5.1. Since the first pair of pulses is always resonant with the transition $|N, 0\rangle \rightarrow |N, 1\rangle$, $\overline{S}_1$ is equal to the peak value of $S_2(\nu_2)$. The spectrum $S_{1+2}(\nu_2)$ results from the combined effect of two pulse pairs: the first pair of pulses drives the transition $|N, 0\rangle \rightarrow |N, 1\rangle$ and contributes the constant offset $\overline{S}_1$ to the signal while the second pair of pulses may also drive the transition $|N, 1\rangle \rightarrow |N, 2\rangle$. Since we are interested primarily in the number of Rydberg excitations added by the second set of pulses, in the following we display the spectra $\tilde{S}_{1+2}(\nu_2) \equiv S_{1+2}(\nu_2) - \overline{S}_1$. Figure 5.3 illustrates how we obtain $\tilde{S}_{1+2}(\nu_2)$ from the raw curves that we directly measure, $S_{1+2}(\nu_2)$ and S_1. We compare

$\tilde{S}_{1+2}(\nu_2)$ with $S_2(\nu_2)$ to determine how the Rydberg-Rydberg interactions modify the spectrum of the transition $|N,1\rangle \rightarrow |N,2\rangle$ from the spectrum of the interaction-free transition, $|N,0\rangle \rightarrow |N,1\rangle$. All spectra relevant to this experiment, measured or derived, are listed in Table 5.1 for reference.

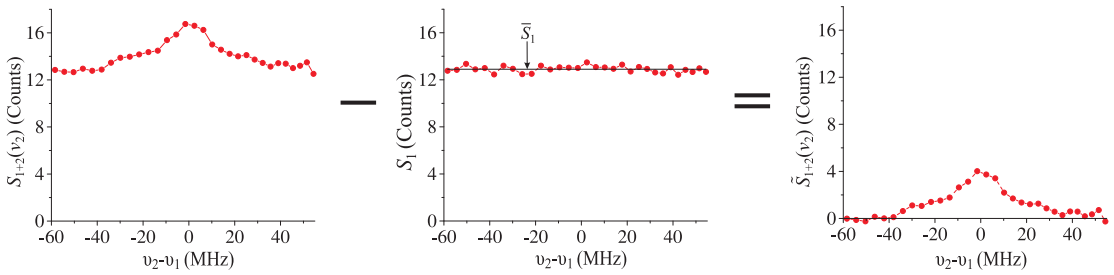

Figure 5.3: Experimentally measured spectra $S_{1+2}(\nu_2)$ and S_1 (left two panels) and the derived spectrum $\tilde{S}_{1+2}(\nu_2)$. I illustrate how $\tilde{S}_{1+2}(\nu_2)$ is generated from two measured spectra.

Spectrum	Measured or Derived	Description
S_1	Measured	Only first pulses enabled; constant function of ν_2
$S_2(\nu_2)$	Measured	Only second pulses enabled; spectrum of $\|N,0\rangle \rightarrow \|N,1\rangle$
$S_{1+2}(\nu_2)$	Measured	Both pulse pairs enabled; includes constant offset of $\bar{S}_1$ contributed by first pulses
$\tilde{S}_{1+2}(\nu_2)$	Derived	$S_{1+2}(\nu_2) - \bar{S}_1$; spectrum of extra counts produced by second pulses when both pulse pairs are enabled
$\hat{S}_{1+2}(\nu_2)$	Derived	$\tilde{S}_{1+2}(\nu_2) - \frac{A_{1+2}}{A_2} \times S_2(\nu_2)$, where A_{1+2} A_2 amplitudes of $\tilde{S}_{1+2}(\nu_2)$ and $S_2(\nu_2)$; spectrum of $\|N,1\rangle \rightarrow \|N,2\rangle$ only

Table 5.1: Summary of all measured and derived spectra relevant to the spectroscopic measurement of the first two transitions in the collective ladder in Fig. 5.1.

5.3 Results for $45D_{5/2}$ states

In Figs. 5.4a and b we display $\tilde{S}_{1+2}(\nu_2)$ (circles; right axis) along with $S_2(\nu_2)$ (squares; left axis) for excitation into $45D_{5/2}$ states. Panels a) and b) show the spectra for zero applied field and an applied field of E_F, respectively. Based on the number of detected Rydberg excitations ($\sim$ 10 in Fig. 5.4), imperfect excitation efficiency, and the SSFI electron detection efficiency ($\sim$ 0.5) we estimate that our excitation vol-

ume (16μm $\times 16\mu$m $\times 19\mu$m) contains of order 40 bubbles. The two spectra $\tilde{S}_{1+2}(\nu_2)$ demonstrate the difference in the nature of the energy shift of states $|N,2\rangle$ for van der Waals (off-resonant) and dipole-dipole (resonant) interactions. The zero-field spectrum $\tilde{S}_{1+2}(\nu_2)$ in Fig. 5.4a exhibits a wing on the negative side of $\nu_2 - \nu_1$, providing evidence for a band of $|N,2\rangle$-excitation frequencies shifted to the low-frequency side of ν_1. This observation is consistent with calculations showing that in zero applied field the interactions among $45D_{5/2}$ atoms are negative (attractive) and primarily van der Waals in nature (see Sect.2.2.1 and Ref. [66]). The spectrum $\tilde{S}_{1+2}(\nu_2)$ in Fig. 5.4b, measured using the applied electric field $E_{\rm F}$, exhibits symmetric wings, providing evidence for two bands of $|N,2\rangle$-excitation frequencies symmetrically located about ν_1. This is consistent with the effect of a Förster resonance on the spectrum of the doubly-excited states $|N,2\rangle$ [2].

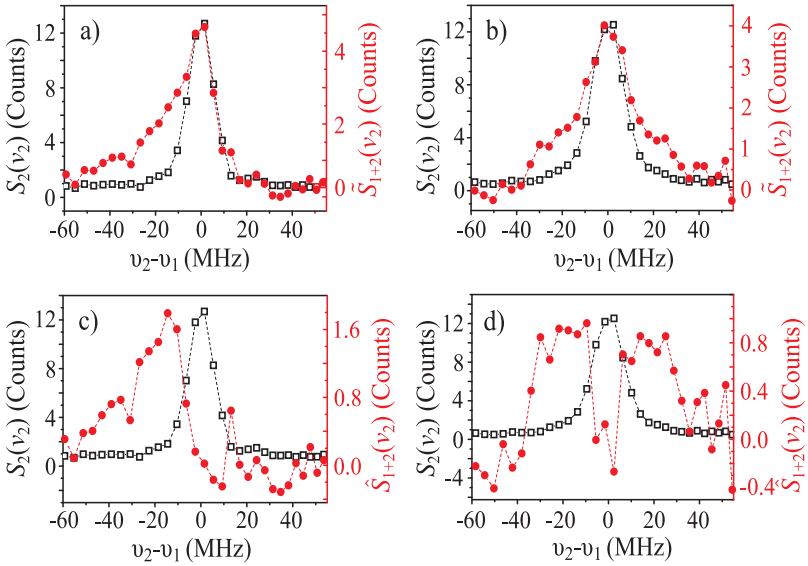

Figure 5.4: Spectra for excitation into the $45D_{5/2}$ state: $S_2(\nu_2)$ (squares; left axes), $\tilde{S}_{1+2}(\nu_2)$ (circles; right axes in a and b), and $\hat{S}_{1+2}(\nu_2)$ (circles; right axes in c and d). Panels a) and c) show data with zero applied electric field and 240 averages per point, while panels b) and d) show data with an applied field of $E_{\rm F}$ and 200 averages per point.

It is important to note that the first set of laser pulses does not excite all bubbles from the state $|N,0\rangle$ to the state $|N,1\rangle$. To minimize power broadening of the

$|N,0\rangle \rightarrow |N,1\rangle$ transition, we limit the Rabi frequencies of the lower- and upper-transition pulses to $\Omega_{5S\rightarrow 5P} = 3.5$ MHz and $\Omega_{5P\rightarrow nD} \sim 3$ MHz, resulting in less than optimal excitation efficiency. We have seen that for these Rabi frequencies the number of Rydberg excitations does not fully saturate, *i.e.* if the intensity is increased more excitations may be created on the $|N,0\rangle \rightarrow |N,1\rangle$ transition. Therefore, the action of the second pair of laser pulses is two-fold: bubbles left in $|N,0\rangle$ after the first pair of pulses are driven on the transition $|N,0\rangle \rightarrow |N,1\rangle$ while bubbles left in $|N,1\rangle$ after the first pair of pulses are driven on the transition $|N,1\rangle \rightarrow |N,2\rangle$. As a result, the spectra $\tilde{S}_{1+2}(\nu_2)$ in panels a) and b) of Fig. 5.4 are a weighted sum of $S_2(\nu_2)$, shown in the same panels, and the spectrum of the transition $|N,1\rangle \rightarrow |N,2\rangle$. To isolate the latter, we subtract $(A_{1+2}/A_2) \times S_2(\nu_2)$ from $\tilde{S}_{1+2}(\nu_2)$, where A_{1+2} and A_2 are the amplitudes of the peaks in $\tilde{S}_{1+2}(\nu_2)$ and $S_2(\nu_2)$, respectively. The results are shown in panels c) and d) of Fig. 5.4 and are henceforth referred to as $\hat{S}_{1+2}(\nu_2)$. The spectrum $\hat{S}_{1+2}(\nu_2)$ in Fig. 5.4c illustrates that off-resonant, attractive van der Waals interactions result a single, red-shifted energy band of states $|N,2\rangle$. Similarly, the spectrum $\hat{S}_{1+2}(\nu_2)$ in Fig. 5.4d illustrates that resonant, dipole-dipole interactions result in two energy bands, symmetrically located above and below twice the single Rydberg-atom energy. The shapes of the spectra $\hat{S}_{1+2}(\nu_2)$ in these plots are consistent with our expectations, which are schematically represented in Fig. 5.1 for the two interaction regimes.

5.4 Results for $43D_{5/2}$ states

The sign of the van der Waals shift can be changed between attractive and repulsive by choosing appropriate quantum states and/or applied electric fields. In Figs. 5.5a and b, I show averaged SSFI signals for excitation into $43D_{5/2}$ states and

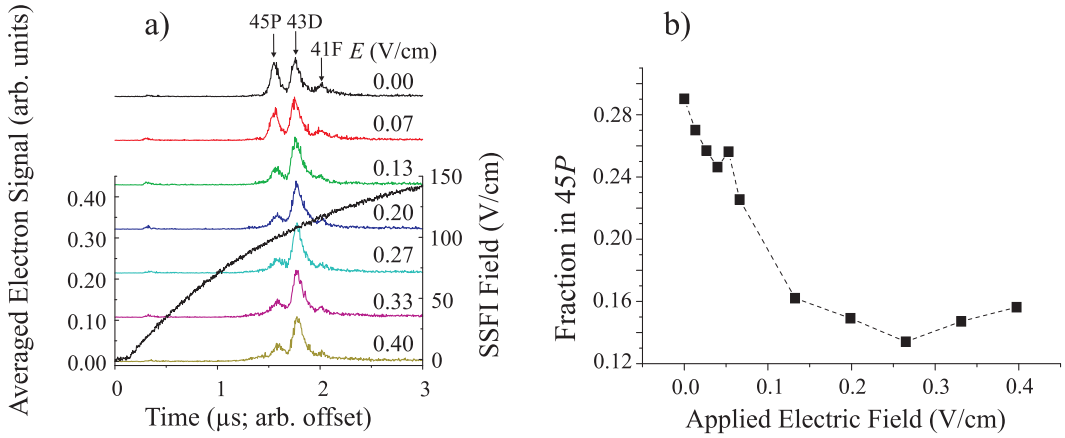

Figure 5.5: Effect of an applied electric field, E, on the probability for state-mixing collisions for excitation into the $43D_{5/2}$ state. Panel a) shows SSFI signals after an interaction time of $\tau_{\mathrm{FI}} = 700$ ns for different values of E along with the SSFI electric field pulse. Panel b) shows the fraction of the total SSFI signal in $45P$ states as a function of E.

the fractions of the SSFI signals in $45P$ states for a range of applied electric fields. This data confirms what is predicted in Fig. 2.7b, namely that a Förster resonance exists for $43D_{5/2}$ near zero applied electric field; this resonance is due to the channel

$$2 \times 43D_{5/2} \rightarrow 41F_{7/2} + 45P_{3/2} \quad . \tag{5.1}$$

In zero electric field, the infinite-separation energy defect of this channel is only -8 MHz (product states lower in energy). The channel becomes more off-resonant as an electric field is applied, changing the character of the interaction to van der Waals. The perturbative calculation of the interaction energy for $43D_{5/2}$ states in a nonzero applied field, shown in Fig. 2.7b, indicates that the van der Waals shifts are positive for electric fields in the range 0.1 to 0.45 V/cm. Thus, in the spectra $\tilde{S}_{1+2}(\nu_2)$ we expect to observe evidence for two bands of excitation frequencies symmetrically located about $\nu_2 - \nu_1 = 0$ in zero applied electric field, and for a single, blue-shifted band in an applied field in the range 0.1 to 0.45 V/cm. Measurements of the spectra $S_2(\nu_2)$ and $\tilde{S}_{1+2}(\nu_2)$ for $43D_{5/2}$ atoms in zero electric field and in an applied electric field of 0.15 V/cm, shown in Fig. 5.6a and b, are consistent with these expectations.

Furthermore, the subtracted spectra $\hat{S}_{1+2}(\nu_2)$ confirm the presence of two bands of $|N,2\rangle$ states symmetrically split about $2W_{\rm Ryd}$ in zero field and a single, blue-shifted band of $|N,2\rangle$ states in an applied field of 0.15 V/cm.

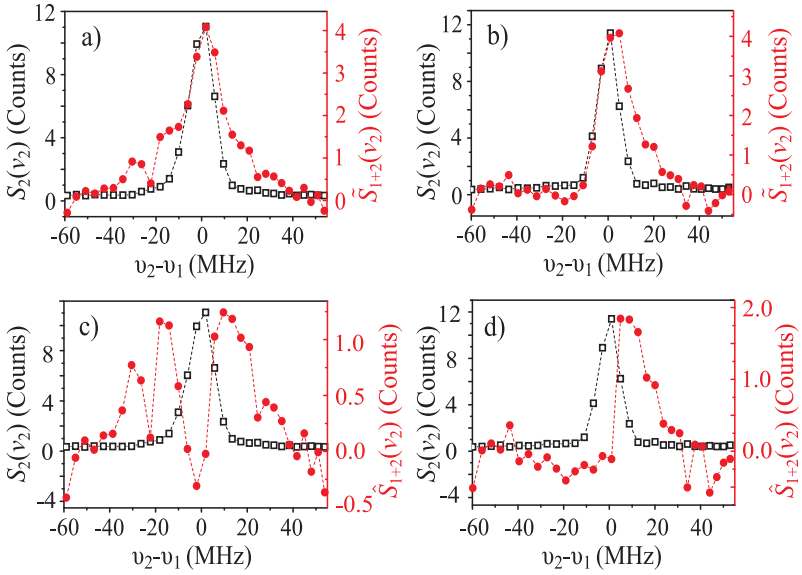

Figure 5.6: Spectra for excitation into the $43D_{5/2}$ state: $S_2(\nu_2)$ (squares; left axes), $\tilde{S}_{1+2}(\nu_2)$ (circles; right axes in a and b), and $\hat{S}_{1+2}(\nu_2)$ (circles; right axes in c and d). Panels a) and c) show data with zero applied electric field and 455 averages per point, while panels b) and d) show data with an applied field of $E_{\rm F}$ and 260 averages per point.

5.5 Discussion and comparison with published theory

One may see from Figs. 5.4d and 5.6c, that the peaks of $\hat{S}_{1+2}(\nu_2)$ are shifted from $\nu_2 - \nu_1 = 0$ by $\sim \pm 20 - 25$ MHz. As stated earlier, the states $|N,2\rangle$ form bands of frequencies because the two excitations are coherently shared among all atom pairs within a bubble, all of which are separated by different distances. For an exact Förster resonance, the contribution to the energy shift of the states $|N,2\rangle$ due to an atom pair separated by a distance R is given by the matrix element in Eq. 2.7, or

$$\Delta W^{(1)}(R) = \sqrt{2} \times 0.36 n^{*4}/R^3 \tag{5.2}$$

for $\theta = 0$ for the channel in Eq. 4.5 (see Eq. 2.15). Therefore, close atom pairs will contribute a larger energy shift than those separated by greater distances. The total

energy spectrum that we measure is a sum of the level shifts due to each possible atom-atom separation, weighted by the probability for two atoms in the bubble to be separated by that distance.

The most probable ground-state atom separation is approximately given by the Wigner-Seitz radius, $R_{\rm ws}$, defined by

$$\frac{4}{3}\pi R_{\rm ws}^3 * \rho = 1 \quad , \tag{5.3}$$

where ρ is the ground-state atom density. The energy shift contributed by atom pairs separated at the Wigner-Seitz radius, or about 0.9 μm, is $\sim$ 2 GHz. Therefore, atom pairs separated by $R_{\rm ws}$ clearly do not provide the dominant contribution to the energy shift of the bands of levels $|N, 2\rangle$. Since the energy shift in Eq. 5.3 scales with R as R^{-3}, the energy shift ($\sim \pm$20 MHz) must be predominantly due to atoms separated by a larger distance. The maximum distance two atoms may be separated and still coherently share an excitation within one bubble is $R_{\rm b}$, or the bubble radius. Additionally, the number of atoms which are separated by a distance R within a bubble scales as R^2, *i.e.* more pairs contribute to the energy shift of the states $|N, 2\rangle$ for large R than for small R. Therefore, we conjecture that the dominant contribution to the observed energy shifts in Figs. 5.4d and 5.6c is due to pairs separated by $R_{\rm b}$. The bubble radius is defined by the condition that the energy shift of doubly excited state at $2R_{\rm b}$, $\Delta W^{(1)}(2R_{\rm b})$, is given by

$$\Delta W^{(1)}(2R_{\rm b}) = \delta\nu_{\rm L} \tag{5.4}$$

where $\delta\nu_{\rm L}$ = 2 MHz is the excitation laser linewidth. Since $\Delta W^{(1)} \propto 1/R^3$, the energy shift due two atoms separated by $R_{\rm b}$ is $\Delta W^{(1)}(R_{\rm b}) = (\frac{1}{2})^{-3}\delta\nu_{\rm L} \sim$ 20 MHz. This is consistent with the frequency displacements of the bands $|N, 2\rangle$ observed in Figs. 5.4d and 5.6c.

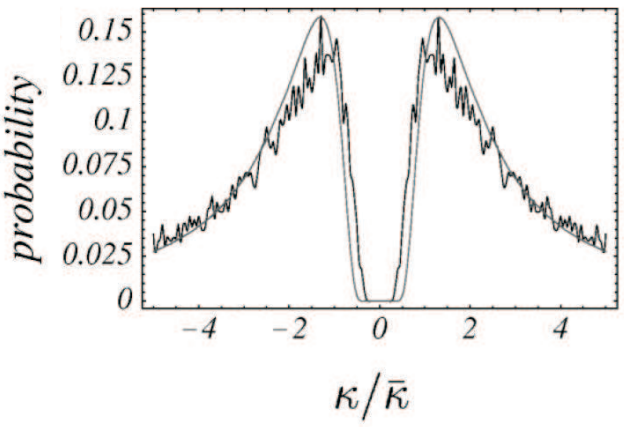

Figure 5.7: Probability distribution for frequency shifts of the band of states $|N, 2\rangle$. The band structure is calculated using a Monte Carlo simulation for 3×10^4 atoms randomly placed in a rectangular box. The frequency axis is in units of $\kappa/\bar{\kappa}$, where κ and $\bar{\kappa}$ are defined in the text. This figure is reprinted with permission from Ref. [2]. © 2001 American Physical Society

While these qualitative considerations describe our data well, we may go further to show that the magnitudes of the observed frequency displacements are in agreement with more complete theoretical calculations presented in Ref. [2]. Figure 2a of Ref. [2] shows the calculated band structure of the states $|N, 2\rangle$ for the case of an exact Förster resonance and I reprint it here in Fig. 5.7. In this figure, the authors plot the energy band structure of the state $|N, 2\rangle$ as a function of the atom-atom coupling strength $\kappa = 0.36n^{*4}/R^3$, scaled by $\overline{\kappa} = 0.36n^{*4}/\Omega$, where Ω is the ensemble volume. We connect this figure with our data by setting Ω equal to the volume of one bubble in our experiment. We estimate the volume of one bubble here by dividing the excitation volume (16 μm $\times$16 μm $\times$19 μm) by the number of bubbles ($\sim$ 40, as estimated above) and find $V_{\rm b} \approx 120\ \mu{\rm m}^3$. The bands in Fig. 5.7 peak at $\kappa/\overline{\kappa} \approx 1.25$. Thus, the displacement, $\Delta W^{(1)}$, of the energy band $|N, 2\rangle$ is given by $\Delta W^{(1)} = \sqrt{2} \times \left(1.25\overline{\kappa}\right) \approx 20$ MHz. This supports our conjecture that the energy shift of the band $|N, 2\rangle$ is due primarily to atoms separated by a distance $R_{\rm b}$.

Since, to my knowledge, there is no detailed calculation of the energy band structure of the states $|N, 2\rangle$ for van der Waals interactions in the literature, I begin

by again assuming that the dominant contribution to the shift of $|N,2\rangle$ for $45D_{5/2}$ states in zero applied field comes from pairs of atoms separated by $R_{\rm b}$. Thus far, we have assumed that the level shifts for $45D_{5/2}$ states scale like R^{-6} (van der Waals scaling) in zero field (see Fig. 2.2a). Therefore, the level shifts for atom pairs separated by $R_{\rm b}$ may again be estimated using simple scaling laws. Specifically, $\Delta W^{(2)}(R_{\rm b}) = (\frac{1}{2})^{-6} \times \delta\nu_{\rm L} \sim 100$ MHz. Since the measured frequency shift of $|N,2\rangle$ in Fig. 5.4c is only ~ 20 MHz, our assumption that the dominant contribution to the level shift comes from atoms separated by $R_{\rm b}$ must be incorrect. Apparently, the dominant contribution to the energy shift comes from atoms with $R > R_{\rm b}$. This implies that there are some atoms outside of $R_{\rm b}$ (where $R_{\rm b}$ is defined in Eq. 5.4), that do not belong to another bubble. The excitation volume is not uniformly filled with bubbles because $R_{\rm b}$ is too small to ensure this condition. Figure 5.8 illustrates the difference between weak interactions (atoms outside the bubble can coherently share excitations with atoms inside the bubble when the state $|N,2\rangle$ is excited with two pulse pairs) and strong interactions (where the excitations are shared only among atom pairs in a given bubble, since the bubbles uniformly fill the excitation volume).

5.6 Limitations of the experimental method

Our method for spectroscopically measuring the energy shifts of the states $|N,2\rangle$ relies on frequency modulation of a single AOM to change the frequency of the second upper-transition pulse relative to the first. As mentioned above this requires a 400 ns delay between the first and second pair of pulses, which leads to several sources of experimental uncertainty. First, as discussed in Sect. 5.3, this delay leads to additional excitation by the second pair of pulses on the $|N,0\rangle \rightarrow |N,1\rangle$ transition when $\nu_2 = \nu_1$. In addition to exciting bubbles that were not excited by the first set

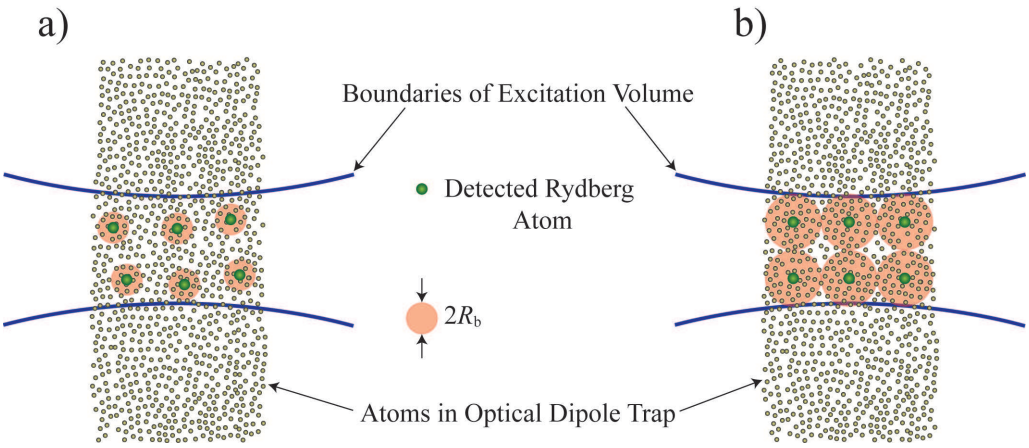

Figure 5.8: Schematic illustration of the Rydberg excitation blockade picture for weak van der Waals interactions (a) and strong dipole-dipole interactions (b). Within the boundaries of the excitation volume (lines), Rydberg excitations created in a cloud of ground-state atoms (small dots) are localized and detected at certain atoms (large green spheres) using a quantum measurement process. In (a) the bubble radius, R_b, is small, so detected Rydberg atoms have a random ordering and the "bubble surfaces" do not touch. In (b) the bubble radius is large, so the positions of detected Rydberg atoms are correlated and the "bubble surfaces" touch.[a]

[a]Note that since the bubbles are not actually real they do not have a "surface." As mentioned earlier, we discuss them because of their utility in describing certain experimental results.

of pulses, the second set of pulses may also coherently drive the transition $|N,1\rangle \rightarrow |N,0\rangle$ for bubbles that are excited by the first set of pulses. That is, they may coherently de-excite bubbles that were initially excited. Finally, in 400 ns the states $|N,1\rangle$ may undergo some dephasing due to weak atomic forces between atoms in adjacent bubbles and state-changing collisions (as described in Chapter VI). While these effects are minor and do not inhibit our ability to see symmetric and asymmetric broadening of the spectra $\tilde{S}_{1+2}(\nu_2)$, we require the additional analysis described in Sect. 5.3 to extract the true energy-shifted spectra of the states $|N,2\rangle$, $\hat{S}_{1+2}(\nu_2)$. A modification of the experimental procedure which will eliminate these sources of error is described in Sect. 7.2.2. We note, however, that the procedure described here provides not only qualitative, but quantitative information about the energy shifts of the states $|N,2\rangle$ for different experimental conditions.

CHAPTER VI

State-mixing and Penning-ionizing collisions

In the experiments described thus far, I have focused exclusively on effects related to the energy level structure of the entangled states, $|N,k\rangle$, that are created when N atoms share k Rydberg excitations. I have considered excitation to $nD_{5/2}$ Rydberg states and assumed that other single-atom Rydberg states are relevant only insofar as couplings to these states account for the level shift of $|N,2\rangle$. In the case of van der Waals interactions, couplings to many such states result in a small energy shift of the doubly-excited state, $|N,2\rangle$. In the case of an exact Förster resonance for the interaction channel in Eqs. 2.14 and 4.5, two symmetrically shifted states, $|N,2\rangle_+$ and $|N,2\rangle_-$ are created which are equal admixtures of the two-particle states $\frac{1}{\sqrt{2}}\big\{|(n-2)F_{7/2}\rangle + |(n+2)P_{3/2}\rangle\big\}$ and $2\times|nD_{5/2}\rangle$. An excitation blockade should prevent the excitation of these states; however, I showed in Chapter V that this state may be populated by applying two pairs of excitation pulses with different frequencies. In this case, if SSFI were used to perform a quantum measurement on the mixed superposition states, $|N,2\rangle_\pm$, by projecting them onto the single-atom basis states, one would measure substantial numbers of atoms in $|(n-2)F_{7/2}\rangle$ and $|(n+2)P_{3/2}\rangle$ states. Thus, it seems that the Hilbert space of detectable Rydberg states is larger than simply $|nD_{5/2}\rangle$ states, but only if we force the population of the

$|N,2\rangle_{\pm}$ states using two excitation frequencies.

In this chapter, however, I investigate in more detail the surprising discovery that we noted in Chapters IV and V; namely, that we can detect significant numbers of $(n-2)F_{7/2}$ and $(n+2)P_{3/2}$ atoms, even when only one set of narrow-linewidth laser pulses, resonant with the $|N,0\rangle \rightarrow |N,1\rangle$ transition, is applied to a blockaded system. This result is inconsistent with a binary theory of Rydberg atom interactions and suggests that many-body effects, or effects due to the simultaneous interaction of many atoms, are significant in our system [70].

Generally, the majority of this chapter deals with state-changing Rydberg-Rydberg collisions and the effect of these collisions on the coherent excitation dynamics and the motion-induced energy exchange dynamics of Rydberg atom systems. Following the discussion of Sect 2.2.3, we look specifically at how the change in magnitude and sign of the level shifts for n near the zero-field Förster resonance at $43D_{5/2}$ affects both types of dynamics. Thus, these results bridge the gap between short time, coherent excitation dynamics and longer time, incoherent, motion-induced dynamics, both of which are due to Rydberg-Rydberg interactions. At the end of this chapter, I briefly discuss measurements related to a different type of collision, Penning-ionizing collisions [70].

6.1 Description of the experiment

In this chapter we examine effects related to the interaction channel that produces the Förster resonances studied in Chapters IV and V,

$$2 \times nD_{5/2} \rightarrow (n-2)F_{7/2} + (n+2)P_{3/2} \quad . \tag{6.1}$$

However, rather than studying the effects of this channel on the excitation statistics or energy level structure of the collective system, we examine its effect on the state

distribution of excited Rydberg atoms and their time evolution. In particular, we expect that two atoms interacting via the collision channel in Eq. 6.1 may produce significant numbers of $(n-2)F_{7/2}$ and $(n+2)P_{3/2}$ atoms only when the infinite separation energy defect of the channel, $\Delta = W_{(n-2)F_{7/2}} + W_{(n+2)P_{3/2}} - 2 \times W_{nD_{5/2}}$, is small and the process is nearly resonant. Other channels that have large matrix elements with $V_{\rm dd}$ may contribute significantly to the energy shift of the state $|N, 2\rangle$[1]. However, these channels are not expected to produce significant numbers of product states in collisions because of their large energy defects. Thus, we focus our attention exclusively on the channel in Eq. 6.1 to study state-mixing collisions. Several groups have studied the energy transfer dynamics of this channel as a function of applied electric field to tune the energy defect through zero [6, 7, 58]. Our study differs in that we tune the energy defect by exciting atoms to states with different principal quantum number n in zero electric field. The energy defects of this channel as a function of, n, are listed in Table 6.1.

n	Δ (MHz)
39	-478
40	-325
41	-199
42	-95
43	-8
44	63
45	121
46	169
47	209

Table 6.1: Infinite separation energy defects of the channel in Eq. 6.1 as a function of principal quantum number, n.

In appendix A we examine in detail the nature of the eigenstates and eigenenergies of two atoms interacting in a single bubble when only the channel in Eq. 6.1 is considered. Although this is a simplification to the experimental system considered

[1] Such as the channel in Eq. 2.13

here, the results provide some insight to our experimental findings. Therefore, in the following we summarize the features of that discussion which are relevant to the experiments described below.

In appendix A it is shown that the operator $V_{\rm dd}$ in Eq. 2.1 will mix the unperturbed states and lead to eigenstates of the interacting system of:

$$|N,2\rangle_{\pm} = \alpha_{\pm}|dd\rangle \pm \beta_{\pm}\{\frac{1}{\sqrt{2}}(|p'f\rangle + |fp'\rangle)\} \tag{6.2}$$

where $|d\rangle, |p'\rangle$, and $|f\rangle$ correspond to the $|nD_{5/2}\rangle$, $|(n+2)P_{3/2}\rangle$, and $|(n-2)F_{7/2}\rangle$ single-atom states. If we assume that these states may somehow be populated, they are excited through matrix elements with the $|dd\rangle$ part of the wavefunction. This is because only the single-atom matrix elements $\langle p|\mu \cdot \mathbf{E}_{\rm laser}|d\rangle$ are nonzero, where the single-particle state $|p\rangle$ corresponds to $|5P_{3/2}\rangle$, μ is the atomic dipole moment operator, and $\mathbf{E}_{\rm laser}$ is the excitation laser field. Once $|N,2\rangle_{\pm}$ are excited, the probability to measure a $p'f$ atom pair is proportional to $|\beta_{\pm}|^2$ if a phase-insensitive quantum measurement is performed. The precise values of $\alpha_{\pm}$ and $\beta_{\pm}$ are determined by the value of Δ for the n state under consideration. If $\Delta \gg V_{\rm dd}$ and positive, $\alpha_{-} \approx \beta_{+} \approx 1$ and $\alpha_{+} \approx \beta_{-} \approx 0$. Thus, only the $|N,2\rangle_{-}$ state may be excited, because only it has significant $|dd\rangle$ character, and it will contain little $|p'f\rangle$ character. Therefore, for large Δ, we expect to observe few $p'f$ pairs. If Δ is small, $|\alpha_{\pm}|^2 \approx |\beta_{\pm}|^2 \approx \frac{1}{2}$. In this case we should excite equal numbers of dd and $p'f$ pairs, except that $\Delta = 0$ corresponds to large energy shifts of $|N,2\rangle_{\pm}$ and a strong blockade. This should inhibit the excitation of the states $|N,2\rangle_{\pm}$ and block the creation of $p'f$ atom pairs. Note that we have not said how $|N,2\rangle$ may be excited, only that if it is the amount of mixing into $p'f$ states will depend sensitively on Δ. In this chapter, we examine experimentally the extent to which these notions hold true.

The experiments described in Sections 6.2 and 6.3 were performed using a MOT

with full diameter of ∼300 μm, a density of $\sim 1.2 \times 10^{10}\text{cm}^{-3}$, and $\sim 1.3 \times 10^6$ atoms. Here we prepare atoms not only in $nD_{5/2}$ states, but also $nD_{3/2}$ and $nS_{1/2}$ states using the two-photon excitation ($5S_{1/2} \rightarrow 5P_{3/2} \rightarrow nD$, nS). The polarization of the upper transition laser pulse is $\sigma+$, π, and $\sigma-$ for excitation from $5P_{3/2}$ into these each of these three states, respectively.[2] We excite atoms with the upper-transition laser frequency selected to excite a given Rydberg state by using the pulse sequence of Fig. 3.5 and determined the state distribution after a variable interaction time, τ_{FI}, using state-selective field ionization (SSFI). The uncertainty in the value of τ_{FI} is 50 ns.

6.2 State-mixing due to static interactions

SSFI electron signals for excitation into $43D_{3/2}$, $43D_{5/2}$, and $45S$ states are shown in Fig. 6.1 along with the field ionization electric field pulse. In this case, the field ionization pulse is applied $\tau_{\text{FI}} = 200$ ns after excitation. Under these conditions, atomic motion is negligible and any state-mixing occurs on a fairly rapid time scale (< 300 ns). The SSFI spectra compared in Fig. 6.1 correspond to states with approximately the same effective principal quantum numbers, $n^* = n - \delta_\ell$, and hence energies, $W = -1/(2n^{*2})$ (the quantum defects are $\delta_S = 3.13$ and $\delta_D = 1.35$) [3]. Therefore, these states ionize at roughly the same electric field, $F = -1/(16n^{*4})$. In the figure, we highlight three regions of the electron signal, labeled A, B, and C. These regions correspond to the ionization electric-field ranges of Rydberg atoms with effective principal quantum numbers $n^* \in]42, 43[$, $n^* \in]41, 42[$, and $n^* \in]40, 41[$. Population in regions A and C is generated as a result of the type of interaction

[2] Whenever n, ℓ, or j is varied, the upper-transition Rabi frequency is kept constant by adjusting the laser intensity by an experimentally determined scale factor. This factor was determined by exciting atoms with low upper transition laser intensity (to prevent suppression of excitation due to the blockade) and measuring the intensities required to create the same number Rydberg of excitations when exciting to $nD_{3/2}$, $nD_{5/2}$, and $(n+2)S_{1/2}$ states. For a given ℓ, or j, the intensities are scaled by n^{*3}.

channels in Eq. 6.1.

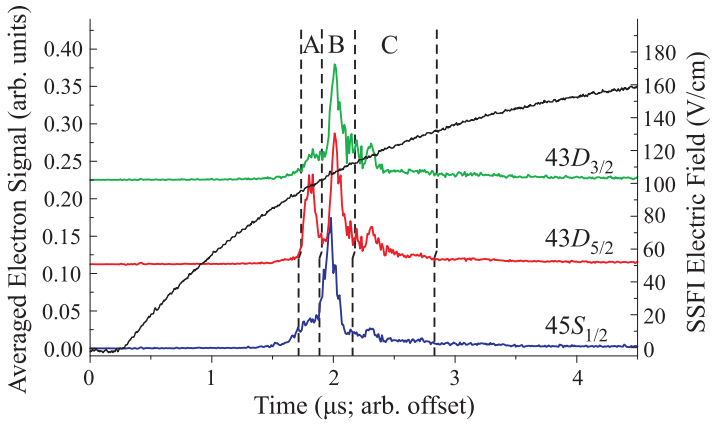

Figure 6.1: Averaged SSFI electron signals (left axis) for excitation into $43D_{3/2}$, $43D_{5/2}$, and $45S_{1/2}$ Rydberg states and the SSFI electric field pulse (right axis). Regions A, B and C correspond to Rydberg atoms populated by direct photoexcitation (B) and combined photoexcitation-collisional processes (A, C).

Figure 6.1 provides evidence for qualitative differences in the state-mixing behavior of different quantum states of approximately equal energy. The $43D_{5/2}$ state, detected in region B, is characterized by significant mixing to $45P$ and $41F$ states, detected in regions A and C, respectively. The $43D_{3/2}$ and $45S_{1/2}$ states, both detected in region B, exhibit much less mixing, owing to the absence of any near-resonant channel for these states. The energy detuning of the channel in Eq. 6.1 is only -8 MHz for $43D_{5/2}$ while the nearest resonant interaction channels for $43D_{3/2}$ and $45S_{1/2}$ states have energy detunings of ~ 300 MHz and ~ 4 GHz.

For laser excitation into $D_{5/2}$ or $D_{3/2}$ states, the nearest-resonant interaction channels involve transitions into higher-lying P- and lower-lying F-states, as in Eq. 6.1, while for excitation into $S_{1/2}$-states all interaction channels only involve transitions into P-states. In all cases shown in Fig. 6.1, a quantitative measure for the amount of mixing into higher-lying P-states is given by S_{A}, the integral of the electron signal detected in region A divided by the total integral. Similarly, mixing into lower-lying states can be quantified via S_{C}, the integral of the signal in region C divided by the

total integral. Here, I choose to analyze the value of S_{A} rather than S_{C} because P-Rydberg states, which make up most of the signal detected in A, ionize over a narrower electric-field range than F states, which in most cases are the dominant signal detected in C [3]. In Fig. 6.2a, I show experimental values of S_{A} as a function of n^* for $D_{3/2}$, $D_{5/2}$, and S states. Evaluating S_{A} for several choices for the integration boundaries that separate regions A, B, and C, we determine that the uncertainty of experimental S_{A}-values ranges from about 0.005 to 0.03, depending on the initially excited Rydberg state. The data in Fig. 6.2b show calculated fractions of Rydberg-state populations in higher-lying P-states (discussed below).

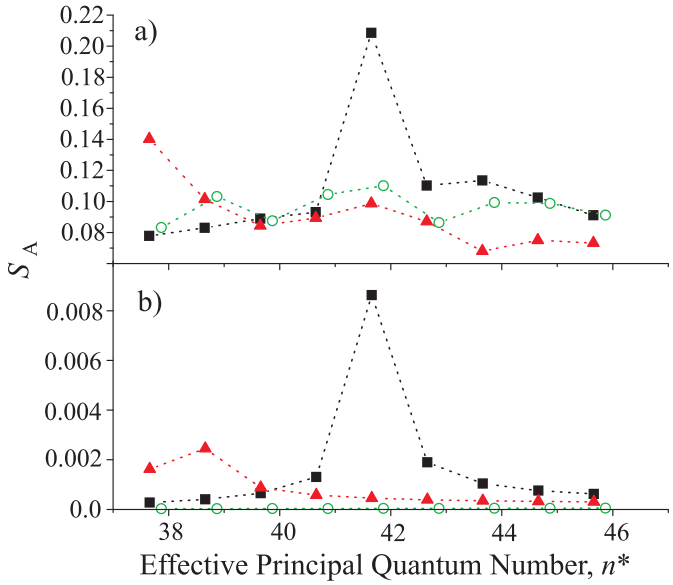

Figure 6.2: S_{A} as a function of the effective principal quantum number of the states into which the atoms are excited. Results are shown for $D_{5/2}$ (squares), $D_{3/2}$ (triangles), and S (circles) states. Part a) experiment, part b) two-body theory.

The curve in Fig. 6.2a for $nD_{5/2}$ states is characterized by a strong enhancement of the mixing at $n^* = 41.65$ (or $n = 43$), where $S_{\mathrm{A}} \approx 0.21$. For $n \neq 43$ the value of S_{A} takes on a smaller, relatively constant background value of ~ 0.09. This observation reflects the fact that the channel in Eq. 6.1 becomes nearly resonant at $n = 43$ and that the energy detuning of the channel becomes significantly larger for $n \neq 43$. To

interpret this result, we first note that the SSFI peaks in Fig. 6.1 overlap somewhat with one another. The integral over region A therefore includes some signal that actually belongs to the B-peak and the integral over region B contains some signal that actually belongs to the A peak.

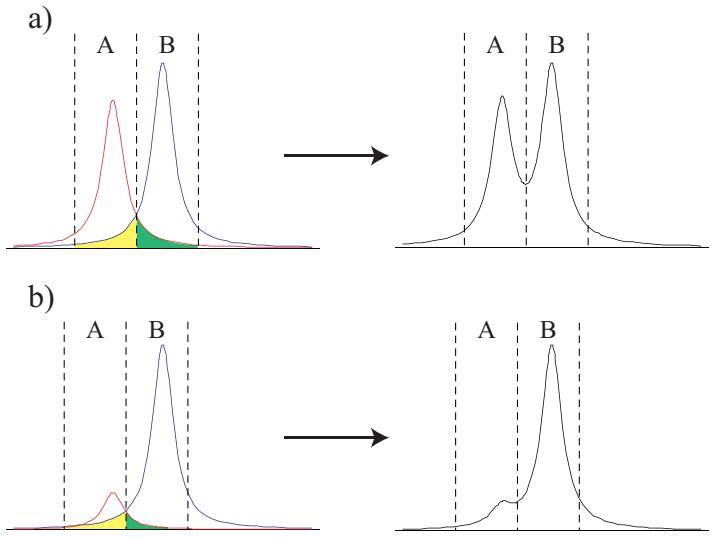

Figure 6.3: Portions of hypothetical SSFI spectra corresponding to regions A and B as defined in Fig. 6.1. We assume that the raw peaks A (red) and B (blue) may be approximated by Lorentzians and add to give a combined partial SSFI spectrum (black). The area of peak A (B) which spills in to the integration range of B (A) is indicated by green (yellow) shading.

The amount of the systematic error in S_{A} caused by the overlap of the SSFI peaks varies as a function of n. This is qualitatively illustrated in Fig. 6.3 by assuming that a hypothetical SSFI spectrum is made up of overlapping Lorentzian peaks.[3] For simplicity we neglect the C peak in our discussion here. We show peaks A and B in red and blue and the component of the total SSFI spectrum belonging to these two peaks in black. The hypothetical integration boundaries that would be used to compute S_{A} are shown as the left two dotted lines. The right boundary of region A is chosen to coincide with the relative minimum between the two peaks, as was the case when the true data was analyzed. The amount of systematic error in S_{A} due to peak overlap may be estimated by the difference in the amount that peak A

[3]We may actually use any bell-shaped curves to qualitatively illustrate our point.

spills into integration range B (green shading) and the amount that peak B spills into integration range A (yellow shading). In panel a) I illustrate cases where the A and B peaks are approximately equal in height, such as for $43D_{5/2}$ spectra. The amount that peak A spills into integration range B is roughly equal to the amount that peak B spills into integration range A. Thus, we conclude that there is little systematic error in S_{A} for $43D_{5/2}$. In panel b) I illustrate cases where peak A is much smaller than peak B, or all of the cases where the energy detuning of the dominant interaction channel is large. In this case, we may immediately see that peak B spills into integration region A much more than peak A spills into the integration region B. Thus, off resonance, *i.e.* for most of the points in Fig. 6.2, there is a large systematic error and we overestimate S_{A}.

Applying the above considerations to the curve for $nD_{5/2}$ states in Fig. 6.2, we conclude that the peak value of S_{A} of 0.21 for $n = 43$ is relatively accurate while for $n \neq 43$ there is a roughly constant systematic error that causes us to overestimate S_{A}. Thus, the contrast in the value of S_{A} between the on- and off-resonance cases is actually greater than it appears in Fig. 6.2. We have verified by Monte Carlo simulation that saturation caused by temporal overlap of MCP-pulses does not significantly alter the S_{A}-values for our experimental parameters. We conclude that for the conditions of Fig. 6.2a, the near-resonance of the channel in Eq. 6.1 at $n = 43$ causes a transfer of up to about 21% of the excited atoms into P-states. For $n \neq 43$ we assume that this fraction is actually less than 9%. This transfer occurs almost instantaneously because of the short duration of the excitation pulses and the almost instantaneous detection. It is important to note that our lower- and upper-transition lasers have linewidths of ~ 2 MHz, or less than the energy defect of the channel in Eq. 6.1 for $n = 43$ (8 MHz). Therefore, the large amount of state-mixing for $n = 43$

is not due to broadband laser excitation.

Inspection of the curve for $nD_{3/2}$ in Fig. 6.2a shows that in the range $n^* < 40$ the detected S_{A}-value increases from the background level of ≈ 0.09 to ≈ 0.14. This rise reflects another, relatively weak, near-resonant interaction identified in Sect. 2.2.2, namely $2 \times 39D_{3/2} \rightarrow 37F_{5/2} + 41P_{3/2}$. Otherwise, the S_{A}-values in Fig. 6.2a largely remain at the background level, in accordance with the absence of any other near-resonant collision channels.

6.2.1 Binary-interaction model

To model the results for $nD_{5/2}$ states in Fig. 6.2a, we numerically solve the full density matrix equations for a two-atom system (including decay from the $5P_{3/2}$ state) in the space:

$$\begin{aligned} &|ss\rangle, |pp\rangle, |dd\rangle, \tfrac{1}{\sqrt{2}}\big\{|sp\rangle + |ps\rangle\big\}, \tfrac{1}{\sqrt{2}}\big\{|sd\rangle + |ds\rangle\big\}, \tfrac{1}{\sqrt{2}}\big\{|pd\rangle + |dp\rangle\big\}, \\ &\tfrac{1}{\sqrt{2}}\big\{|p'f\rangle + |fp'\rangle\big\}, \tfrac{1}{\sqrt{2}}\big\{|sp\rangle - |ps\rangle\big\}, \tfrac{1}{\sqrt{2}}\big\{|sd\rangle - |ds\rangle\big\}, \tfrac{1}{\sqrt{2}}\big\{|pd\rangle - |dp\rangle\big\} \end{aligned} \tag{6.3}$$

assuming binary interactions and negligible atomic motion. The single-atom states $|s\rangle, |p\rangle, |d\rangle, |p'\rangle$, and $|f\rangle$ correspond to the $|5S_{1/2}\rangle$, $|5P_{3/2}\rangle$, $|nD_{5/2}\rangle$, $|(n+2)P_{3/2}\rangle$, and $|(n-2)F_{7/2}\rangle$ states, respectively. The $\frac{1}{\sqrt{2}}\big\{|p'f\rangle - |fp'\rangle\big\}$ state is omitted because it does not couple to any other state. The excitation is modeled by two coincident Gaussian laser pulses with an intensity FWHM of 100 ns that resonantly couple $|s\rangle$ to $|p\rangle$ and $|p\rangle$ to $|d\rangle$. In the calculation, the peak Rabi frequency of the lower transition is 3.5 MHz, as calculated from experimental Autler-Townes splitting data [87], and that of the upper transition is estimated to be 3 MHz. For a range of the dipole-dipole coupling strength, V_{dd}, of the channel in Eq. 6.1, 1 MHz$\leq V_{\mathrm{dd}} \leq$ 25 MHz, we solve the master equations and extract the fraction of atoms in the $|p'\rangle$ state 200 ns after excitation. The $|p'\rangle$-fraction, S_{A}, is given by the fraction of all Rydberg states

in the state p', or

$$S_{\mathrm{A}} = \frac{\rho_{p'f+fp'}}{2\rho_{p'f+fp'} + 2\rho_{dd} + \rho_{pd+dp} + \rho_{pd-dp} + \rho_{gd+dg} + \rho_{gd-dg}} \quad , \tag{6.4}$$

where ρ_a is short for the diagonal element $\rho_{a,a}$. The calculated values of S_{A} have a maximum within the above range of V_{dd}, which we show as squares in Fig. 6.2b as a function of n. We assume that $p'f$ pairs are preferentially excited for atoms with coupling strengths that maximize energy transfer according to Eq. 6.1. Using appropriate sets of different basis states, energy detunings, and coupling strengths, analogous results are also obtained for $nD_{3/2}$ and nS states (triangles and circles in Fig. 6.2b).

The model is quite successful in reproducing all qualitative features of Fig. 6.2a, but the experimental values of S_{A} are about 20 times larger than the theoretical values. Several factors may cause disagreement between the experimental and calculated values of S_{A}. We find that S_{A} is sensitive to several parameters which are not precisely known, including the upper-transition Rabi frequency and the energy detuning of the channel in Eq. 6.1. Additionally, in our calculations we neglect the magnetic substructure of the atoms. Most importantly, we neglect excitations involving more than two atoms by construction of our Hilbert space.

Work is currently being done with a collaborator, Thomas Pohl, which confirms that many-atom effects are indeed the dominant mechanism responsible for the surprisingly large amounts of state mixing observed when the channel in Eq. 6.1 is nearly resonant [95]. In general, the simplest way to account for many-body effects within one bubble is by solving for the interaction-induced level shifts as a sum over pairwise interactions among many atoms. This is the approach commonly taken in the literature [23, 28, 30], and we show that such an approach yields a significant improvement to the agreement between experiment and theory. At $n = 43$, the

theory underestimates S_{A} by a factor of 2 rather than a factor of ~ 20. However, in order to model our results fully, Thomas has solved the full many-body Hamiltonian of a scaled-down version of our entire extended system. The full multi-atom state basis includes many-body interactions to all orders, *i.e.* interactions that cannot be represented as a pure sum of binary potentials. Using this approach, the agreement between theory and experiment is excellent; for $43D_{5/2}$ the two values agree to within $5-10\%$. Thus, forthcoming work proves what is hinted at in these experiments; namely, that the collective effect of many-body interactions that arise from considering the full Hilbert space are responsible for the significant amount of instantaneous energy transfer according to Eq. 6.1 [95].

Other theoretical work in progress to be published by Paul Berman and Thomas Pohl accounts for the fact that one may observe strong state mixing into $|(n-2)F_{7/2}\rangle$ and $|(n+2)P_{3/2}\rangle$ states in a system where one may see a significant Rydberg excitation blockade. This is the apparently contradictory conclusion to which we are lead based on the discussion of Chapters IV, V, and VI. One would intuitively expect that the f and p' single atom states may be produced only if the $|N,2\rangle$ state is populated in a single bubble, a situation which seems to preclude the observation of a strong blockade. However, Berman and Pohl find that when the number of atoms in a bubble, N, becomes large there are a large number of accessible states that share two or more excitations. One state that contains significant $|p'f\rangle$ and $|fp'\rangle$ character may be populated during the excitation pulses, but this state is like a "dark" state in that it is not affected by the interaction channel in Eq. 6.1 after the optical pulses are off. Excitation to this state can lead to the creation of substantial numbers of $p'f$ atom pairs. While certain bubbles may be excited to this state, others are blockaded in the sense that only singly-excited collective states are populated. More

details may be found in the forthcoming manuscript. However, I wish emphasize the general point that elaborate theoretical analysis of systems of interacting Rydberg atoms, accounting for the full many-body nature of the interactions, reproduces our initially counterintuitive results and accounts for mixing into $p'f$ states in blockaded systems.

6.3 Time-delayed state mixing

In the results shown so far, the time between excitation and SSFI has been fixed at $\tau_{\rm FI} = 200$ ns, which is sufficiently short to ensure that the atoms remain fixed in space. In the following discussion, we explore time-delayed collisions, which may be triggered by the effect of interatomic forces on atomic motion [51, 55, 56]. State-mixing due to time-delayed collisions may be interpreted as the time-delayed creation of states $|N,2\rangle_{\pm}$. Two single atoms in d states created in adjacent bubbles may move together as a result of the attractive nature of the interaction potential. As the atoms move together, they become strongly coupled and form mixed quantum states $|N,2\rangle_{\pm}$. As the atoms get closer, the coupling matrix element, $V_{\rm dd} \propto 1/R^3$, grows and the atoms become more equal admixtures of $|dd\rangle$ and $\frac{1}{\sqrt{2}}\big\{|p'f\rangle + |fp'\rangle\big\}$. Therefore, the probability to measure a $p'f$ atom pair gets larger with interaction time, $\tau_{\rm FI}$. If, however, atoms are excited which interact via repulsive interactions, the atoms are not expected to move appreciably and they do not form mixed quantum states. Thus, for repulsive interactions the number of detected product state atom pairs will not change appreciably with interaction time, $\tau_{\rm FI}$.

In Fig. 6.4 I show the $S_{\rm A}$-fraction measured as a function of the time delay between excitation and detection for $41D_{5/2}$, $43D_{5/2}$, and $45D_{5/2}$ states. Within 200 ns of excitation, the $S_{\rm A}$-value measured for excitation to $43D_{5/2}$ reaches ≈ 0.18. This is

somewhat lower than the corresponding value in Fig. 6.2a, presumably because of experimental variations in atom density. As the time delay is increased, the S_A-value increases to a steady state of ≈ 0.24 within several μs. For excitation into $45D_{5/2}$, a qualitatively similar behavior is observed, with S_A-values being ≈ 0.03 lower than for excitation into $43D_{5/2}$. In contrast, for excitation into $41D_{5/2}$ states much lower S_A-values are measured, and S_A does not increase as a function of the excitation-probe delay time.

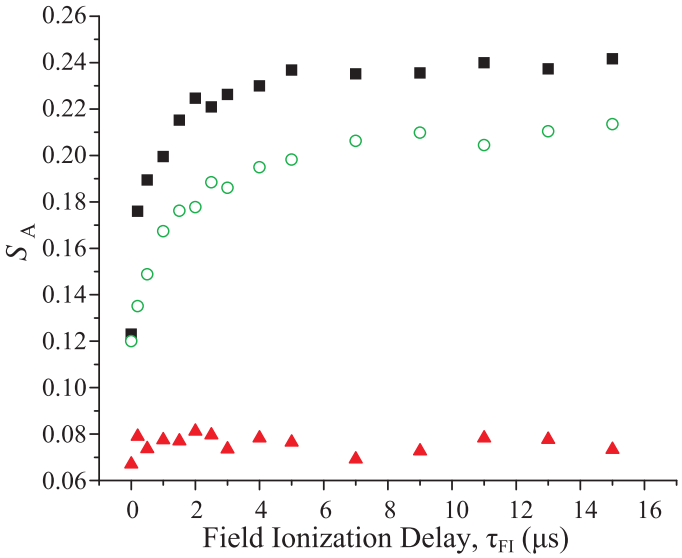

Figure 6.4: S_A as a function of the delay between excitation and field ionization, τ_{FI}, for excitation into $41D_{5/2}$ (triangles), $43D_{5/2}$ (squares), and $45D_{5/2}$ (circles) states.

The energy detuning of the channel in Eq. 6.1 is nearly zero for $n = 43$ and changes sign between 43 and 44 (see Table 6.4). This leads to enhanced attractive interaction for several n-states above $n = 43$ and repulsive interaction for several n-states below $n = 43$ (see Fig. 2.2). In the case of $45D_{5/2}$ in Fig. 6.4, in which the channel in Eq. 6.1 leads to a negative (attractive) interaction potential, the S_A-value rapidly increases with field ionization delay within a few μs. This increase is primarily due to additional state-mixing produced in time-delayed collisions triggered by attractive inter-atomic forces. In the case of $41D_{5/2}$, in which the interaction potential is weak

and repulsive, the S_A-value remains constant as a function of field ionization delay. This observation is consistent with the absence of additional state-mixing produced in time-delayed collisions; here atoms move very little relative to one another due to mutual repulsion. In the case $43D_{5/2}$ the detuning, Δ, is of the same order as the excitation bandwidth, leading to the creation of atom pairs on both attractive and repulsive molecular potentials. This may explain why the data for $43D_{5/2}$ exhibit both an almost instantaneous initial rise and a time-delayed, gradual increase in S_A.

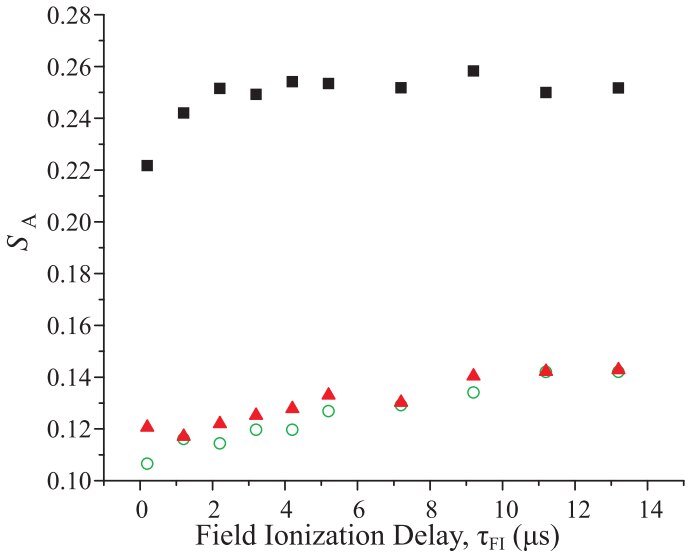

Figure 6.5: S_A as a function of the time delay between excitation and field ionization, τ_{FI}, for excitation into $43D_{3/2}$ (circles), $43D_{5/2}$ (squares), and $45S$ (triangles) states.

In Fig. 6.5 we show the value of S_A as a function of the field-ionization delay, τ_{FI}, for several different angular momentum states of approximately equal energy ($43D_{3/2}$, $43D_{5/2}$, and $45S$). One may note that there is little difference in the growth of S_A with interaction time, τ_{FI}, for $43D_{3/2}$, which interacts via attractive interactions and $45S_{1/2}$, which interacts via repulsive interactions. This is in contrast to the strong difference in the growth of S_A with τ_{FI} for the $45D_{5/2}$ (attractive) and $41D_{5/2}$ (repulsive) states, as seen in Fig. 6.4. We attribute this difference to the fact that the energy detuning of the dominant interaction channel for $43D_{3/2}$ states is more than

twice as large as that for $45D_{5/2}$ states and that the interaction energies, and hence attractive forces, are a factor of three smaller than for $45D_{5/2}$ (see Figs. 2.2 and 2.3). Thus, the rates of time delayed state-mixing may increase dramatically only if the interactions are strong and interact via a channel with small energy defect, such as for $45D_{5/2}$. The clearest feature of Fig. 6.5, however, is that for $43D_{5/2}$ states, the $S_{\rm A}$ value increases much more rapidly and reaches a much higher steady-state value than for the $43D_{3/2}$ and $45S$ states. We attribute this behavior to the fact that the $43D_{5/2}$ state interacts via a strong, near-resonant interaction (Eq. 6.1) while the other two states do not.

6.4 Collisions in an optical dipole trap

In addition to the experiments examining the state-mixing collisions of atoms in a MOT described above, we have performed similar measurements for atoms in an optical dipole trap. In this case, the ground-state atom density may be varied by varying the dipole trap time of flight, τ_2, before optical excitation. A detailed account of how comparisons between theoretical and experimental curves of $S_{\rm A}$ as a function of ground-state atom density for $43D_{5/2}$ states proves that many-body effects dominate the dynamics of our system is given in Ref. [95]. Here, we highlight two other aspects of the data taken using an optical dipole trap which relate to the discussion of time-delayed collisions above.

6.4.1 Time-delayed collisions as a function of n^*

Figure 6.4 and the accompanying discussion provides evidence for the enhancement of the number of time-delayed state-mixing collisions when the interactions between Rydberg atoms are strong and attractive, such as for $45D_{5/2}$ states. It also provides evidence that such collisions are strongly suppressed when interactions are

weak and repulsive, such as for $41D_{5/2}$. Both the change in sign and strength of the potential over a small range of n centered about $n = 43$ may be seen in Fig. 2.2 and are due to the change in sign of Δ for the channel in Eq. 6.1 (see Table 6.1).

We may more directly measure the enhancement or suppression of time-delayed collisions in the vicinity of $n = 43$ due to the near-resonance of the channel in Eq. 6.1 by examining the fraction $S_{\rm A}$ as a function of n^* for a long interaction time, $\tau_{\rm FI}$. In Fig. 6.6, I show $S_{\rm A}$ as a function of n^* for several $nD_{3/2}$, $nD_{5/2}$, and $nS_{1/2}$ states near $n = 43$. The data was taken with $\tau_2 = 25$ μs, corresponding to a peak ground-state atom density of 2×10^{11} cm^{-3}. The atoms were given $\tau_{\rm FI} = 10.1$ μs to interact before their state distribution was probed using SSFI.

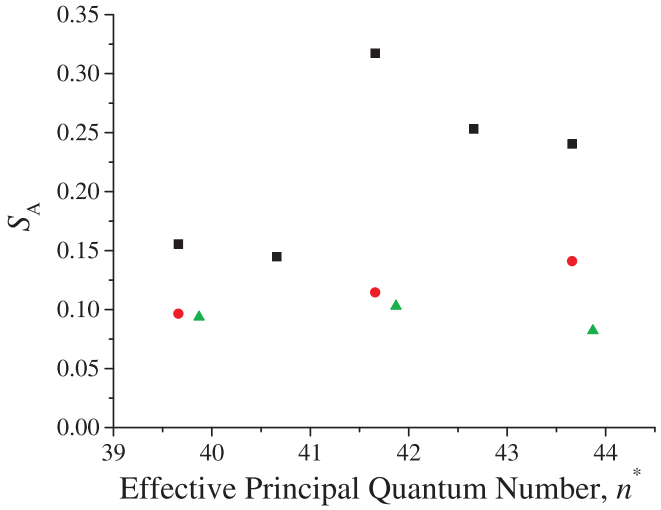

Figure 6.6: $S_{\rm A}$ as a function of the effective principal quantum number of the states into which the atoms are excited for an interaction time $\tau_2 = 10.1$ μs. Results are shown for $D_{5/2}$ (squares), $D_{3/2}$ (triangles), and S (circles) states.

We immediately see that the magnitude of $S_{\rm A}$ is modulated with n in a way that follows the dispersive-shaped interaction resonance near $n = 43$ for $nD_{5/2}$ states, as seen in Fig. 2.2. When the interactions are repulsive ($n = 41$ and 42) the amount of time-delayed state mixing is significantly lower than when the interactions are attractive and enhanced by the small energy detuning of the interaction channel

($n = 44$ and 45). As before, we see the strongest state mixing for $43D_{5/2}$. Since Δ is very small, time-delayed state mixing collisions are significant even though the interactions are repulsive. For $nD_{3/2}$ and $nS_{1/2}$ states, the values of $S_{\rm A}$ are small and show little variation with n owing to the absence of any near-resonant interaction channel in this vicinity.

6.4.2 Penning-ionizing collisions

The resonance of the interaction channel in Eq. 6.1 at $n = 43$ affects not only the state-mixing dynamics of $nD_{5/2}$ Rydberg atoms, but also Penning ionization. Penning ionization, illustrated schematically in Fig. 6.7, is a process very similar to energy transfer in resonant state-mixing collisions except that, in order to conserve energy in a collision, one collision partner is promoted to an energy state above the ionization threshold. To investigate ionization, we excite Rydberg atoms with 500 ns laser pulses (we have found that longer excitation pulses lead to clearer ionization signatures) and measure the number of free electrons generated when atoms are allowed a time $\tau_{\rm FI}$ to interact before SSFI. In our data, free electrons produce a peak at the onset of the SSFI pulse, as shown in Fig. 6.8. Rydberg states are excited from atoms in an optical dipole trap with peak density 7×10^{10} cm^{-3} and diameter 35 μm, produced by allowing the dipole trap $\tau_2 = 25$ ms to expand before the optical excitation pulses are applied.

To quantify ionization, I define the Penning-ionization probability, $S_{\rm FE}$, as the integral of the free-electron peak divided by the total integral of the electron signal. Figure 6.9a shows $S_{\rm FE}$ as a function of the interaction time, $\tau_{\rm FI}$, and shows that $S_{\rm FE}$ approaches a steady-state after a few tens of μs of evolution. In Fig. 6.9b I show $S_{\rm FE}$ for $nD_{5/2}$ states after 15.1 μs interaction time as a function of n. $S_{\rm FE}$ is approximately constant at ~ 0.10, except for a drop in the range $n = 41 - 43$ and a moderate

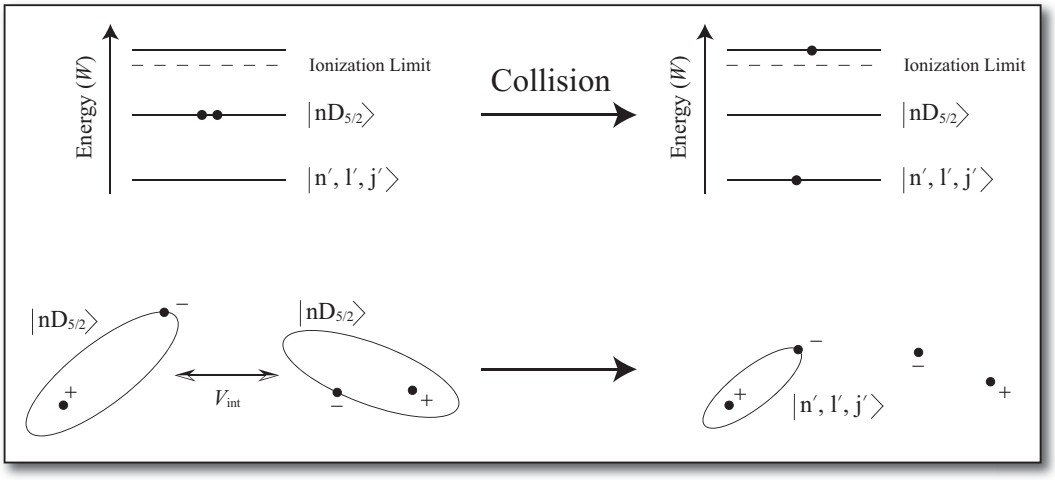

Figure 6.7: Schematic illustration of a Penning-ionizing collision. The collisional energy-transfer process is similar to the case of state-mixing described above except that one of the product states lies above the ionization threshold.

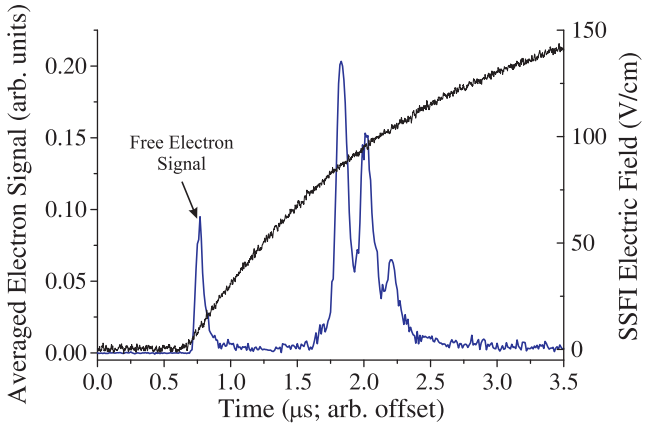

Figure 6.8: Averaged SSFI electron signal for the $44D_{3/2}$ Rydberg state (blue curve; left axis), plotted along with the field ionization electric field pulse (black curve; right axis). The delay between excitation and ionization is $\tau_{\mathrm{FI}} = 15.1\ \mu$s. The free electron signal produced from Penning-ionizing collisions is indicated.

elevation at $n = 40$. We attribute the drop in the range $n = 41 - 43$ to a reduction in collisions due to the repulsive interactions between Rydberg atoms expected in that range of n (see Fig. 2.2). While the elevation at $n = 40$ is not fully understood, we note that, following Fig. 2.2, Rb atoms in the $40D_{5/2}$ state exhibit relatively weak interaction due to an accidental cancelation of the level-shift contributions associated with the two dominant interaction channels, those in Eqs. 2.13 and 2.14. The weak interaction at $n = 40$ is expected to weaken the Rydberg excitation blockade and to lead to a relatively large fraction of Rydberg-atom pairs at close distances, which may cause enhanced ionization. Overall, the interaction channel in Eq. 6.1 plays a significantly smaller role in Penning ionization than it does in the near-resonant state-mixing collisions discussed earlier. This may be because Penning ionization is a deep, inelastic process, which should depend less on a single, near-elastic interaction channel than the state-mixing collisions studied in this thesis.

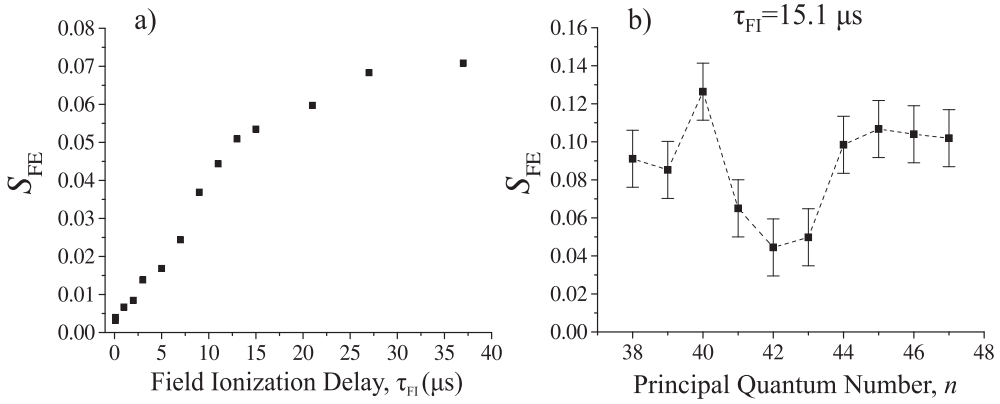

Figure 6.9: a) Penning-ionization probability S_{FE} for $43D_{5/2}$ as a function of field ionization delay time, τ_{FI}. b) S_{FE} for $nD_{5/2}$ states as a function of n for $\tau_{\mathrm{FI}} = 15.1$ μs.

CHAPTER VII

Conclusion and outlook

The work described in this thesis represents a broad investigation of Rydberg-Rydberg interactions and their experimental manifestations. I have discussed a detailed calculation of two-body Rydberg-Rydberg interaction energies for a wide range of quantum states, atom-atom orientations, and applied electric fields. Although the assumption that Rydberg atoms interact predominantly via two-body interactions is not always valid, our calculations provide a framework within which one may understand a wide variety of experimentally observed phenomena, including Rydberg excitation blockades and state-changing and ionizing collisions. I have described a technique to measure the effectiveness of a Rydberg excitation blockade using the counting statistics of the number of excited atoms, and shown a significant narrowing of the counting distributions when Rydberg-Rydberg interactions are strong. Using an optical dipole trap, we have observed significantly sub-Poissonian counting statistics, in agreement with theoretical predictions. I have also described an experiment that provides the first direct, spectroscopic proof that the blockade mechanism is operative in systems of interacting Rydberg atoms. We have spectroscopically measured the energy shift of the collective states $|N, 2\rangle$ for several quantum states and values of an applied electric field. Finally, we have investigated the relative probabilities for

state-changing and Penning-ionizing collisions as a function of n in the vicinity of an electric field-free interaction resonance. The results provide evidence for the strong variation in magnitude and sign of Rydberg-Rydberg interaction potentials in the vicinity of one such resonance and for the importance of accounting for many-body interactions when theoretically describing a system of interacting Rydberg atoms.

While we have studied the properties and manifestations of Rydberg-Rydberg interactions from a variety of angles, much work remains to be done in pursuit of our closely-related goals of both understanding Rydberg atom interactions and developing a neutral-atom quantum phase gate. In the remainder of this chapter, I highlight some of the work which is planned for the near-future. I first describe data we have already obtained related to collisions between $nS_{1/2}$ Rydberg atoms. The data is not totally understood but suggests that further investigation may reveal interesting physics. Additionally, I will describe some planned experiments that extend the work described here, improve our understanding of Rydberg-Rydberg interactions, and move us towards the implementation of a neutral-atom quantum gate.

7.1 Collisions between $nS_{1/2}$ atoms

In Chapter VI it was apparent that when Rydberg atoms interact via time-delayed state-changing collisions, the number of collision products produced is a strong function of the nature of the involved interatomic forces (*i.e.* attractive or repulsive). The results presented in that Chapter VI suggest that when the interactions are attractive, the number of collision products increases with interaction time, but when the interactions are repulsive, the number of collision products remains relatively constant with interaction time or increases only slightly. One case that was not

discussed at length, however, is collisions between $S_{1/2}$ states, which always interact via repulsive interactions (see Fig. 2.4). Surprisingly, we have found that for high ground-state atom densities the number of product states produced *decreases* with interaction time, τ_{FI}.

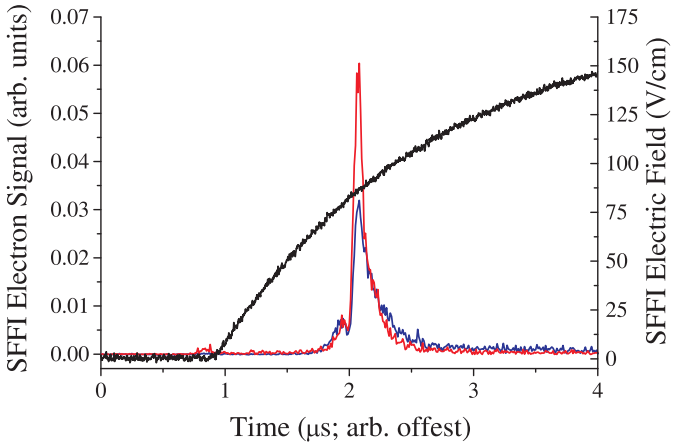

Figure 7.1: SSFI electron spectra for excitation into the $49S_{1/2}$ state for $\tau_{\mathrm{FI}} = 100$ ns (blue) and 20.1 μs (red) along with SSFI electric field pulse.

This result may be easily seen in Fig. 7.1, a plot of the SSFI electron spectrum for excitation into $49S_{1/2}$ states for $\tau_{\mathrm{FI}} = 100$ ns and $\tau_{\mathrm{FI}} = 20.1$ μs from a dipole trap with ground-state atom density of 4×10^{11} cm^{-3}. Each spectrum has been scaled by an appropriate factor to make their total integrals equal. One may see that for $\tau_{\mathrm{FI}} = 100$ ns, the wings of the SSFI spectrum are broader and the central peak shorter than for $\tau_{\mathrm{FI}} = 20.1$ μs. As interaction time increases, the spectra transition from short and broad to narrow and tall. This indicates that there are more collision products for short interaction times than for long interaction times. Therefore, it seems that state-mixing probability decreases with interaction time, contrary to all other cases studied. If, however, the density is lowered to 1×10^{10} cm^{-3}, this phenomenon disappears and we see little change in the SSFI spectra with τ_{FI}.

While this phenomenon is not yet fully understood, we have taken spectra similar

to those displayed in Fig. 7.1 for a range of SSFI ramp speeds. We have seen that, as the ramp speed is increased, the difference between the spectra for $\tau_{\mathrm{FI}} = 100$ ns and $\tau_{\mathrm{FI}} = 20.1$ μs disappears. Thus, we suspect that the broadening of the SSFI spectra for high density and short interaction time, τ_{FI}, is related to the detailed nature in which the $nS_{1/2}$ states are field-ionized. A recent paper has investigated the effect of the SSFI ramp speed on product state mixing for interaction channels near a Förster resonance [96]. Since the dominant interaction channels for $S_{1/2}$ states have infinite-separation energy detunings of order several GHz, there is no Förster resonance and the application of an electric field tunes these channels further from resonance. Therefore, we suspect that we are seeing a different effect of atomic interactions during the SSFI electric field ramp that is apparent only at high ground-state atom densities and does not depend on a Förster resonance. Further investigation will be required to fully understand this process and its implications for the use of state-selective field ionization as a tool to investigate collisional physics.

7.2 Future Plans

Most experiments planned for the near future are designed to help us better understand the properties of the coherent many-body quantum states $|N, k\rangle$ and to realize systems that may be useful in implementing a neutral atom quantum phase gate. In pursuit of the former goal, experiments will be performed in which the validity of the "bubble" picture of an excitation blockade in an extended atomic ensemble is tested. This is important since we rely on the bubble picture to describe many experimental results in systems of interacting Rydberg atoms. Additionally I will describe an improved version of the double-resonance spectroscopy measurement described in Chapter V that will provide us with more direct information about

the nature of the energy shifted states, $|N, 2\rangle$. Experiments are also planned that utilize two close, parallel optical dipole traps to provide information about the nature of Rydberg-Rydberg interactions and move our experimental system towards a configuration in which a quantum phase gate may be realized.

7.2.1 Testing the "bubble" picture

In the discussion of experiments on Rydberg excitation blockades in extended atomic ensembles I have relied heavily on the "bubble" picture. I have emphasized that the bubbles are not real, they are merely a heuristic construction that reflects the following fact. If we perform a quantum measurement where we project all many-body entangled states $|N, 1\rangle$ in different regions of the excitation volume onto individual atoms and measure these positions in a spatially sensitive way, the pair correlation function will be zero for some volume around each detected excitation. In other words, there is an anticorrelation in the measured positions of Rydberg excitations when they are projected onto individual atoms. While our apparatus is currently not capable of detecting Rydberg atoms in a spatially-sensitive way, an experiment is being constructed that is.

Spatial sensitivity is achieved in this experiment through a novel state-selective field ionization electrode geometry in which a MOT is created just above a conducting tip, as shown in Fig. 7.2. In the experiment, the lower transition light will be collimated and much larger than the MOT, as shown in the upper panel of Fig. 3.7. The upper transition light will be focused in one dimension using a cylindrical lens in order to create a sheet of light with thickness on the order of the diameter of one bubble (or the anticorrelation length expected for detected Rydberg excitations [28]). Thus, Rydberg excitations will be created roughly in a plane. After excitation, a high voltage SSFI pulse will be applied to the conducting tip, creating a purely radial

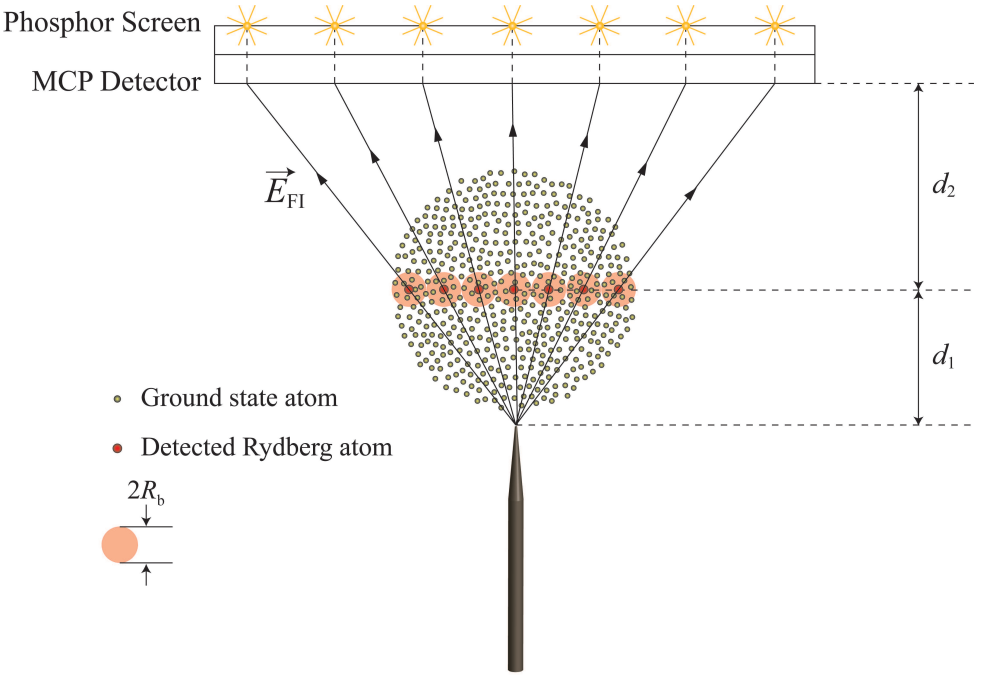

Figure 7.2: Illustration of a novel state-selective field ionization geometry that will allow spatially sensitive detection of Rydberg excitations. A high voltage pulse is applied to a sharp conducting tip placed in the vicinity of the MOT. Rydberg atoms are ionized and, if all stray fields are well compensated, the ions follow paths parallel to the divergent electric field of the tip.

electric field. All magnetic and stray electric fields will be carefully compensated in order to ensure that this is the case. Rydberg atoms will be ionized and the ions will follow trajectories parallel to the radial electric field and will impinge on an MCP.[1] Thus, we map the two-dimensional distribution of Rydberg atoms onto the surface of the MCP with a large magnification factor, M, given by $M = \frac{d_1+d_2}{d_1}$, where d_1 and d_2 are defined in Fig. 7.2. Figure 7.2 is not drawn to scale and in the experiment M will be of order ~ 500. Thus, atoms separated by $2R_{\mathrm{b}} \sim 10$ μm in the MOT will produce signals separated by millimeters on the MCP front face. The pair correlation function of atoms on the MCP face can then be calculated by analyzing images obtained from the phosphor screen attached to the MCP. In this way, we can observe the spatial anticorrelation in the detected Rydberg atoms and verify the validity of the "bubble"

[1] In this case we detect ions rather than electrons on the MCP, but SSFI works the same for either type of detection.

picture.

7.2.2 Improvement to the double-resonance spectroscopy experiment

A separate experiment is being implemented that seeks to improve on the technique described in Chapter V for the double-resonance spectroscopy of the many body states $|N, k\rangle$ in a system of interacting Rydberg atoms. As pointed out in Sect. 5.6, the interpretation of the spectra obtained when both pairs of excitation pulses are enabled, $\tilde{S}_{1+2}(\nu_2)$, is complicated by the fact that the pulse pairs are separated in time by 400 ns. We will perform an experiment similar to the one described in Chapter V, but in which only one lower-transition excitation pulse is applied and the upper-transition pulse has two frequency components. The frequency of one component will be fixed and the frequency of the other will be scanned. In other words, we bring the "first pulses" and "second pulses" in Fig. 5.2 to the same instant of time. This will be accomplished by using two independently scannable RF sources. The frequency modulation input of one source will be scanned relative to the other and the two RF signals will be added with an RF combiner. The resulting signal will then be sent to an AOM and the first upshifted order will contain two beams with slight relative displacement and slightly different frequencies. The slightly displaced beams will then be coupled into the same optical fiber, producing an optical beam at the fiber output with two frequency components in spatial mode.

Although this experiment will present some new experimental challenges, it will be complicated less by the problems associated with the experiment described in Chapter V. These problems include decay between the first and second pulses, unwanted coherent depopulation of the state $|N, 1\rangle$ with the second pulses, and unwanted excitation of bubbles in the $|N, 0\rangle$ state by the second pulses. In the new experiment, any excitation to states $|N, 2\rangle$ will be a single two-photon transition at one instant

of time, not two one-photon transitions at separate times. As long as the number of Rydberg excitations created on the $|N,0\rangle \rightarrow |N,1\rangle$ transition have saturated with upper-transition laser intensity, we should observe no extra counts in $\tilde{S}_{1+2}(\nu_2)$ when $\nu_2 = \nu_1$. That is, we should directly measure spectra like those in Figs. 5.4 and 5.6c and d, without doing any subtraction of spurious excitations.

7.2.3 Experiments with parallel dipole traps

All of the experiments we have done and plan to do have been steps towards the long-term goal of this project: the implementation of a neutral-atom quantum phase gate. The scheme for implementing a phase gate is detailed in Sect. 1.1.1. The gate requires the ability to independently address two atoms [20] or two distinct ensembles of atoms [2] that are separated by less than the bubble radius for the chosen experimental conditions. It has been proposed that trapping atoms in an optical lattice and addressing individual lattice sites with Rydberg excitation lasers is a viable route to the implementation of a phase gate [20]. There has been recent progress towards constructing these systems which may hold promise for large-scale quantum computers [45]. However, the first realization of a neutral atom quantum gate will most likely be in a simpler system, such as two parallel dipole traps. Thus, we plan to implement a double-dipole trap in our system in order to move towards the implementation of a prototype of a quantum gate. Such a geometry is depicted in Fig. 7.3 and could be realized by placing a nonlinear optical element in the dipole-trap beam path to create a small angular divergence between two polarization components before the light is focused through the MOT.

Once two optical dipole traps are constructed with a separation d_{12} smaller than R_{b}, several experiments would naturally follow. One would begin by demonstrating single-trap addressability using tightly focused lower- and upper-transition beams.

One could then use this system to perform a variant of the double-resonance spectroscopy experiment described in Chapter V. A single Rydberg excitation could be created in trap 1 and the atoms in the trap 2 could be excited with a pulse pair having a scannable frequency. In this way, we may record the energy shift of the state $|N, 2\rangle$ as the separation of the two traps is varied in order to spectroscopically measure the distance-dependent interaction potentials between atoms in the two traps. As long as the spatial dimensions of the atom clouds are $\ll R_{\rm b}$, such a measurement would approximately yield the true two-body interaction potentials for two interacting Rydberg atoms.

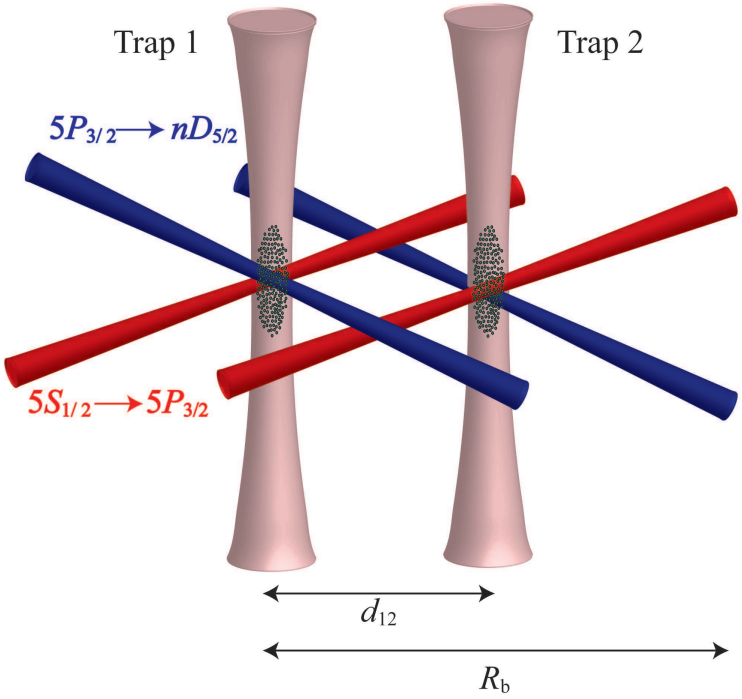

Figure 7.3: Two parallel optical dipole traps separated by a variable distance d_{12}. Each trap may be individually addressed by two pairs of optical beams. Such a geometry could be used to probe the interaction potentials as a function of d_{12} or to realize a prototype of the quantum phase gate described in Sect. 1.1.1. The magnitude of the bubble radius, $R_{\rm b}$ is indicated.

In addition to performing double-resonance spectroscopic measurements, one may measure the effectiveness of a Rydberg excitation blockade in a system with one average excitation. This may be done by measuring the counting statistics of the

number of excited atoms when addressing only one trap with beams that define an excitation volume $\lesssim$ the bubble volume.[2] Alternatively, one could excite an atom in one trap to a Rydberg state and show that excitation in the other trap is blockaded. In other words, we may apply excitation pulses to trap 1, wait a short time, and then apply the same pulses to trap 2. If $d_{12} < R_{\mathrm{b}}$, atoms in trap 1 will be excited but excitation of trap 2 will be inhibited. The number of Rydberg excitations detected will be between 0 and 1 on average, depending on the excitation efficiency. If $d_{12} > R_{\mathrm{b}}$, however, one would detect twice as many excitations on average since both traps may be excited. If the ability is demonstrated to measurably inhibit excitation in trap 2 due to a Rydberg excitation in trap 1, experimental implementation of a quantum phase gate would be within reach.

[2]This could actually be demonstrated using one optical dipole trap.

APPENDICES

APPENDIX A

Eiegenstates and energies for binary interaction via one interaction channel

For the discussion that follows, I consider two atoms separated by a fixed distance and interacting via only the near-resonant interaction channel

$$2 \times nD_{5/2} \rightarrow (n-2)F_{7/2} + (n+2)P_{3/2} \quad . \tag{A.1}$$

I show that changing the infinite separation energy defect of this channel, $\Delta = W_{|(n-2)F_{7/2}\rangle} + W_{|(n+2)P_{3/2}\rangle} - 2 \times W_{|nD_{5/2}\rangle}$, changes the nature of the doubly-excited states $|N = 2, k = 2\rangle$. Specifically, I examine the transition from van der Waals interactions where one state $|N = 2, k = 2\rangle$ may be excited to dipole-dipole interactions where two $|N = 2, k = 2\rangle$ states may be excited that are symmetrically split about the interaction-free energy. The energy defect may be tuned by applying an electric field (such as described in Sect. 2.3.1 and implemented in Chapters IV and V) or by changing the n value of the state into which one is exciting the atoms (such as in Chapter VI).

The energy level diagram of the problem is shown in Fig. A.1 and the Hamiltonian matrix is

$$H = \begin{bmatrix} 0 & V & V \\ V & \Delta & 0 \\ V & 0 & \Delta \end{bmatrix},$$

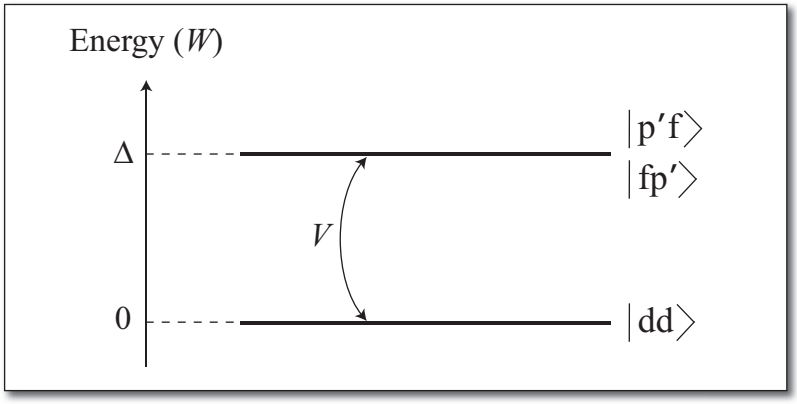

Figure A.1: Energy level diagram relevant to the discussion of this section. I assume that the energy of $|dd\rangle$ is zero for simplicity.

where the three columns are associated with the two-atom basis states $|dd\rangle$, $|p'f\rangle$, and $|fp'\rangle$, respectively. The single-atom states $|d\rangle, |p'\rangle$, and $|f\rangle$ correspond to the $|nD_{5/2}\rangle$, $|(n+2)P_{3/2}\rangle$, and $|(n-2)F_{7/2}\rangle$ states and the coupling matrix elements (see Eq. 2.2) are denoted as V ($V = 0.36n^{*4}/R^3$). Diagonalizing this Hamiltonian yields three eigenstates, $|N=2,k=2\rangle_{\rm o}$ and $|N=2,k=2\rangle_{\pm}$, with energies

$$W_{\rm o} = \Delta \tag{A.2}$$

$$W_{\pm} = \frac{\Delta}{2} \pm \sqrt{2V^2 + \left(\frac{\Delta}{2}\right)^2} \quad . \tag{A.3}$$

The eigenstates expressed in the original $|dd\rangle$, $|p'f\rangle$, and $|fp'\rangle$ basis are

$$|N=2,k=2\rangle_{\rm o} = \frac{1}{\sqrt{2}}\big\{|p'f\rangle - |fp'\rangle\big\} \tag{A.4}$$

$$|N=2,k=2\rangle_{\pm} = \alpha_{\pm}|dd\rangle \pm \beta_{\pm}\frac{1}{\sqrt{2}}\big\{|p'f\rangle + |fp'\rangle\big\} \tag{A.5}$$

where

$$\alpha_{\pm} = \frac{W_{\mp}}{\sqrt{2V^2 + |W_{\mp}|^2}} \tag{A.6}$$

$$\beta_{\pm} = \frac{\sqrt{2V^2}}{\sqrt{2V^2 + |W_{\mp}|^2}} \quad . \tag{A.7}$$

I first assume that it is possible to excite the state $|N=2,k=2\rangle$. Since $nD_{5/2}$ Rydberg states may only be created from the $5P_{3/2}$ level (which I will call $|p\rangle$), the

states $|N=2,k=2\rangle$ are optically excited via matrix elements of the type

$$\frac{1}{\sqrt{2}}\big\{\langle pd|\mu_1\cdot\mathbf{E}_{\rm laser}|N=2,k=2\rangle+\langle dp|\mu_2\cdot\mathbf{E}_{\rm laser}|N=2,k=2\rangle\big\} \tag{A.8}$$

where μ_i is the atomic dipole moment operator for atom i and $\mathbf{E}_{\rm laser}$ is the $5P_{3/2}\rightarrow nD_{5/2}$ laser field. Since atoms 1 and 2 are identical, Eq. A.8 reduces to

$$\sqrt{2}\langle pd|\mu_1\cdot\mathbf{E}_{\rm laser}|N=2,k=2\rangle \quad . \tag{A.9}$$

We now see that the state $|N=2,k=2\rangle_{\rm o}$ cannot be excited because the single-atom matrix elements $\langle p|\mu_1\cdot\mathbf{E}_{\rm laser}|p'\rangle$ and $\langle p|\mu_1\cdot\mathbf{E}_{\rm laser}|f\rangle$ are zero owing to selection rules. The fact that these matrix elements are zero also implies that the $|N=2,k=2\rangle_{\pm}$ states may be excited only through matrix elements with the $|dd\rangle$ part of the wavefunction. That is, the matrix element in Eq. A.9 is:

$$\sqrt{2}\langle pd|\mu_{\mathbf{1}}\cdot\mathbf{E}_{\rm laser}|N=2,k=2\rangle_{\pm}=\alpha_{\pm}\big\{\sqrt{2}\langle pd|\mu_{\mathbf{1}}\cdot\mathbf{E}_{\rm laser}|dd\rangle\big\} \tag{A.10}$$

and the probability to excite the states $|N=2,k=2\rangle_{\pm}$ is proportional to $|\alpha_{\pm}|^2$.

In Fig. A.2a and b I plot $|\alpha_{\pm}|^2$ and $W_{\pm}$ as a function of Δ, assuming that the separation of the two atoms gives rise to a coupling matrix element $V=20$ MHz. That is, I assume the two atoms are separated by less than the bubble radius but more than the average ground-state atom separation for all cases of interest in Chapters IV, V, and VI. Figure A.2a shows that for $\Delta=0$, $|\alpha_{\pm}|^2=\frac{1}{2}$. By conservation of probability $|\beta_{\pm}|^2=\frac{1}{2}$ as well. Therefore, the states $|N=2,k=2\rangle_{\pm}$ are both equal admixtures of $|dd\rangle$ and $\frac{1}{\sqrt{2}}\big\{|p'f\rangle+|fp'\rangle\big\}$. Since $|\alpha_+|^2=|\alpha_-|^2$; that is, since $|N=2,k=2\rangle_+$ and $|N=2,k=2\rangle_-$ have equal $|dd\rangle$ character, both states may be excited with equal probability. An alternative way to view this situation is that the state $|dd\rangle$ is created immediately after excitation and, since $\Delta=0$, $|dd\rangle=\frac{1}{\sqrt{2}}\big\{|N=2,k=2\rangle_+ + |N=2,k=2\rangle_-\big\}$. Therefore, the probability to be in

$|N = 2, k = 2\rangle_+$ and $|N = 2, k = 2\rangle_-$ after a phase-insensitive quantum measurement is equal. Figure A.2b shows that for $\Delta = 0$, $W_+ = -W_-$ and the energy levels are symmetrically split about $W = 0$, or the noninteracting energy of a $|dd\rangle$ pair. $W_+ = -W_- = 28.3$ MHz which is equal to $\sqrt{2} \times V = \sqrt{2} \times 20$ MHz, in agreement with Eq. 2.7.

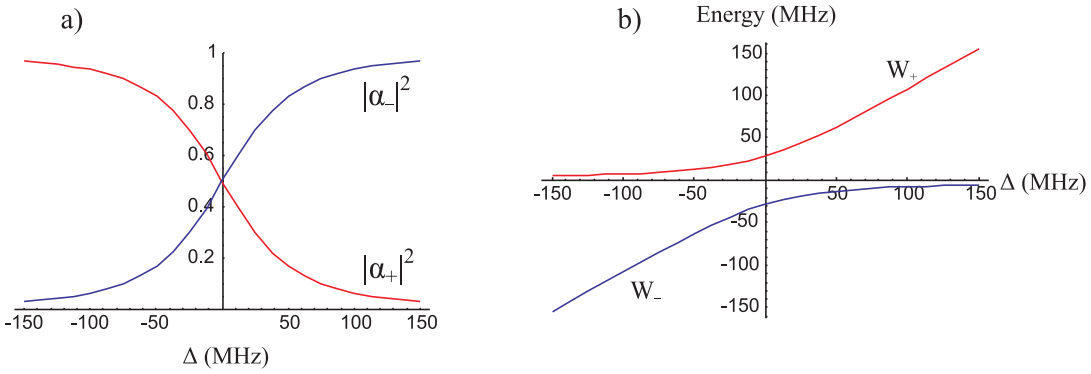

Figure A.2: $|\alpha_\pm|^2$ (a) and $W_\pm$ (b) as a function of Δ for $V = 20$ MHz.

As Δ becomes large and positive, however, $|\alpha_+|^2 \to 0$ and $|\alpha_-|^2 \to 1$. Therefore, for large energy detuning ($\Delta \gg V$) we may only excite one state, $|N = 2, k = 2\rangle_-$. Figure A.2b shows that W_+ becomes very large as Δ grows but, since the state $|N = 2, k = 2\rangle_+$ is unexcitable, this state has no experimental importance. However, we also see that as Δ grows, the energy W_- becomes smaller and monotonically approaches zero from below as $\Delta \to \infty$, as expected. The situation is the same if Δ is negative and its magnitude is large, but the roles of $|N = 2, k = 2\rangle_-$ and $|N = 2, k = 2\rangle_+$ are reversed. Here we can only excite $|N = 2, k = 2\rangle_+$ and its energy shift approaches zero from above as $\Delta \to -\infty$. In general, if we increase magnitude of the energy defect of the channel in Eq. A.1 from zero using an applied electric field or by changing n, we transition from being able to excite two symmetrically split states with equal probability to being able to excite only one state, with a smaller energy shift.

In addition to affecting the number and nature of the collective states that may be excited, changes in Δ will affect the probability to measure certain single-atom states when SSFI is used to project the states $|N = 2, k = 2\rangle$ onto the single-atom basis d, p', f. For $\Delta = 0$, when the states are equal admixtures of $|dd\rangle$ and $\frac{1}{\sqrt{2}}\{|p'f\rangle + |fp'\rangle\}$, SSFI measurements will yield equal numbers of dd and $p'f$ atom pairs. However, when Δ is large and the only excitable state has mainly $|dd\rangle$-character, we expect to measure very few $p'f$ atom pairs using SSFI.

While the present discussion has focused on the easily tractable case of $N = 2$ particles, we may extend the qualitative notions developed here to systems with $N > 2$. For $k = 2$ excitations shared by $N > 2$ atoms, the dimension of the Hilbert space is $\frac{3}{2}N(N-1)$. Therefore, a detailed examination of the exact solutions to the problem become difficult. However, for $N > 2$ we will still find that we can excite two *bands* of states which are symmetrically split about $W = 0$ for $\Delta = 0$ and that we can excite only one *band* of states which has significant $|dd\rangle$ character and little $|p'f\rangle$ character when Δ is large. The discrete levels become bands of levels because the two excitations will now be shared by many pairs of atoms, all separated by different distances and having different values of $V \sim n^{*4}/R^3$.

APPENDIX B

Feedback scheme for intensity stabilization in the double-resonance spectroscopy experiment

In all of the experiments described in this thesis, optical pulses are generated from narrowband continuous wave (cw) laser beams by amplitude modulation (AM) of an acousto-optic modulator or a combination of both amplitude and frequency modulation (FM). However, the experiment on double-resonance spectroscopy of interacting Rydberg atom systems, described in Chapter V, is the only experiment for which the FM capability of the AOM is used as a spectroscopic tool. In this experiment we set the frequency of the $5P_{3/2} \rightarrow nD_{5/2}$ laser so that the first upshifted order through the AOM is exactly on resonance with the $|N,0\rangle \rightarrow |N,1\rangle$ transition when the frequency ν_1 is applied to the FM input of the AOM. Amplitude modulation is used to create a pulse at frequency ν_1 out of the cw beam; I denote this pulse as "upper transition pulse 1." The frequency of the second upper transition pulse, ν_2, is then scanned in 4 MHz steps by changing the FM input to the AOM. This has the unavoidable side-effect of changing the angle of the first upshifted order after the AOM. The optical system is aligned so that the upper transition light pulses are coupled into an optical fiber most efficiently when the FM input of the AOM is at a frequency ν_1. Thus, as ν_2 is scanned, the angle of the upshifted order changes, and the light becomes less efficiently coupled into the optical fiber. The intensity

of the second optical pulse at the fiber output decreases as $|\nu_2 - \nu_1|$ grows and the amplitudes of the two optical pulses that are incident on the atoms are consequently unequal.

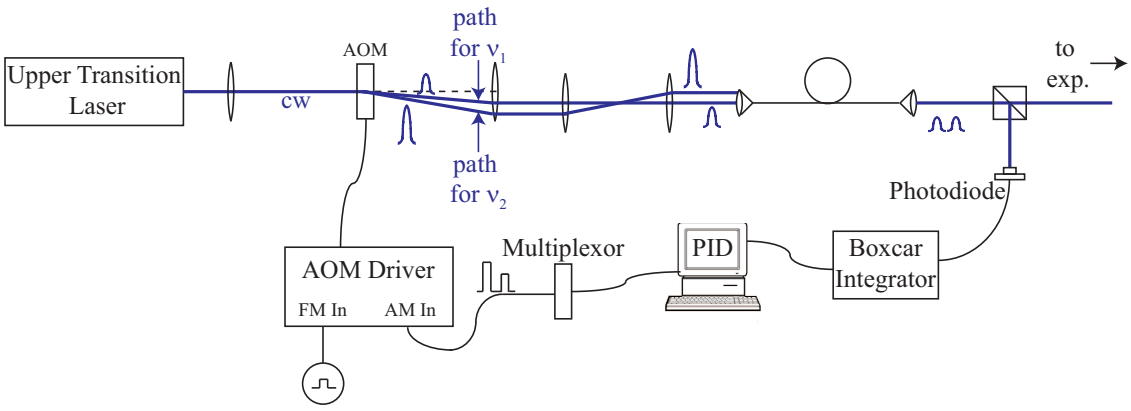

Figure B.1: Schematic illustration of the feedback scheme used to produce pulses with different frequencies, ν_1 and ν_2, at the output of the optical fiber. For clarity, the laser beam is drawn as a line rather than a beam with a waist that varies as it passes through various optical elements.

The physical properties of our experimental setup that lead to this problem, as well as our solution to the problem are sketched in Fig. B.1. We solve the problem by actively controlling the amplitude of the second pulse in a feedback scheme that utilizes the amplitude modulation capability of the AOM. The pulse timing diagram relevant to our scheme is shown in Fig. 5.2b and I reproduce its essential features in Fig. B.2 for convenience.

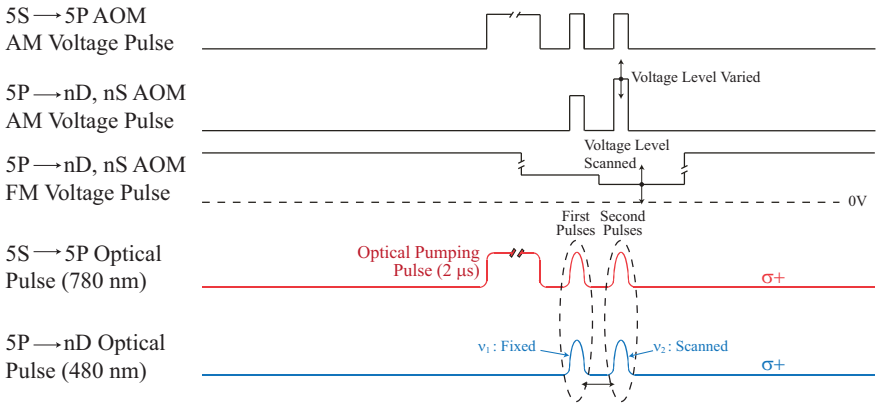

Figure B.2: Timing diagram for the electrical and optical signals relevant to the intensity stabilization scheme described in this appendix.

Our scheme proceeds as follows. We monitor the height of the each of the two pulses after the fiber output using a photodiode. The output of the photodiode is sent to a gated boxcar integrator which integrates the area of pulse 2 and this integral is read by a computer. The value of the integral is the input for a PID feedback algorithm that we implement using LabView. The PID algorithm compares the value of the integral read from the boxcar integrator with the value of a pre-programmed integral ($\approx$ the integral of pulse 1) and calculates an adjusted voltage to be sent to the AM input of the AOM driver (through a multiplexor). In other words, if the second optical pulse is smaller (larger) than the first at the fiber output, a larger (smaller) AM voltage is sent to the AOM driver for the second pulse and we repeat the process a fixed number of times that was chosen to ensure the two pulses will have the same area. When the two areas are approximately equal, we record the value of the AM voltage which is generated by the PID program. Thus, each frequency ν_2 is associated with a different AM voltage for pulse 2 which gives optical pulses 1 and 2 that have equal area at the fiber output. This list of AM voltages as a function of ν_2 can then be used to create two pulses with different frequency but equal amplitude at the fiber output as ν_2 changes.

To summarize: as ν_2 is scanned, the beam's upshifted order through the AOM changes position and we compensate the loss of fiber-coupling efficiency with higher light intensity for the second pulse at the fiber input.

BIBLIOGRAPHY

BIBLIOGRAPHY

[1] C. J. Lorenzen and K. Niemax. *Phys Scr.*, 27:300, 1983.

[2] M. D. Lukin, M. Fleischhauer, R. Cote, L. M. Duan, D. Jaksch, J. I. Cirac, and P. Zoller. Dipole blockade and quantum information processing in mesoscopic atomic ensembles. *Phys. Rev. Lett.*, 87(3):037901, June 2001.

[3] Thomas F. Gallagher. *Rydberg Atoms*. Cambridge University Press, 1994.

[4] R. F. Stebbings and F. B. Dunning. *Rydberg States of Atoms and Molecules*. Cambridge University Press, 1983.

[5] Harold J. Metcalf and Peter van der Straten. *Laser Cooling and Trapping*. Springer, 1999.

[6] W. R. Anderson, J. R. Veale, and T. F. Gallagher. Resonant dipole-dipole energy transfer in a nearly frozen Rydberg gas. *Phys. Rev. Lett.*, 80(2):249, January 1998.

[7] I. Mourachko, D. Comparat, F. de Tomasi, A. Fioretti, P. Nosbaum, V. M. Akulin, and P. Pillet. Many-body effects in a frozen Rydberg gas. *Phys. Rev. Lett.*, 80(2):253, January 1998.

[8] J. S. Frasier, V. Celli, and T. Blum. Resonant processes in a frozen gas. *Phys. Rev. A*, 59(6): 4358, June 1999.

[9] W. R. Anderson, M. P. Robinson, J. D. D. Martin, and T. F. Gallagher. Dephasing of resonant energy transfer in a cold Rydberg gas. *Phys. Rev. A*, 65(6):063404, June 2002.

[10] Thomas J. Carroll, Katharine Claringbould, Anne Goodsell, M. J. Lim, and Michael W. Noel. Angular dependence of the dipole-dipole interaction in a nearly one-dimensional sample of Rydberg atoms. *Phys. Rev. Lett.*, 93(15):153001, October 2004.

[11] T. Cubel Liebisch, A. Reinhard, P. R. Berman, and G. Raithel. Atom counting statistics in ensembles of interacting Rydberg atoms. *Phys. Rev. Lett.*, 95(25):253002, December 2005.

[12] Neil W. Ashcroft and N. David Mermin. *Solid State Physics*. Saunders College Publishing, 1976.

[13] Marcel Mudrich, Nassim Zahzam, Thibault Vogt, Daniel Comparat, and Pierre Pillet. Back and forth transfer and coherent coupling in a cold Rydberg dipolegas. *Phys. Rev. Lett.*, 95 (23):233002, November 2005.

[14] J. Kasprzak, M. Richard, S. Kundermann, A. Baas, P. Jeambrun, J. M. J. Keeling, F. M. Marchetti, M. H. Szymańska, R. Andr, J. L. Staehli, V. Savona, P. B. Littlewood, B. Deveaud, and Le Si Dang. Bose-Einstein condensation of exciton polaritons. *Nature*, 443(7110):409, September 2006.

[15] K. Afrousheh, P. Bohlouli-Zanjani, D. Vagale, A. Mugford, M. Fedorov, and J. D. D. Martin. Spectroscopic observation of resonant electric dipole-dipole interactions between cold Rydberg atoms. *Phys. Rev. Lett.*, 93(23):233001, November 2004.

[16] I. Mourachko, Wenhui Li, and T. F. Gallagher. Controlled many-body interactions in a frozen Rydberg gas. *Phys. Rev. A*, 70(3):031401, September 2004.

[17] Thomas J. Carroll, Shubha Sunder, and Michael W. Noel. Many-body interactions in a sample of ultracold Rydberg atoms with varying dimensions and densities. *Phys. Rev. A*, 73(3):032725, March 2006.

[18] Paul J. Tanner, Jianing Han, E. S. Shuman, and T. F. Gallagher. Many-body ionization in a frozen Rydberg gas. *Phys. Rev. Lett.*, 100(4):043002, January 2008.

[19] S. M. Farooqi, D. Tong, S. Krishnan, J. Stanojevic, Y. P. Zhang, J. R. Ensher, A. S. Estrin, C. Boisseau, R. Côté, E. E. Eyler, and P. L. Gould. Long-range molecular resonances in a cold Rydberg gas. *Phys. Rev. Lett.*, 91(18):183002, October 2003.

[20] D. Jaksch, J. I. Cirac, P. Zoller, S. L. Rolston, R. Côté, and M. D. Lukin. Fast quantum gates for neutral atoms. *Phys. Rev. Lett.*, 85(10):2208, September 2000.

[21] M. Saffman and T. G. Walker. Creating single-atom and single-photon sources from entangled atomic ensembles. *Phys. Rev. A*, 66(6):065403, December 2002.

[22] Isabelle Bouchoule and Klaus Mølmer. Spin squeezing of atoms by the dipole interaction in virtually excited Rydberg states. *Phys. Rev. A*, 65(4):041803, April 2002.

[23] D. Tong, S. M. Farooqi, J. Stanojevic, S. Krishnan, Y. P. Zhang, R. Côté, E. E. Eyler, and P. L. Gould. Local blockade of Rydberg excitation in an ultracold gas. *Phys. Rev. Lett.*, 93 (6):063001, August 2004.

[24] Thibault Vogt, Matthieu Viteau, Jianming Zhao, Amodsen Chotia, Daniel Comparat, and Pierre Pillet. Dipole blockade at Förster resonances in high resolution laser excitation of Rydberg states of cesium atoms. *Phys. Rev. Lett.*, 97(8):083003, August 2006.

[25] Thibault Vogt, Matthieu Viteau, Amodsen Chotia, Jianming Zhao, Daniel Comparat, and Pierre Pillet. Electric-field induced dipole blockade with Rydberg atoms. *Phys. Rev. Lett.*, 99 (7):073002, August 2007.

[26] Rolf Heidemann, Ulrich Raitzsch, Vera Bendkowsky, Björn Butscher, Robert Löw, Luis Santos, and Tilman Pfau. Evidence for coherent collective Rydberg excitation in the strong blockade regime. *Phys. Rev. Lett.*, 99(16):163601, October 2007.

[27] Rolf Heidemann, Ulrich Raitzsch, Vera Bendkowsky, Björn Butscher, Robert Löw, and Tilman Pfau. Rydberg excitation of Bose-Einstein condensates. *Phys. Rev. Lett.*, 100(3):033601, January 2008.

[28] F. Robicheaux and J. V. Hernández. Many-body wave function in a dipole blockade configuration. *Phys. Rev. A*, 72(6):063403, December 2005.

[29] C. Ates, T. Pohl, T. Pattard, and J. M. Rost. Strong interaction effects on the atom counting statistics of ultracold Rydberg gases. *J. Phys. B*, 39(11):L233, May 2006.

[30] C. Ates, T. Pohl, T. Pattard, and J. M. Rost. Many-body theory of excitation dynamics in an ultracold Rydberg gas. *Phys. Rev. A*, 76(1):013413, July 2007.

[31] C. Ates, T. Pohl, T. Pattard, and J. M. Rost. Antiblockade in Rydberg excitation of an ultracold lattice gas. *Phys. Rev. Lett.*, 98(2):023002, January 2007.

[32] J. V. Hernández and F. Robicheaux. Simulation of a strong van der Waals blockade in a dense ultracold gas. *J. Phys. B*, 41(4):045301, February 2008.

[33] E. Solano, M. França Santos, and P. Milman. Quantum phase gate with a selective interaction. *Phys. Rev. A*, 64(2):024304, July 2001.

[34] Michael A. Nielsen and Isaac L. Chuang. *Quantum Information*. Cambridge University Press, 2000.

[35] I. E. Protsenko, G. Reymond, N. Schlosser, and P. Grangier. Operation of a quantum phase gate using neutral atoms in microscopic dipole traps. *Phys. Rev. A*, 65(5):052301, April 2002.

[36] M. Saffman and T. G. Walker. Analysis of a quantum logic device based on dipole-dipole interactions of optically trapped Rydberg atoms. *Phys. Rev. A*, 72(2):022347, August 2005.

[37] E. Brion, A. S. Mouritzen, and K. Mølmer. Conditional dynamics induced by new configurations for Rydberg dipole-dipole interactions. *Phys. Rev. A*, 76(2):022334, August 2007.

[38] E. Brion, K. Mølmer, and M. Saffman. Quantum computing with collective ensembles of multilevel systems. *Phys. Rev. Lett.*, 99(26):260501, December 2007.

[39] E. Brion and L. H. Pedersen K. Mølmer. Implementing a neutral atom Rydberg gate without populating the Rydberg state. *J. Phys. B*, 40(9):S159, April 2007.

[40] T. A. Johnson, E. Urban, T. Henage, L. Isenhower, D. D. Yavuz, T. G. Walker, and M. Saffman. Rabi oscillations between ground and Rydberg states with dipole-dipole atomic interactions. *Phys. Rev. Lett.*, 100(11):113003, March 2008.

[41] T. Cubel, B. K. Teo, V. S. Malinovsky, J. R. Guest, A. Reinhard, B. Knuffman, P. R. Berman, and G. Raithel. Coherent population transfer of ground-state atoms into Rydberg states. *Phys. Rev. A*, 72(2):023405, August 2005.

[42] J. Sebby-Strabley, R. T. R. Newell, J. O. Day, E. Brekke, and T. G. Walker. High-density mesoscopic atom clouds in a holographic atom trap. *Phys. Rev. A*, 71(2):021401, February 2005.

[43] J. Sebby-Strabley, R. T. R. Newell, J. O. Day, E. Brekke, and T. G. Walker. Dense atom clouds in a holographic atom trap. *Opt. Lett.*, 28(14):12266, July 2003.

[44] S. Bergamini, B. Darqui, M. Jones, L. Jacubowiez, A. Browaeys, , and P. Grangier. Holographic generation of microtrap arrays for single atoms by use of a programmable phase modulator. *J. Opt. Soc. Am. B*, 21(11):1889, November 2004.

[45] Karl D. Nelson, Xiao Li, and David S. Weiss. Imaging single atoms in a three-dimensional array. *Nature Physics*, 3(8):556, August 2007.

[46] T. C. Killian, S. Kulin, S. D. Bergeson, L. A. Orozco, C. Orzel, and S. L. Rolston. Creation of an ultracold neutral plasma. *Phys. Rev. Lett.*, 83(23):4776, December 1999.

[47] M. P. Robinson, B. Laburthe Tolra, Michael W. Noel, T. F. Gallagher, and P. Pillet. Spontaneous evolution of Rydberg atoms into an ultracold plasma. *Phys. Rev. Lett.*, 85(21):4466, November 2000.

[48] Wenhui Li, Michael W. Noel, Michael P. Robinson, Paul J. Tanner, Thomas F. Gallagher, Daniel Comparat, Bruno Laburthe Tolra, Nicolas Vanhaecke, Thibault Vogt, Nassim Zahzam, Pierre Pillet, and Duncan A. Tate. Evolution dynamics of a dense frozen Rydberg gas to plasma. *Phys. Rev. A*, 70(4):042713, October 2004.

[49] A. Walz-Flannigan, J. R. Guest, J.-H. Choi, and G. Raithel. Cold-Rydberg-gas dynamics. *Phys. Rev. A*, 69(6):063405, June 2004.

[50] T. C. Killian, M. J. Lim, S. Kulin, R. Dumke, S. D. Bergeson, and S. L. Rolston. Formation of Rydberg atoms in an expanding ultracold neutral plasma. *Phys. Rev. Lett.*, 86(17):3759, April 2001.

[51] Wenhui Li, Paul J. Tanner, and T. F. Gallagher. Dipole-dipole excitation and ionization in an ultracold gas of Rydberg atoms. *Phys. Rev. Lett.*, 94(17):173001, May 2005.

[52] Christophe Boisseau, Ionel Simbotin, and Robin Côté. Macrodimers: Ultralong range Rydberg molecules. *Phys. Rev. Lett.*, 88(13):133004, March 2002.

[53] Arne Schwettmann, Jeff Crawford, K. Richard Overstreet, and James P. Shaffer. Cold Cs Rydberg-gas interactions. *Phys. Rev. A*, 74(2):020701, August 2006.

[54] F. Robicheaux. Ionization due to the interaction between two Rydberg atoms. *J. Phys. B*, 38 (2):S333, January 2005.

[55] B. Knuffman and G. Raithel. Emission of fast atoms from a cold Rydberg gas. *Phys. Rev. A*, 73(2):020704, February 2006.

[56] T. Amthor, M. Reetz-Lamour, S. Westermann, J. Denskat, and M. Weidemüller. Mechanical effect of van der Waals interactions observed in real time in an ultracold Rydberg gas. *Phys. Rev. Lett.*, 98(2):023004, January 2007.

[57] Thomas Amthor, Markus Reetz-Lamour, Christian Giese, and Matthias Weidemüller. Modeling many-particle mechanical effects of an interacting Rydberg gas. *Phys. Rev. A*, 76(5): 054702, November 2007.

[58] A. L. de Oliveira, M. W. Mancini, V. S. Bagnato, and L. G. Marcassa. Rydberg cold collisions dominated by ultralong range potential. *Phys. Rev. Lett.*, 90(14):143002, April 2003.

[59] John David Jackson. *Classical Electrodynamics*. Wiley, 1999.

[60] David J. Griffiths. *Introduction to Electrodynamics*. Prentice Hall, 1999.

[61] Kilian Singer, Jovica Stanojevic, Matthias Weidemüller, and Robin Côté. Long-range interactions between alkali Rydberg atom pairs correlated to the *nsns*, *npnp* and *ndnd* asymptotes. *Journal of Physics B*, 38(2):S295, January 2005.

[62] A. Dalgarno and W. D. Davidson. The calculation of van der Waals interactions. *Adv. At. Mol. Phys.*, 2:1, 1966.

[63] M. Marinescu and A. Dalgarno. Dispersion forces and long-range electronic transition dipole moments of alkali-metal dimer excited states. *Phys. Rev. A*, 52(1):311, July 1995.

[64] M. Marinescu. Dispersion coefficients for the *np-np* asymptote of homonuclear alkali-metal dimers. *Phys. Rev. A*, 56(6):4764, December 1997.

[65] Leonard Schiff. *Quantum Mechanics*. McGraw-Hill, 1968.

[66] A. Reinhard, T. Cubel Liebisch, B. Knuffman, and G. Raithel. Level shifts of rubidium Rydberg states due to binary interactions. *Phys. Rev. A*, 75(3):032712, March 2007.

[67] Wenhui Li, I. Mourachko, M. W. Noel, and T. F. Gallagher. Millimeter-wave spectroscopy of cold Rb Rydberg atoms in a magneto-optical trap: Quantum defects of the *ns*, *np*, and *nd* series. *Phys. Rev. A*, 67(5):052502, May 2003.

[68] Jianing Han, Yasir Jamil, D. V. L. Norum, Paul J. Tanner, and T. F. Gallagher. Rb nf quantum defects from millimeter-wave spectroscopy of cold ^{85}Rb Rydberg atoms. *Phys. Rev. A*, 74(5):054502, November 2006.

[69] C. E. Moore. *Atomic Energy Levels NSRDS-NBS*, 35, 1971.

[70] A. Reinhard, T. Cubel Liebisch, K. C. Younge, P. R. Berman, and G. Raithel. Rydberg-Rydberg collisions: resonant enhancement of state-mixing and Penning ionization. *Phys. Rev. Lett.*, 100(12):123007, March 2008.

[71] A. Reinhard, K. C. Younge, and G. Raithel. In preparation.

[72] P. Bohlouli-Zanjani, J. A. Petrus, and J. D. D. Martin. Enhancement of Rydberg atom interactions using ac Stark shifts. *Physical Review Letters*, 98(20):203005, May 2007.

[73] E. L. Raab, M. Prentiss, Alex Cable, Steven Chu, and D. E. Pritchard. Trapping of neutral sodium atoms with radiation pressure. *Phys. Rev. Lett.*, 59(23):2631, Dec 1987.

[74] Z. T. Lu, K. L. Corwin, M. J. Renn, M. H. Anderson, E. A. Cornell, and C. E. Wieman. Low-velocity intense source of atoms from a magneto-optical trap. *Phys. Rev. Lett.*, 77(16): 3331–3334, Oct 1996.

[75] T. B. Swanson, D. Asgeirsson, J. A. Behr, A. Gorelov, and D. Melconian. Efficient transfer in a double magneto-optical trap system. *J. Opt. Soc. Amer. B*, (11):2641, November 1998.

[76] C. J. Myatt, N. R. Newbury, R. W. Ghrist, S. Loutzenhiser, and C. E. Wieman. Multiply loaded magneto-optical trap. *Opt. Lett.*, (4), 1996.

[77] K. I. Lee, J. A. Kim, H. R. Noh, and W. Jhe. Single-beam atom trap in a pyramidal and conical hollow mirror. *Opt. Lett.*, 21(15):1177, August 1996.

[78] R. S. Williamson III, P. A. Voytas, R. T. Newell, and T. Walker. A magneto-optical trap loaded from a pyramidal funnel. *Opt. Exp.*, 3(3):111, August 1998.

[79] Jason Remington Ensher. *The first experiments with Bose-Einstein condensation of* ^{87}Rb. PhD thesis, The University of Colorado at Boulder, 1996.

[80] Natalya Morrrow. *Atomic Motion in an Optical Lattice*. PhD thesis, The University of Michigan, 2006.

[81] A. Ashkin. Acceleration and trapping of particles by radiation pressure. *Phys. Rev. Lett.*, 24 (4):156, Jan 1970.

[82] Steven Chu, J. E. Bjorkholm, A. Ashkin, and A. Cable. Experimental observation of optically trapped atoms. *Phys. Rev. Lett.*, 57(3):314, Jul 1986.

[83] J. D. Miller, R. A. Cline, and D. J. Heinzen. Far-off-resonance optical trapping of atoms. *Phys. Rev. A*, 47(6):R4567, Jun 1993.

[84] Paul R. Berman and Vladimir Malinovsky. *Quantum Optics*. Unpublished, 2008.

[85] J. R. Lowell, T. Northup, B. M. Patterson, T. Takekoshi, and R. J. Knize. Measurement of the photoionization cross section of the $5s_{1/2}$ state of rubidium. *Phys. Rev. A*, 66(6):062704, Dec 2002.

[86] C. Gabbanini, F. Ceccherini, S. Gozzini, and A. Lucchesini. Partial photoionization cross section measurement in a Rb magneto-optical trap. *J. Phys. B*, 31(18):4143, September 1998.

[87] B. K. Teo, D. Feldbaum, T. Cubel, J. R. Guest, P. R. Berman, and G. Raithel. Autler-Townes spectroscopy of the $5s_{1/2} - 5p_{3/2} - 44d$ cascade of cold ^{85}Rb atoms. *Phys. Rev. A*, 68(5):053407, November 2003.

[88] T. W. Hänsch, I. S. Shahin, and A. L. Schawlow. High-resolution saturation spectroscopy of the sodium D lines with a pulsed tunable dye laser. *Phys. Rev. Lett.*, 27(11):707, Sep 1971.

[89] W. Demtröder. *Laser Spectroscopy*. Springer-Verlag, 1982.

[90] E. Hansis, T. Cubel, J.-H. Choi, J. R. Guest, and G. Raithel. A simple pressure-tuned Fabry-Perot interferometer. *Rev. of Sci. Inst.*, 76(3):033105, March 2005.

[91] Joseph Ladislas Wiza. Microchannel plate detectors. *Nuclear Instruments and Methods*, 162 (1):587, June 1979.

[92] L. Mandel. Sub-Poissonian photon statistics in resonance fluorescence. *Optics Letters*, 4(7): 205, July 1979.

[93] J.-H. Choi, B. Knuffman, T. Cubel Liebisch, A. Reinhard, and G. Raithel. Cold Rydberg atoms. *Adv. in At. Mol. and Opt. Physics*, 54:131, 2007.

[94] A. Reinhard K. C. Younge, T. Cubel Liebisch, B. Knuffman, P. R. Berman, and G. Raithel. Double-resonance spectroscopy of interacting Rydberg-atom systems. *Submitted to Phys. Rev. Lett.*, 2008.

[95] K. C. Younge, A. Reinhard, T. Pohl, P. R. Berman, and G. Raithel. Exploring collective phenomena in cold Rydberg gas interactions. *Submitted to Nature Physics*, 2008.

[96] Jianing Han and T. F. Gallagher. Field ionization of the frozen Rydberg gas. *Phys. Rev. A*, 77(1):015404, 2008.